

1D-to-3D Transition of Phonon Heat Conduction in Polyethylene Using Molecular Dynamics Simulations

by,
Asegun Sekou Famake Henry

B.S., Mechanical Engineering (2004)
Florida A & M University

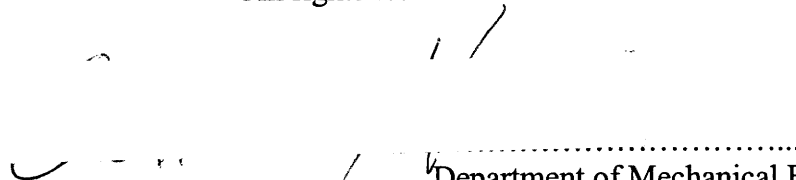
M.S., Mechanical Engineering (2006)
Massachusetts Institute of Technology

Submitted to the Department of Mechanical Engineering
in Partial Fulfillment of the Requirements for the Degree of
Doctor of Philosophy in Mechanical Engineering

at the
Massachusetts Institute of Technology
May 2009

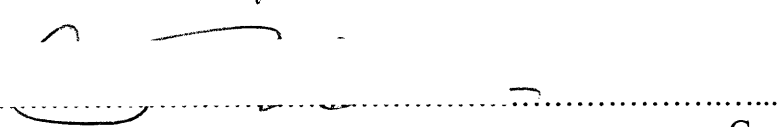
© 2009 Massachusetts Institute of Technology
All rights reserved

Signature of
Author.....



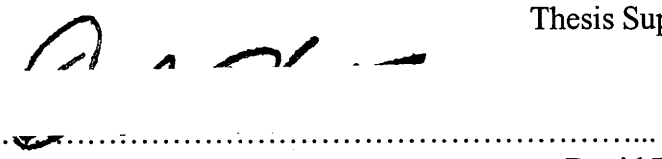
Department of Mechanical Engineering
May 9, 2009

Certified
by.....

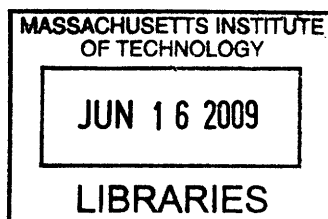


Gang Chen
Professor of Mechanical Engineering
Thesis Supervisor

Accepted
by.....



David E. Hardt
Chairman, Department Committee on Graduate Students



ARCHIVES

1D-to-3D Transition of Phonon Heat Conduction in Polyethylene Using Molecular Dynamics Simulations

by,

Asegun Sekou Famake Henry

Submitted to the Department of Mechanical Engineering
in Partial Fulfillment of the Requirements for the Degree of
Doctor of Philosophy in Mechanical Engineering

Abstract

Experiments have demonstrated that the mechanical stretching of bulk polyethylene can increase its thermal conductivity by more than two orders of magnitude, from 0.35 W/mK to over 40W/mK, which is comparable to steel. This strong effect is believed to arise from the increased alignment of the constituent polymer chains, which are thought to have very high thermal conductivity. Although it is well established that bulk polymers have low thermal conductivity, these experiments suggest that cheap, high thermal conductivity polymer materials can be engineered. This type of advancement may provide a much cheaper alternative to the conventional metal-based heat transfer materials that are used today.

In order to quantify upper limits on the thermal conductivity of polyethylene, we examine the underlying phonon (lattice wave) transport using molecular dynamics simulations. We first show that the thermal conductivity of individual polyethylene chains is high, and can actually diverge (approach infinity) in some cases. We then discuss how the high thermal conductivity of individual chains is reduced by the presence of additional chains, through van der Waals chain-chain interactions. These intermolecular interactions give rise to both a 2D planar lattice structure and a 3D bulk lattice structure, which allows for the observation of an interesting 1D-to-3D transition in phonon transport. For most crystalline nanostructures, the thermal conductivity decreases with decreasing crystal size from an enhanced boundary scattering of phonons. In the case of polyethylene, however, the intermolecular chain-chain interactions increase phonon-phonon scattering along each chain and actually result in the opposite trend, where the thermal conductivity increases with decreasing crystal size. The results provide important fundamental insight into phonon-phonon interactions and will also aid in the design and structural optimization of high thermal conductivity polymers.

Thesis Supervisor: Gang Chen

Title: Warren and Towneley Rohsenow Professor of Mechanical Engineering

Acknowledgements

I must first and foremost thank my advisor and mentor, Prof. Gang Chen. His knowledge, drive, dedication to student development, guidance, and commitment to excellence is both inspiring and remarkable. I must particularly thank Prof. Chen for giving me the freedom early on in my matriculation to learn about molecular dynamics simulations and follow my passion. Most students arrive at MIT, search for an advisor and end up assigned to a specific project they are expected to contribute to. Prof. Chen's decision to let me explore my interests in atomic vibration was the key to all my subsequent successes and development. I also thank Prof. Chen for investing time and energy into my academic and career development, by inviting me to attend the US Japan seminar on nanoscale transport phenomena after only one year of research experience. These early opportunities to gain the experience I desired were invaluable. Throughout my time at MIT, Prof. Chen has consistently shown faith and confidence in my abilities, for which I am eternally grateful.

I am also grateful to the other members of my thesis committee, Prof. John H. Lienhard V and Prof. Mildred Dresselhaus, for their encouragement, guidance and insightful commentary on my work. I must particularly thank Prof. Lienhard for his insight into the divergent phenomena, recognizing its possible connection to the Hurst phenomena in turbulence. His insight and perspective was extremely helpful and aided me in recognizing the larger implications of my work. I must also thank Prof. Dresselhaus for her scientific insight, nurturing and guidance as well. Prof. Dresselhaus was instrumental to my career success and I am forever indebted to her for her recommendations for faculty positions, assistance in finding a postdoc and her encouraging words of wisdom. She has played a crucial role in my maturation and development and she has been a blessing to my experience at MIT. I am deeply grateful and appreciative of the time, energy and aid she has provided during my matriculation.

It is important to also state that it has been a privilege to work with everyone in the Nanoengineering Group, whose members past and present have been a source of lasting friendships and scientific inspiration. I am especially thankful to Prof. Ronggui

Yang and Dr. Lu Hu for mentoring me as a new graduate student. Dr. Hu in particular was instrumental in my learning about high performance computing and the development of my coding abilities. I also thank my friend and colleague, Michael Ghebrebrhan, who was instrumental in helping me to learn quantum and statistical mechanics. I am also grateful to the Department of Energy for their generous financial support via the computational science graduate fellowship program. Their financial support gave me the freedom to pursue my own ideas, and the program played a key role in my pursuit of a broader knowledge base that centers on high performance computing. I also wish to especially thank my parents, sister, extended family and community for their encouragement and support throughout the MIT experience. Without them I would have no foundation. I also wish to thank Azizi Carle for her friendship, understanding, love and support throughout my Ph.D. experience.

Table of Contents

Chapter 1: Introduction	11
1.1 Introduction to Phonon Transport and the Thermal Conductivity of Crystalline Solids	13
1.2 Anomalous Heat Conduction in 1D Lattices	23
1.3 Polymer Chain Modeling.....	26
1.4 Objectives	31
Chapter 2: Molecular Dynamics Simulations.....	34
2.1 The Theory of Molecular Dynamics Simulations.....	34
2.2 Interatomic Potentials	38
2.3 The Adaptive Intermolecular Reactive Empirical Bond Order Potential (AIREBO)	42
Chapter 3: Analysis of MD Simulation Results.....	48
3.1 Energy and Temperature	48
3.2 Green-Kubo Formula for the Thermal Conductivity	54
3.3 The Boltzmann Equation for Phonon Transport	61
3.4 Lattice Dynamics.....	66
3.5 Normal Mode Analysis	71
3.6 Simulation Procedures	74
Chapter 4: Single Chain Results	77
4.1 Divergent Thermal Conductivity.....	77
4.2 Normal Mode Analysis	81
4.3 Divergent Behavior Interpretation	91
4.4 Finite Length Chains	94
Chapter 5: PE Lattice Thermal Conductivity.....	98
5.1 1D-to-3D Transition.....	98
5.2 1D-to-2D: Anharmonicity vs. Conductance.....	103
Chapter 6: Conclusions and Future Directions	110
6.1 Conclusions.....	110
6.2 Future Directions.....	112
References	115

List of Figures

Figure 1.1.1 HRTEM image of Nb ₂ O ₅ nanoparticles.....	14
Figure 1.1.2 Classical and quantum harmonic oscillators.....	16
Figure 1.1.3 Thermal conductivity of silicon.....	19
Figure 1.1.4 Dimensional dependence of classical size effects.....	20
Figure 1.1.5 Thermal conductivity vs. diameter.....	21
Figure 1.2.1 FPU recurrence phenomenon.....	25
Figure 1.3.1 Two neighboring polyethylene chains.....	28
Figure 1.3.2 Polyethylene bulk lattice structure.....	30
Figure 1.4.1 Thermal conductivity of mechanically stretched bulk polyethylene.....	32
Figure 2.1.1 Two-dimensional illustration of periodic boundary conditions.....	36
Figure 2.2.1 Lennard-Jones potential and force.....	41
Figure 3.4.1 One-dimensional chain of atoms connected by springs.....	66
Figure 3.4.2 Phonon dispersion curves for polyethylene.....	69
Figure 3.4.3 Atomic displacements for the 4 acoustic polarizations in a polyethylene chain.....	70
Figure 4.1.1 The heat flux autocorrelation function for a 40 unit cell long chain.....	78
Figure 4.1.2 Average Green-Kubo thermal conductivity integral.....	79
Figure 4.1.3 Green-Kubo thermal conductivity integral.....	79
Figure 4.1.4 Green-Kubo thermal conductivity integrals for 5 independent simulations.....	81
Figure 4.2.1 Normal mode correlation functions.....	84
Figure 4.2.2 Normal mode cross-correlation functions.....	85
Figure 4.2.3 Normal mode correlation functions.....	87
Figure 4.2.4 Normal mode correlation functions.....	89
Figure 4.2.5 Normal mode correlation functions.....	90
Figure 4.3.1 Diagram of scattering and correlation based paradigms.....	92
Figure 4.4.1 The predicted thermal conductivity for individual polyethylene chains.....	96
Figure 4.4.2 The predicted thermal conductance for individual polyethylene chains.....	97
Figure 5.1.1 Conceptual illustration of the 1D-to-3D transition.....	99
Figure 5.1.2 Normalized heat flux autocorrelation.....	100
Figure 5.1.3 1D-to-3D thermal conductivity results.....	102
Figure 5.2.1 Thermal conductivity of chain 1 in the presence of chain 2.....	105
Figure 5.2.2 Normalized heat flux autocorrelation functions for chain 1.....	106
Figure 5.2.3 Chain-chain conductance between chain 1 and chain 2.....	107
Figure 5.2.4 Normalized energy exchange autocorrelation.....	108

Chapter 1: Introduction

High thermal conductivity materials play an important role in a wide range of heat transfer-related applications throughout a variety of industries. For example, high thermal conductivity materials are needed for efficient heat exchangers, which are employed in applications such as space heating, refrigeration, air conditioning, power plants, chemical plants, petroleum refineries and natural gas processing plants. High thermal conductivity materials are also needed to make heat sinks, which are used in heat engines, cooling electronic devices, lasers etc. These materials are usually based on metals, where conduction electrons are responsible for a significant portion of the thermal transport. Bulk polymers, on the other hand, are thermal insulators, but have the advantage of low manufacturing costs [1]. One approach to making higher thermal conductivity materials based on polymers has involved incorporation of additives [2-6], such as carbon nanotubes (CNTs) which have very high thermal conductivity [7-17]. This approach, however, has only resulted in marginal overall improvement [2-6]. An alternative approach involves restructuring the polymer itself, where several experiments have demonstrated that the thermal conductivity of polymer chain based materials can increase dramatically from improved chain alignment, achieved through mechanical stretching [18, 19]. Depending upon the extent to which bulk polymer's thermal conductivity can be enhanced, these materials may be able to serve as cheap, lightweight thermal conductors that may be able to replace metals in many of the fore mentioned applications. The electrically insulating nature of polymers could also allow high thermal conductivity polymers to open up an array of new applications, where metals cannot be used.

One such potential application where high thermal conductivity polymers could be useful is in superconductor sheathing. Here the high thermal conductivity could enable better heat removal from the cryogenic current carrying wires, while simultaneously acting as an electrical insulation barrier. If the thermal conductivity can be raised high enough, polymer chain-based materials may even be able to compete with conventional heat transfer materials, which are used in a variety of heat transfer components such as

heat exchangers and heat sinks. If cheap manufacturing techniques can be developed, these structurally engineered polymers could also serve as more efficient heat spreaders in personal electronics applications, such as cell phone and laptop casings, where bulk polymers are typically used. Increasing the thermal conductivity of polymers extends their range of applicability. The first step towards stimulating more research into the development of high thermal conductivity polymers lies in quantifying the maximum thermal conductivity that can be achieved. Understanding the fundamental limitations on heat conduction in polymer materials can motivate further research into experimental characterization, structural optimization and large-scale manufacturing processes.

To address the fundamental limits on the thermal conductivity of polymers we used molecular dynamics (MD) simulations to investigate the details of phonon transport in polyethylene (PE), the simplest and most widely used polymer. Intuitively we know that the highest possible thermal conductivity that can be obtained for any PE based nano or macrostructure is bounded by the upper limit for a single molecular chain. We also know that any macroscopic polymer material will consist of many interacting chains, which will illicit different heat conduction behavior. In this introductory chapter we first provide an overview of phonon heat conduction and discuss the behavior of thermal conductivity in bulk solids. We proceed to a discussion of classical size effects on the thermal conductivity and explain its connection to 3D, 2D and 1D phonon transport. We then focus on 1D phonon transport by introducing the theoretical background associated with anomalous heat conduction in 1D lattices and we consider how it relates to phonon transport in single polymer chains. Then we provide an overview of polymer chain modeling and the effects of chain-chain interactions with neighboring molecules to lay the foundation for the modeling procedure used in this work. We then proceed to a discussion of the PE lattice structure and introduce the concept of a 1D-to-3D transition in phonon transport, which is one of the primary phenomena we seek to highlight in this thesis.

In chapter 2 we discuss the theory of MD simulations and we present the model used in our investigation of polyethylene. In chapter 3 we derive the equations used to analyze the simulation results, which allows us to calculate thermal conductivity and analyze the detailed phonon transport mechanisms. Chapter 3 also includes a brief

discussion of the model implementation and the specific parameters that were used to conduct the simulations. In chapter 4 we present the results of single chain simulations and provide a detailed discussion on the anomalous transport phenomenon that was observed. Here, we provide an explanation for the phenomenon based on theoretical developments presented in chapter 3. Chapter 5 presents results from PE chain lattice simulations and focuses on the effects of chain-chain interactions with an emphasis on the 1D-to-3D transition effect. Chapter 5 also presents results for the chain-chain conductance and discusses the interplay between anharmonicity and conductance as it relates to the thermal conductivity. In chapter 6 we provide a summary of the findings and discuss possible directions for future work.

1.1 Introduction to Phonon Transport and the Thermal Conductivity of Crystalline Solids

All terrestrial materials are composed of atoms. Within every material, Coulombic interactions between neighboring atoms give rise to specific bonding characteristics, which lead to different classifications of materials, such as noble gases, metals, non-metals, halogens, semiconductors, semi-metals etc [20, 21]. The atoms in crystalline solids form a periodic arrangement with long range order as shown in Fig. 1.1.1, which shows a high resolution tunneling electron microscope image of a Nb_2O_5 nanoparticle [22]. The position of each atom in a crystalline solid is localized to its lattice site as a result of the potential well created by the Coulombic interactions with the neighboring atoms [20, 23]. Since each atom is surrounded by other atoms, it experiences a restoring force whenever it is perturbed away from its equilibrium lattice site [20, 23]. If we think classically and imagine starting with all atoms at rest, we can perturb the position of one atom and eventually all other atoms will begin to move, because the atoms are coupled together. From this classical picture it becomes evident that at finite temperature all atoms are constantly in motion and vibrate about their respective lattice sites [23].

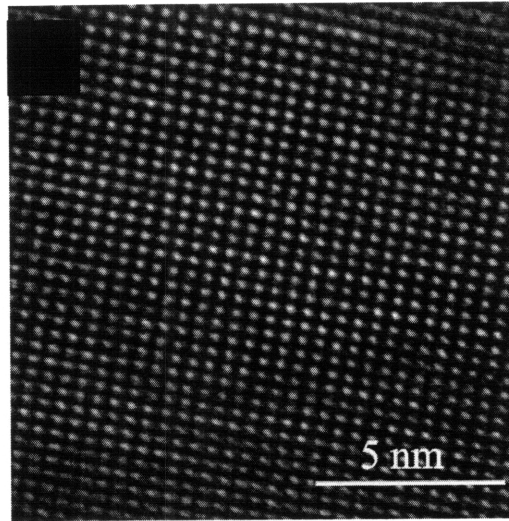


Figure 1.1.1 HRTEM image of Nb₂O₅ nanoparticles [22]

For a large bulk crystal, which contains long range order, the atomic vibrations can be approximately decomposed into periodic wave solutions. These vibrations usually comprise the most significant portion of the crystal's thermal energy (thermodynamic internal energy) and the lattice vibrational waves can carry energy over large distances. The transportation of this vibrational energy throughout the crystal, from one region of the material where the atoms have higher average kinetic energy, to another region of the crystal, where the atoms have lower average kinetic energy, is the fundamental physics that underlies the science of heat conduction [20, 24, 25]. Regions where the average kinetic energy is higher correspond to higher temperature while regions where the average kinetic energy is lower correspond to lower temperature. It is the coupling between neighboring atom vibrations, via the interatomic forces (potential energy), that allows the energy to conduct from high to low temperature. The key property most often used to describe how efficiently a material can conduct heat is the thermal conductivity. Thermal conductivity was first defined in reference to Fourier's law for heat conduction, where the thermal conductivity κ is the ratio of the heat flux to the temperature gradient $\kappa = -\mathbf{Q}/\nabla T$.

If we approximately model the atomic interactions in a crystalline solid with linear springs satisfying Hooke's law $F = -K \cdot x$, we could solve for the atomic displacements analytically using a Fourier series to describe the different normal modes

of vibration [23]. In this limiting case, the solutions are orthogonal, such that a single lattice wave is able to carry energy indefinitely. This would cause the thermal conductivity to be infinite, because the system would not be able to support a temperature gradient [26]. In reality, the interactions between atoms are nonlinear and do not obey Hooke's law exactly. It is this deviation from the harmonic limit that actually gives rise to thermal resistance and finite thermal conductivity [25, 27]. One way to understand the effects of nonlinearity would be to consider the system as containing the same normal modes obtained from the harmonic approximation [23]. However since the interactions are nonlinear, the normal mode solutions can interact (scatter) and exchange energy with each other [25]. This effect of nonlinearity is often termed anharmonicity, since it is conceived based on the deviation from the harmonic limit. Studying the effects of mode-mode interactions, which are induced by the anharmonicity in real materials, then becomes challenging, because quantifying nonlinearity in different materials with different bond chemistries can be difficult. Nonetheless, recent advances in numerical techniques such as *ab initio* calculations of 3-phonon scattering rates [28] and normal mode analysis via molecular dynamics simulations [29, 30] have opened up new possibilities for quantitative study of the thermal conductivity at the atomic scale.

Thus far, we have restricted our discussion to the classical picture of atomic vibrations in crystals, while in reality the atomic motion is governed by quantum mechanics. To understand the quantum picture of lattice wave transport in crystals, let us first consider the classical behavior of a linear chain of harmonic oscillators. For a classical chain of oscillators, we can solve for the atomic displacements with a Fourier series, indexed by different wave vectors $k = 2\pi/\lambda$ based on the normal mode wavelength λ [23]. We can then consider the quantum analog of the system by recasting the classical system's energetic description as a quantum mechanical Hamiltonian operator [21],

$$E = \frac{1}{2}m(\omega^2 x^2 + \dot{x}^2) \Rightarrow \mathbf{H} = \frac{\hat{\mathbf{p}}^2}{2m} + \frac{m\omega^2 \hat{\mathbf{x}}^2}{2} \quad (1.1.1)$$

where x and \dot{x} represent the classical particle's displacement and velocity respectively, while $\hat{\mathbf{x}}$ and $\hat{\mathbf{p}}$ represent the quantum displacement and momentum operators respectively,

$$\hat{\mathbf{x}} = x \quad (1.1.2)$$

$$\hat{\mathbf{p}} = i\hbar \frac{d}{dx} \quad (1.1.3)$$

where \hbar is Planck's constant divided by 2π . Each normal mode in the classical system is a solution to the coupled equations of motion. We can find corresponding solutions ϕ_n to the coupled quantum oscillator system based on the Schrödinger equation [21],

$$E\phi_n = \mathbf{H}\phi_n \quad (1.1.4)$$

where E is the mode energy. When solving the system of coupled quantum oscillators we obtain the same wave vectors as the classical system, but the quantum normal mode amplitudes and energy states are quantized as shown in Fig. 1.1.2. As a result, we can draw an analogy between the quantum and classical systems through a quantum quasi-particle description of the normal mode transport in the classical system. In this transformation we define each step (quanta) in energy, n , for the quantum solution as a phonon particle [21, 25].

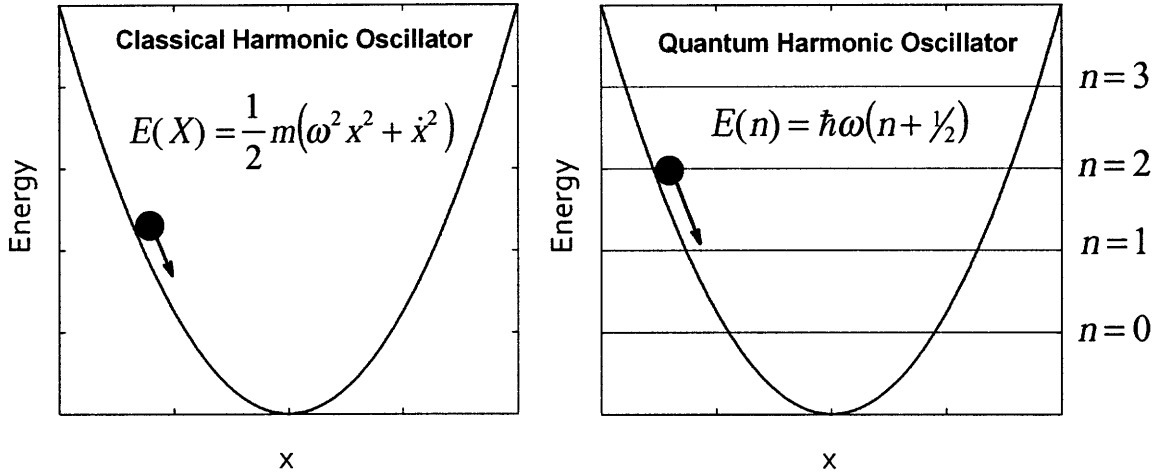


Figure 1.1.2 Classical and quantum harmonic oscillators. In the classical harmonic oscillator problem, the solutions for the atomic displacement consist of sine and cosine functions, which allow the vibrational amplitude x and total energy E to take on any value. The quantum harmonic oscillator solutions are the product of a Gaussian and an n^{th} order Hermite polynomial. Each solution, indexed by the quantum number n corresponds to a particular amplitude and total energy. Each discrete step in n signifies a different solution. The difference in energy between successive solutions is $\hbar\omega$ and each discrete energy quanta $\Delta E = \hbar\omega$ is carried by a phonon quasi-particle.

When a particular normal mode's energy shifts by an amount $\hbar\omega$, it corresponds to the addition of one phonon to the system. Similarly if a particular normal mode's energy is

decreased by an amount $\hbar\omega$, it corresponds to a reduction of one phonon. The entire dynamical exchange of energy between normal modes in a nonlinear classical system therefore corresponds to a series of discrete phonon-phonon scattering events which create and annihilate phonons, subject to the constraints of energy and momentum conservation [25, 27]. For convenience we can write creation $\hat{\mathbf{a}}^\dagger$ and annihilation $\hat{\mathbf{a}}$ operators for each mode, which have the following properties [21],

$$\hat{\mathbf{a}} = \sqrt{\frac{m\omega}{2\hbar}}\hat{\mathbf{x}} + i\sqrt{\frac{1}{2m\hbar\omega}}\hat{\mathbf{p}} \quad (1.1.5)$$

$$\hat{\mathbf{a}}^\dagger = \sqrt{\frac{m\omega}{2\hbar}}\hat{\mathbf{x}} - i\sqrt{\frac{1}{2m\hbar\omega}}\hat{\mathbf{p}} \quad (1.1.6)$$

$$\hat{\mathbf{a}}^\dagger\hat{\mathbf{a}}\phi_n = n\cdot\phi_n \quad (1.1.7)$$

$$\hat{\mathbf{n}} = \hat{\mathbf{a}}^\dagger\hat{\mathbf{a}} \quad (1.1.8)$$

$$\hat{\mathbf{H}} = \hbar\omega(\hat{\mathbf{n}} + \frac{1}{2}) \quad (1.1.9)$$

where n is the quantum number indicating the energy associated with a given solution $E_n = \hbar\omega(n + \frac{1}{2})$. Using this approach we can describe the heat carried by a system of interacting vibrational normal modes as a gas of phonon quasi-particles that are created and annihilated through scattering events (mode-mode interactions). This transformation now allows for a description of thermal transport based on the Boltzmann equation, where the thermal conductivity is proportional to the phonon specific heat, group velocity and average time between collisions [24],

$$\kappa \propto C \cdot v^2 \tau \quad (1.1.10)$$

C and v represent the phonon specific heat and group velocity respectively and can be determined using lattice dynamics methods. The average time between phonon collisions τ , however, is more difficult to determine because it is fundamentally limited by the anharmonicity, which causes phonon-phonon scattering (mode-mode interactions), but can also be affected by other scattering mechanisms such as boundary, impurity, defect, and electron scattering [20, 24, 25].

The effect that different scattering mechanisms have on the thermal conductivity of solids can be seen through the temperature dependence of thermal conductivity for a typical solid such as silicon, which is shown in Fig. 1.1.3. Figure 1.1.3 highlights three

different regimes where the thermal conductivity is limited by different factors. At the lowest cryogenic temperatures, the atomic vibrational amplitudes are low and most modes are likely to be in their ground state. As a result, atoms do not move far from their equilibrium position and their interactions approach the harmonic limit. Therefore, anharmonicity, which is a measure of deviation from the harmonic limit, is minimal at low temperatures, which causes the phonon-phonon scattering rates to approach zero $1/\tau \rightarrow \infty$. The zero scattering rate limit corresponds to the harmonic limit because phonons would not scatter with each other. In a real crystal, however, phonons can still collide with boundaries, interfaces, impurities, crystal imperfections and electrons. In the low temperature regime, phonon impurity and boundary scattering typically become the limiting factors for the average time between collisions and therefore τ is approximately constant. With the time between collisions fixed by the grain size (boundary scattering) and density of impurities, the thermal conductivity then becomes limited by the specific heat, which approaches zero at zero temperature. It is for this reason that the thermal conductivity in Fig. 1.1.3 increases proportional to T^3 [20, 31, 32], in the same manner as the specific heat at low temperatures. Eventually however the thermal conductivity reaches a peak value as phonon-phonon scattering becomes comparable to impurity and boundary scattering effects and τ begins to decrease from its upper limit. Beyond this peak value, thermal conductivity decreases monotonically with increasing temperature. This is because atoms move further away from their lattice sites, which causes anharmonicity to increase and subsequently induces more phonon-phonon scattering, such that it becomes dominant.

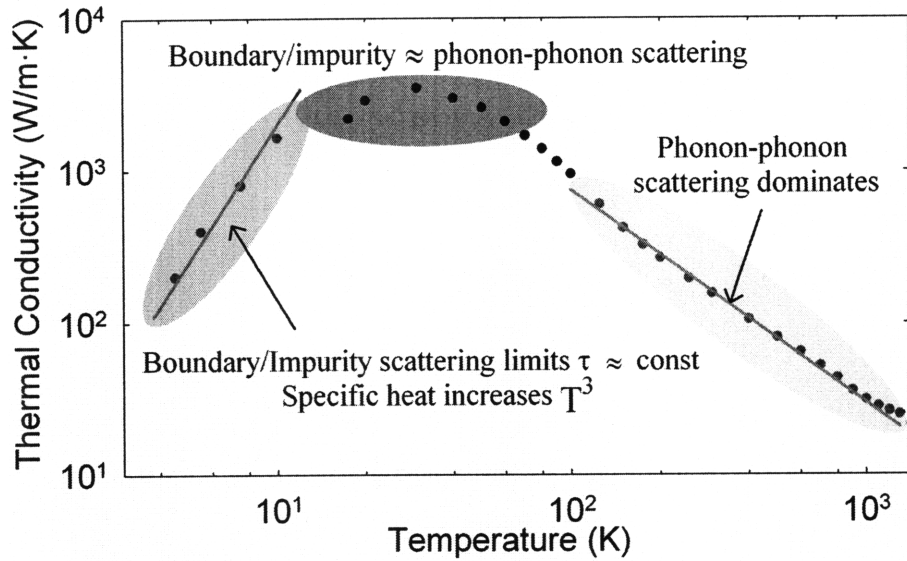


Figure 1.1.3 Thermal conductivity of silicon [32] vs. temperature and governing mechanisms

For most bulk crystalline materials, phonon-phonon scattering is dominant in the higher temperature regime, as indicated in Fig. 1.1.3. In micro and nanostructures, however, phonons can encounter boundaries and interfaces more often than other phonons, which can allow boundary scattering to restrict τ below the upper limit imposed by phonon-phonon scattering. In fact, for some nanostructures, this effect which is commonly referred to as a classical size effect, can result in more than an order of magnitude reduction in thermal conductivity [33, 34]. Through classical size effects it becomes possible to observe stronger reduction in the thermal conductivity as more dimensions of the crystal are constrained by increased boundary/interfacial scattering. Figure 1.1.4 shows experimental results for the thermal conductivity of several different silicon nanostructures. This plot shows that a bulk single crystal which is not constrained to a nanometer length scale in any dimension will have the highest thermal conductivity (3D) [32], while a (2D) thin film which is constrained in one dimension will have lower thermal conductivity [35]. A (1D) nanowire can then have even lower thermal conductivity [34], because it is constrained in two dimensions, and a (0D) quantum dot can exhibit the lowest thermal conductivity since it is constrained in all three dimensions [33]. This classical size effect on thermal conductivity has proven particularly useful for improving thermoelectric material performance, because it allows the thermal

conductivity to be reduced without significant impact on electrical transport. Many studies over the last 20 years have contributed to understanding size effects and the efficiency improvements have been largely due to thermal conductivity reduction [36].

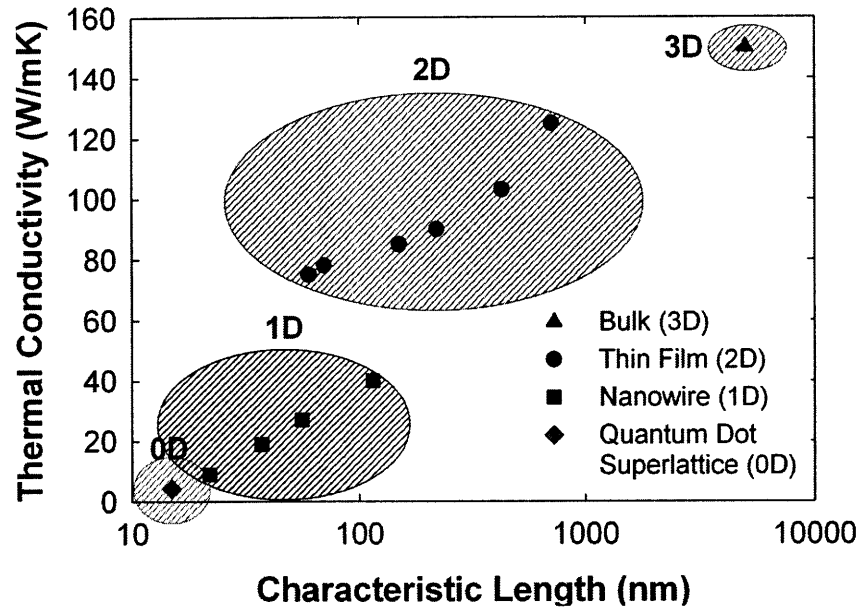


Figure 1.1.4 Dimensional dependence of classical size effects showing how thermal conductivity is reduced from classical size effects as more dimensions are constrained to nanometer length scales, from 3D bulk [32] to 2D thin films [35] to 1D nanowires [34] to 0D quantum dot superlattices [33].

Although it is generally understood that lower dimensionality and smaller characteristic lengths result in lower thermal conductivity for most nanostructures, some low dimensional structures, such as carbon nanotubes (CNTs), actually have high thermal conductivity and exhibit the opposite trend with decreasing diameter, as shown in Fig 1.1.5. Here we see distinctly different behavior between CNTs [9] and nanowires [34], which both have very large aspect ratios. The key difference between CNTs and nanowires, however, is that a CNT is a single molecule and it only supports lattice waves traveling along its axis (1D phonon transport). Nanowires have high aspect ratios, but they also have many unit cells spanning their cross section, which allows modes to propagate in all three-dimensions. Since lattice waves (phonons) can still propagate in 3D, the reduced diameter only serves to increase boundary scattering. CNTs on the other hand exhibit 1D phonon transport, which in turn yields high thermal conductivity. It is also important to note that this high thermal conductivity also increases with decreasing

diameter [9], because the number of modes is reduced and therefore the number of allowable scattering events is reduced, which leads to a longer time between phonon-phonon collisions.

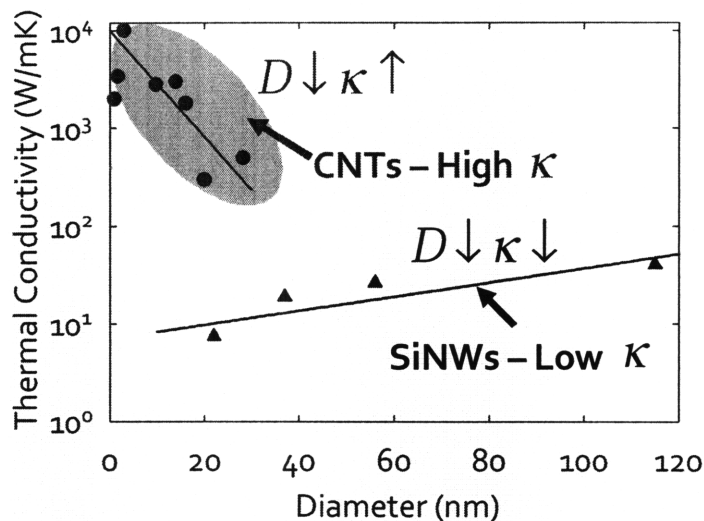


Figure 1.1.5 Thermal conductivity vs. diameter showing opposing trends for silicon nanowires (SiNWs) [34] and CNTs [9].

Although classical size effects can be used to make cheap low thermal conductivity materials, such as ball milled nanocomposites [37], synthesizing cheap high thermal conductivity materials can be even more challenging [2-6]. One approach for developing cheaper high thermal conductivity materials involves mixing CNTs into a bulk polymer or epoxy matrix [2-6]. This approach seeks to enhance the composite thermal conductivity based on reasoning derived from effective medium theories. Under the effective medium assumption, one would expect the high thermal conductivity of CNTs to greatly impact the composite thermal conductivity even at low volume fractions. Experiments, however, show minimal thermal conductivity enhancement (<20 W/mK) [2-6] which indicates that the interfacial resistance between the CNTs and matrix is a fundamental constriction on heat flow.

Another approach for making cheap high thermal conductivity materials involves restructuring bulk polymers themselves. Bulk polymers consist of molecular chains that are highly entangled in a disordered arrangement. The disordered nature of bulk polymers limits their ability to conduct heat, because energy is primarily transported across regions where chains overlap and interact via weak van der Waals forces. A straightened

individual polymer chain molecule, however, can exhibit similar 1D phonon transport characteristics as CNTs, since it only has one dimension of special periodicity. Thus we might expect that individual polymer molecules intrinsically have high thermal conductivity, despite the fact that bulk polymers have low thermal conductivity. Choy *et al.* [18] and Mergenthaler *et al.* [19] have demonstrated the potential for taking advantage of the intrinsic heat conduction characteristics of individual chains by measuring the thermal conductivity of mechanically stretched bulk PE, which is the simplest most widely used polymer. Choy *et al.* [18] were able to increase the thermal conductivity by more than two orders of magnitude, from 0.35 W/mK to 42 W/mK, which is higher than some steels. This strong enhancement is believed to derive from increased chain alignment resulting from the extreme plastic deformation. This [18] and other experiments on mechanically stretched bulk polymers [19] suggest that it may be possible to engineer high thermal conductivity polymer materials, which would have a wide range of applications.

Thus far, Choy *et al.* [18] have reported the highest thermal conductivity measurement of any polymer (42 W/mK). The applications where high thermal conductivity polymers will become relevant depends on the how much thermal conductivity enhancement can be achieved. For example, if the highest achievable thermal conductivity is ~ 42 W/mK, these materials cannot compete with aluminum-based heat sinks or heat exchangers, but could serve as a means of heat spreading in electronic packages, where the plastic encasings often act as an additional thermal barrier to internal component heat dissipation. Since polymers are generally much cheaper to manufacture, high thermal conductivity polymers may become useful in low power thermal management applications, where aluminum heat sinks are too expensive. On the other hand, if it is possible to obtain a thermal conductivity as high as ~ 200 W/mK, these materials could compete with aluminum in higher power thermal management applications, and could also become relevant for heat exchangers in industrial applications such as refrigeration, air conditioning, power plants, chemical processing plants and refineries. These materials would have the added benefit of being lightweight which is important in space and transportation applications, such as satellite electronic package thermal management and automobile radiators. Another attractive aspect of high

thermal conductivity polymers is that they can be electrically insulating. As a result, a material such as high thermal conductivity PE, could be used as to reduce the thermal resistance between superconducting wires and their cryogenic coolant, while simultaneously acting as an electrical insulation barrier.

The key to determining the applications where high thermal conductivity polymers will be relevant is to first quantify the upper limit on its thermal conductivity. Providing an accurate upper limiting estimate and understanding the heat conduction mechanisms can act as a stimulant for further research into large scale manufacturing techniques and optimization methods for specific applications. Intuitively we expect that the upper limiting thermal conductivity for a material consisting of PE chains is the limit of a single chain. A macroscopic material, on the other hand, will consist of many interacting chains, which may have lower thermal conductivity. It will be important to understand both single chains and systems of interacting chains in order to enhance our design intuition. To begin our investigation, we will start with the question of determining the thermal conductivity of a single polymer chain. This question has deep theoretical implications that are discussed in the next section, as it relates to the problem of a 1D chain of nonlinear oscillators.

1.2 Anomalous Heat Conduction in 1D Lattices

In our quest to predict the thermal conductivity of a single PE chain, we first consider the limiting thermal conductivity of a 1D nonlinear chain of oscillators. From statistical mechanics we know that a linear chain of harmonic oscillators (linear forces) is non-ergodic and has infinite thermal conductivity, because the normal modes of vibration are non-interacting and thus there is no source of mode-mode/phonon-phonon scattering [38-40]. Theory suggests that nonlinear particle interactions introduce mode-mode interactions, which in turn give rise to thermal resistance (finite thermal conductivity) through Umklapp scattering [25, 27]. In 1955 however, Fermi, Pasta and Ulam (FPU) showed that a simple model of a nonlinear 1D chain of particles can be non-ergodic, which also implied infinite thermal conductivity [40]. This “remarkable little discovery”

led to the discovery of solitons and gave birth to the modern field of computational nonlinear dynamics [38, 39]. The FPU problem was originally proposed in order to study the system's rate of thermalization and approach to equilibrium. This was based on an expected evolution toward an equipartition of mode energy as a result of the mode-mode interactions induced by the nonlinear particle interactions. Here, the term equipartition implies that, on average, the system's vibrational energy is distributed amongst all the normal modes and is not restricted to a subset of modes. An example plot showing the mode energy with respect to time from the FPU study [40] is shown in Fig 1.2.1. The FPU system consisted of 64 particles and this particular simulation was initialized with all the energy in the lowest frequency mode (mode 1). Figure 1.2.1 shows that nonlinearity does cause mode-mode interactions and the lowest mode's energy decreases as it is exchanged with several other modes. However not all of the system's modes were excited, and after enough time, all of the system's energy returns into the original mode. Since all the system's energy is returned to the lowest frequency mode the entire trajectory repeats itself, which indicates that the system is non-ergodic. This surprising recurrence phenomenon suggests that even an anharmonic chain of oscillators can have infinite thermal conductivity, because the system has infinite memory of its original configuration and the vibrational energy does not diffuse amongst all the modes. To draw a connection between the recurrence phenomenon and heat conduction, it is common to start with the Boltzmann equation and derive an expression, similar in form to (1.1.10), for the thermal conductivity based on phonon transport.

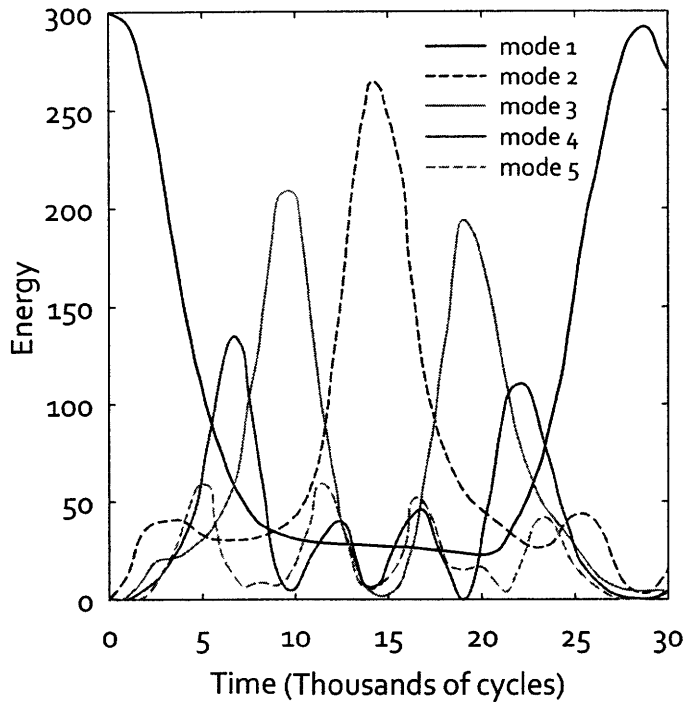


Figure 1.2.1 FPU recurrence phenomenon. This plot shows the energy contained in each normal mode with respect to the simulation time, where the system is initialized with all the energy in the lowest frequency mode labeled mode 1.

From the perspective of the Boltzmann equation, a system having infinite thermal conductivity implies that some phonons do not experience phonon-phonon collisions (Umklapp scattering) and therefore conduct heat ballistically $\tau = \infty$. In the FPU problem, however, phonon-phonon collisions (mode-mode interactions) do occur from the nonlinear forces between particles. How is it that phonon-phonon collisions can occur, giving rise to a finite nonzero scattering rate, and yet the thermal conductivity is still infinite? Over the years, it has proved quite difficult to explain the FPU recurrence phenomenon with Boltzmann equation based arguments [38, 39].

Since the FPU discovery, many important works have provided significant insight into the circumstances required for anomalous transport, as well as possible explanations for the recurrence phenomena [34, 40-62]. For example, in 1965 Zabusky and Kruskal [63] showed that numerical integration of the Korteweg–de Vries equation could lead to stable, solitary waves (solitons) from general initial conditions. These solitons could travel through the media and interact with each other while maintaining their identity [63]. This type of wave propagation would therefore correspond to a mode that does not

scatter/relax, which would imply infinite time between phonon-phonon collisions and infinite conductivity. Another explanation for the recurrence phenomenon, given by Chirikov *et al.* [64, 65], was based on a threshold for dynamical chaos. Chirikov *et al.* showed that an overlap in nonlinear resonance could cause a dynamical instability that would lead to chaotic motion in low dimensional systems. They then used the approach to analytically derive a stochastic threshold, which was later confirmed numerically [66]. These studies explained the FPU recurrence by showing that, in the original report, the initial conditions were below the stochastic threshold and that when initial conditions above the threshold were used, the expected equipartition behavior was observed [64, 65].

Another explanation, provided by Lepri *et al.*, was based on hydrodynamic mode coupling theory. Their explanation [47], suggested that a 1D system is likely to have low frequency modes that behave differently than others. They assert that the dynamical characteristics of these modes can be described by mode coupling theory, which implies that they diffuse over a much longer time scale than other modes in the system. This difference in time scales allows these modes to propagate without fully attenuating, leading to an infinite memory, which then causes the thermal conductivity to diverge $\kappa \rightarrow \infty$. It is unclear, however, whether or not these explanations would apply to a more complicated model of an individual polymer chain and questions surrounding the circumstances required for anomalous heat conduction continue to linger [38, 39].

1.3 Polymer Chain Modeling

In establishing a connection between the many previous works on anomalous heat conduction in 1D lattices [34, 40-62] and thermal transport in single polymer chains, it is important to address their similarities and differences. Previous models are similar to single polymer chains in the sense that they only have one dimension of spatial periodicity for the atomic arrangement. Most of these studies [34, 40-62], however, used simplified toy models, which do not accurately represent the more complicated many-body interactions in a real polymer chain. In fact, most works have investigated fictitious

systems, where the interactions between particles were simply chosen for better understanding of the circumstances required for infinite conductivity.

For example, Casati *et al.* [42] used a ding-a-ling model to show that chaos is essential for convergent behavior. The ding-a-ling model is not intended to represent a physically meaningful system, as it consists of linear chain of hard colliding spheres, where every other hard sphere is bound to its lattice site with a harmonic potential while the other hard spheres are unbound and free to collide with their nearest neighbors. This model aided in uncovering some of the underlying physics and necessity of chaos [42], but does not provide directly applicable insight into the behavior of polymer chains. Prosen and Robnik [67] later showed that the free particle collisions were not necessary for normal transport behavior, by investigating the ding-dong model, which only consists of hard spheres that are bound to their lattice site with a harmonic potential. For this model [67], there is an obvious threshold, where the atoms must deviate far enough from their lattice site to cause elastic collisions with neighboring spheres, otherwise the system evolves as a group of independent oscillators. Nonetheless, Prosen and Robnik [67] showed that these hard sphere collisions between oscillators were sufficient for introducing enough randomization (chaos) for normal convergent thermal conductivity. These works [42, 67] helped to establish that some 1D lattice models do behave normally and do not exhibit anomalous transport (diverging thermal conductivity).

Although hard sphere collision systems exhibited normal transport characteristics, a series of investigations involving Toda's lattice model [45, 68, 69] revealed that other nonlinear oscillator models, other than the FPU model, showed divergent behavior. The Toda lattice consisted of point masses connected via an exponentially decaying potential. Toda showed that this system can be studied analytically and has normal modes [69], while others such as Hatano [45], demonstrated its capacity to exhibit divergent thermal conductivity. Another more recent example, where toy models were used to examine the thermal conductivity more specifically, was that of Li and Li [70]. Here, the authors tested and compared various toy models [70], including harmonic models with cosine functions as onsite potentials, as well as slightly extended versions of the original FPU model, such as the FPU- α , FPU- β and FPU- $\alpha\beta$ models. This study [70] showed that the temperature dependence of the thermal conductivity depended on the strength of the

nonlinearity and that different trends could be obtained by changing the model parameters. Although these works helped to uncover some of the fundamental physics associated with heat conduction in 1D lattices [42, 45, 56, 67, 70], the results provide little insight into the expected behavior of more complicated single polymer chains. In the preceding examples, as well as many others [40-44, 46-62], the models were chosen for elucidation of the underlying physics and were not necessarily based on physically motivated considerations. As a result, the evidence and conclusions in these works cannot be extended to predict the behavior of an individual polymer chain in a straightforward manner.

In a real polymer chains, such as PE, there are strong covalent forces between bonded atoms separated by short distances and weaker van der Waals forces between atoms separated by larger distances. Figure 1.3.1 identifies the carbon and hydrogen atoms in two PE chains along with the two distinctly different types of interactions. In general, the covalent interactions between bonded atoms are complicated, because they are very sensitive to the positions of surrounding atoms, as well as their bonding angles and local coordination. This is because the atomic interactions are fundamentally governed by the electron density, which is most sensitive to the closest nucleic positions. Solving the many-body electron problem, however, is currently too computationally expensive for the systems of interest. In light of this difficulty, many schemes for approximating the effective Coulombic interactions have been developed, with varying degrees of complexity, realism and accuracy.

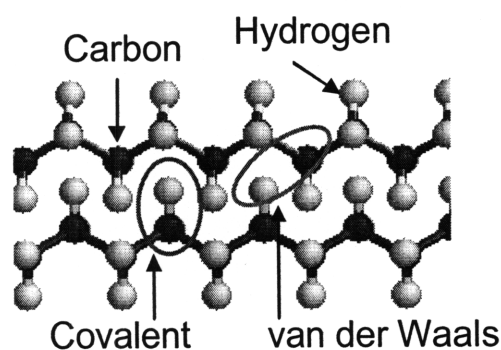


Figure 1.3.1 Two neighboring polyethylene chains. Covalently bonded atoms are connected by smaller cylinders. Ellipses identify pairs of atoms that experience each of the two types of bonding.

To our knowledge the most realistic model that has been used for studying the thermal conductivity of a single polymer chain was that of Freeman, Morgan and Cullen [71]. Their study employed the Kirkwood model [72], which uses a united-atom (UA) representation to describe the vibrational modes of a zig-zag PE chain molecule in two dimensions. UA models reduce the total number of degrees of freedom in a MD simulation by lumping atoms together to form a single pseudo-atom rigid body. In the case of the Kirkwood model for PE, each pair of hydrogen atoms is lumped together with a carbon atom to form CH_2 pseudo-atom units, such that the total number of degrees of freedom is reduced by a factor of three. The UA representation also allows for a time step that is ~ 4 times larger, because the high velocity hydrogen motions no longer need explicit treatment. These two benefits together allow for at least an order of magnitude reduction in computational cost, as compared to a fully explicit treatment of each atomic species. Sumpter *et al.* [73] have discussed the ramifications of the UA simplification on the structural properties of PE. For the thermal/phonon transport properties, however, the Kirkwood model is oversimplified and neglects several important features that are present in real PE chains.

One issue is that Kirkwood's use [72] of the UA approximation and limited vibrational degrees of freedom (2D) significantly reduces the number of modes present in the simulations, from 18 polarizations in a real chain (6 basis atoms with 3 degrees of freedom) to 4 polarizations in the Kirkwood model (2 basis atoms with 2 degrees of freedom). If many of the system's modes are nonexistent in the model, the resultant thermal conductivity, which is a consequence of the many different types of mode-mode interactions, becomes questionable. The second issue in the Kirkwood model is that the atomic interactions are highly simplified, consisting of only harmonic bond stretching and harmonic bond bending. Although it is a harmonic interaction based approach, nonlinearity arises from cross-terms generated by expansion of the interatomic forces. The interactions in a real PE chain, however, will be more complicated because of many body effects that arise from the electron density's sensitivity to the respective locations of neighboring atomic nuclei.

Another feature that is absent in the Kirkwood model is the treatment of van der Waals interactions. These weaker, longer ranged interactions derive from the attraction

between the nucleus of one atom and the electron clouds of other atoms to which they are not covalently bonded. Van der Waals forces are an order of magnitude smaller than covalent forces, but their long range nature allows whole polymer chain molecules to form a minimum energy lattice structure. In the case of PE, the lattice structure is orthorhombic as shown in Fig. 1.3.2, where the chain axis extends perpendicular to the viewing plane [1]. The unit cell contains two chains and each is rotated by ~ 30 degrees from the primitive cell vectors to minimize the hydrogen atom repulsion.

For a single chain, the phonon transport is one-dimensional, because all of the normal mode wave vectors point in the z direction along the chain backbone, since it is the only direction of spatial periodicity. When multiple chains are allowed to interact they can minimize their energy by forming the bulk lattice structure shown in Fig. 1.3.2. In the bulk lattice structure additional modes are present, which arise from the relative vibrations between whole molecules. These modes propagate in the other two dimensions at various angles from the chain backbone and have both lower frequencies and group velocities because of the weaker van der Waals stiffness. As a result, the bulk lattice structure supports three-dimensional phonon transport, which is common to most bulk materials and nanostructures. Thus we can anticipate a dimensional transformation in phonon transport as we move from studying 1D transport in single chains to 3D transport in the bulk lattice structure.

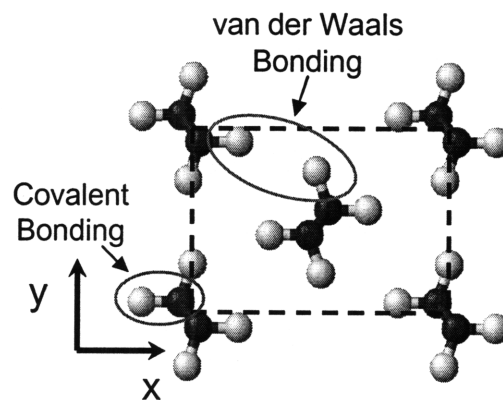


Figure 1.3.2 Polyethylene bulk lattice structure. Dashed lines indicate the unit cell, while ellipses identify the two types of bonding present.

For most nanostructures, reducing their size reduces their thermal conductivity, because of enhanced boundary scattering of phonons caused by an increased surface area

to volume ratio. Polymer chain lattices however may exhibit different behavior because of the strong anisotropy in bond chemistry, with stiff covalent bonds in the axial direction and weak van der Waals bonds in the lateral directions. Since each polymer chain is likely to have high thermal conductivity by itself, additional chains may detract from the axial conductivity by imposing chain-chain van der Waals interactions, which in turn act as an additional phonon-phonon scattering mechanism. Adding chains however, also opens up new paths for heat conduction, which can enhance the thermal conductivity. The interplay between these two effects will determine whether or not the thermal conductivity will exhibit the opposite trend observed in most nanostructures. We anticipate that the phonon scattering effect of the van der Waals interactions will dominate, which will give rise to a dimensional transformation in the thermal conductivity as it corresponds with the dimensional transformation in phonon transport.

1.4 Objectives

In an idealized infinitely long polymer chain lattice, the weakly attractive van der Waals forces between chains give rise to a lattice structure in both 2D and 3D. This unique feature allows for the observation of both a 1D-to-2D and 2D-to-3D transition in phonon transport. In the remainder of this thesis, we will begin from the limiting behavior of an infinitely long single PE chain. Upon starting from a single PE chain, which is expected to have high thermal conductivity, we anticipate a transition to 2D behavior as more chains are added to form a single lattice plane (1D-to-2D transition). The 2D lattice plane should then exhibit lower thermal conductivity, as a result of anharmonic scattering induced by neighboring chains. A second transition from 2D to 3D is also expected as additional lattice planes are stacked, leading to even more chain-chain anharmonic scattering, which should lower the thermal conductivity even further. As a result, we expect that the strongly anisotropic bond chemistry in PE chain lattices may cause the axial thermal conductivity to increase with decreasing crystal size, which is the opposite trend observed in most materials [24, 34]. These transitional behaviors will be probed

with molecular dynamics (MD) simulations and analyzed using linear response theory approaches along with modal analysis techniques.

For the specific case of PE, several experiments have provided evidence to support the notion that individual polymer chains may intrinsically have high thermal conductivity, but only in the direction of the chain’s carbon backbone. In both sets of experiments conducted by Choy *et al.* [18] and Mergenthaler *et al.* [19], the mechanical stretching of bulk PE resulted in more than two orders of magnitude increase in the thermal conductivity along the stretching direction, while the thermal conductivity in the perpendicular directions remained largely unchanged. Choy *et al.* [18] in particular reported that spectroscopic measurements of their most stretched samples ($L_{final}/L_{initial} > 300$), which showed thin crystal needle structures. Their measurements shown in Fig. 1.4.1 indicate that the thermal conductivity is initially very sensitive to stretching, but appears to approach an asymptotic value at the highest stretch ratios. This asymptotic value may correspond to the bulk crystalline value and we will use their measurements as a basis for comparison with our calculations for the upper limiting thermal conductivity of a single crystal (3D).

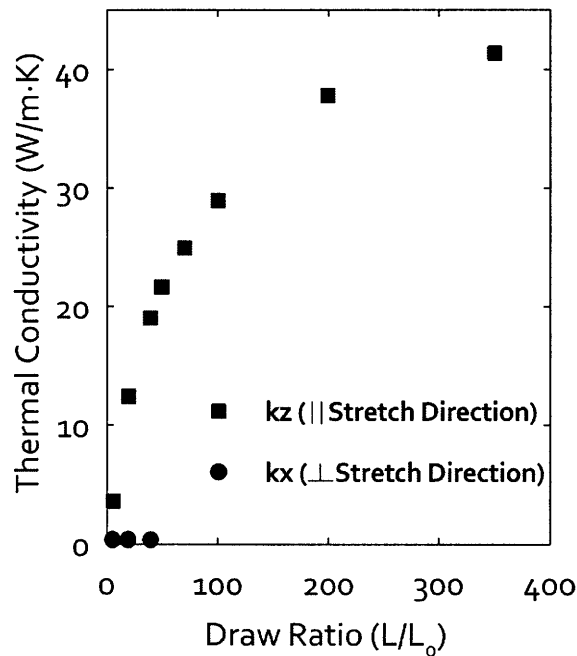


Figure 1.4.1 Thermal conductivity of mechanically stretched bulk polyethylene [18]. The draw ratio is based on the final and initial sample lengths L and L_0 respectively.

In the remaining chapters we provide a discussion of our MD simulation implementation, the potential energy model used, and the simulation procedures. We then present the analytical framework used to interpret the atomic trajectories. These analysis techniques are based on incorporation of results from linear response theory [24, 74], lattice dynamics [23], the Boltzmann equation [24] as well as a spatial Fourier transform technique [23, 30]. We then present the results of over 300 independent simulations of single PE chains and various sizes of PE lattices to address the issues outlined in this chapter. Finally, we provide concluding remarks that encompass the theoretical advancements achieved, as well as the physical insight gained with respect to the details of phonon transport in PE.

Chapter 2: Molecular Dynamics Simulations

In this chapter we introduce a numerical method, termed molecular dynamics (MD) [75], which can be used to investigate the fundamental properties of materials by simulating the atomic motion. Many fundamental parameters, such as phonon mean free paths, are difficult to determine analytically or experimentally and therefore numerical techniques, such MD simulations, are a powerful alternative. Although MD simulations can be used to study a wide variety of phenomena, the present investigation is focused on the vibrational properties, which give rise to phonon transport phenomena. In this chapter we introduce the theory of MD simulations and briefly discuss how it can be implemented on a parallel computing architecture.

2.1 The Theory of Molecular Dynamics Simulations

In classical mechanics the motion of rigid bodies is governed by Newton's equation of motion. Under the classical framework, a body's position, velocity and acceleration are all calculated deterministically in response to the forces acting on it. Quantum mechanics, on the other hand, treats material bodies probabilistically, as waves whose spatial makeup is determined by solving Schrodinger's equation [21]. In the classical framework, two bodies cannot occupy the same space, while in the quantum framework, individual material waves can overlap leading to interference phenomena [21].

MD simulations model the motion of atoms by treating each atom as a point particle that obeys classical equations of motion. MD simulations track the trajectory of particles by sequentially integrating the equations of motion to determine each atom's position after fixed time intervals. In classical MD simulations, Newtonian dynamics are used to relate forces to particle accelerations through

$$\vec{\mathbf{F}} = m \cdot \frac{d^2 \vec{\mathbf{r}}}{dt^2} \quad (2.1.1)$$

where \vec{F} is the net force, m is the particle's mass and $\frac{d^2\vec{r}}{dt^2}$ is its acceleration. In MD simulations the forces are calculated from a model for the system's potential energy. The potential energy model is thus the most important component of MD simulations, because its accuracy in describing the interactions is crucial for accurate and realistic results. Most often, potential models are functions of the atomic nuclei positions and do not include velocity contributions. This is because most models attempt to provide an effective treatment of Coulombic interactions, which only depend on the relative locations of charged particles. Once the model for the potential energy Φ has been chosen, the force on each particle can be determined by

$$\vec{F}_i = -\frac{\partial\Phi}{\partial\vec{r}_i} \quad (2.1.2)$$

where \vec{F}_i is the force on a particle labeled i . The relationship between force and energy in (2.1.2) ensures that particles adjust their positions to minimize the system's potential energy. Once the potential model, initial positions, and initial velocities are specified, the force on each particle can be calculated numerically, based on the analytical derivative of the potential energy. The positions, velocities and calculated forces can then be used to predict the future position of each particle using an algorithm to integrate the equations of motion. The simplest and most popular is the Verlet algorithm [75], which is based on a forward and backward Taylor expansion of a particle's position in time. By adding,

$$\vec{r}_i(t + \Delta t) = \vec{r}_i(t) + \vec{v}_i(t) \cdot \Delta t + \frac{\vec{F}_i}{2 \cdot m_i} \cdot (\Delta t)^2 \quad (2.1.3)$$

and

$$\vec{r}_i(t - \Delta t) = \vec{r}_i(t) - \vec{v}_i(t) \cdot \Delta t + \frac{\vec{F}_i}{2 \cdot m_i} \cdot (\Delta t)^2 \quad (2.1.4)$$

we can arrive at

$$\vec{r}_i(t + \Delta t) = 2 \cdot \vec{r}_i(t) - \vec{r}_i(t - \Delta t) + \frac{\vec{F}_i}{m_i} \cdot (\Delta t)^2 \quad (2.1.5)$$

where the velocity is calculated as

$$\vec{v}(t) = \frac{\vec{r}_i(t + \Delta t) - \vec{r}_i(t - \Delta t)}{2 \cdot \Delta t} \quad (2.1.6)$$

$\bar{\mathbf{r}}_i(t + \Delta t)$ is the particle's predicted position, $\bar{\mathbf{r}}_i(t)$ is its current position, $\bar{\mathbf{r}}_i(t - \Delta t)$ was its previous position, $\bar{\mathbf{v}}(t)$ is its velocity, $\frac{\bar{\mathbf{F}}_i}{m_i}$ is its acceleration and Δt is the specified time step. Since the velocity is calculated based on the predicted position, obtained from the algorithm itself, the Verlet algorithm is generally more stable than the forward or backward schemes alone [75]. This is because it uses the acceleration, present and previous positions as inputs and not the velocity, which contains numerical error from the current time step. With this scheme, the future positions are computed iteratively to determine the system's trajectory. Even more stable and accurate algorithms exist. However they have increased complexity and computational expense [75].

The last component to a MD simulation is the specification of initial and boundary conditions. Typical simulations start with particles at equilibrium positions and initial velocities that correspond to a desired temperature. It is this natural inclusion of temperature that makes MD ideal for the investigation of temperature-dependent phenomena. The specification of boundary conditions depends on the problem of interest, but wherever possible it is common to impose periodic boundary conditions to imitate an infinite medium. Periodic boundaries are useful because the size and timescale of MD simulations are the limiting factors in its implementation. Periodic boundaries are natural conditions that reflect microcanonical statistics, because they inherently conserve the number of particles, energy and volume [75].

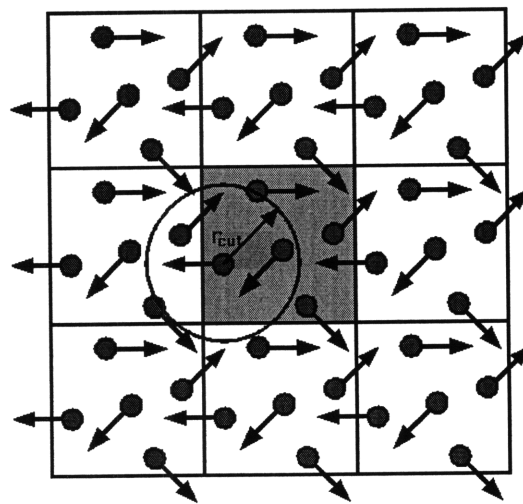


Figure 2.1.1 Two-dimensional illustration of periodic boundary conditions

Figure 2.1.1 shows how periodic boundary conditions are implemented in a two-dimensional simulation domain. As atoms move beyond boundaries they reenter through opposite sides so that the particle interactions are geometrically cyclic, preserving energy and volume in a simulation cell. Periodic boundaries can be implemented by copying the particle positions, such that the atoms on one side of the domain interact with the atoms on the opposite side of the domain [75]. This is a feature that naturally works with rectangular domains, which is the most common choice for the domain shape.

Other boundary conditions have been developed for simulating constant temperature and constant pressure ensembles that involve rescaling the equations of motion, such as the Nose-Hoover thermostat. Nonequilibrium boundary conditions also exist and are often used to study transport. Velocity rescaling is a nonequilibrium boundary condition that alters the atomic trajectory in order to impose heat fluxes and induce a temperature gradient [75, 76]. The thermal conductivity can be calculated with these boundary conditions by inverting the temperature gradient in accordance with Fourier's law [76],

$$\mathbf{Q} = -\kappa \cdot \vec{\nabla} T \quad (2.1.7)$$

where \mathbf{Q} is the heat flux, κ is the thermal conductivity and $\vec{\nabla} T$ is the temperature gradient. Although this approach for determining the thermal conductivity is intuitive, nonequilibrium techniques have several drawbacks.

One issue is that the atomic vibration in regions where the boundary conditions are applied becomes unnatural. Here, the vibrational dynamics in the boundary regions are no longer solely governed by the interatomic potential, and therefore velocity modifications introduce an artificial mechanism for the phonon scattering. For properties such as the thermal conductivity, which are based on phonon scattering, this effect can have a strong impact on the results. Studies employing this approach typically observe size effects on the thermal conductivity and can require large simulation domains for convergence of the results. This issue is most problematic for high thermal conductivity materials, with long phonon mean free paths, because the results will not converge unless the simulation domain is larger than the mean free paths [76].

A second issue with nonequilibrium approaches arises as a consequence of the length scale limitations in MD simulations. In many studies, computational resources are

limited, which constrains the maximum size of the simulation domain that can be studied. As a result, most MD simulation domains are nanometers in length. This can become problematic when generating temperature gradients that are large enough to detect. If the domain is small, large heat fluxes on the order of MW/m are required to generate single degree temperature differences. When considering that the temperature fluctuations in MD simulations are on the order of ± 10 degrees, a serious problem for the signal to noise ratio arises, and it is often difficult to determine thermal conductivity reliably [76]. Equilibrium methods, on the other hand, allow for natural atomic vibrations without boundary artifacts introduced by trajectory modifications. A common drawback to equilibrium techniques, however, is the necessity for long time simulations, which are needed for sufficient sampling of the statistical fluctuations [29, 77].

2.2 Interatomic Potentials

The potential energy model is the essential feature of MD simulations that determines the dynamics and therefore the validity of the results. Most potential models fall between two categories, *ab initio*/quantum and empirical/classical. In general, modeling atomic interactions involves approximate solution of a nonlinear N-body problem, where the speed and simplicity of empirical models is traded at the expense of accuracy and realism, which is maintained to a higher degree with *ab initio* methods. In MD simulations the most expensive portion of the calculation is numerical computation of the forces. As a result MD simulations are usually limited by processor speed as opposed to available memory and careful considerations should be taken when choosing a potential model, so that an optimal balance of accuracy and speed is achieved.

Ab initio techniques are highly accurate because they typically involve a minimization scheme to determine the coefficients of basis functions, which are used to describe N interacting electrons obeying Schrodinger's equation. Once the electron wave function, or pseudo-wave function has been determined, the force acting on each atom can be calculated by numerically integrating the Coulombic contributions from the

charge distribution. The high degree of accuracy associated with *ab initio* approaches [78, 79], however, is accompanied by an extremely large computational expense, in comparison to empirical and semi-empirical methods.

Despite the large computational requirements, *ab initio* calculations have become popular in recent years due to advancements by Walter Kohn and John Pople, who received a Nobel prize in 1998 for developing density functional theory (DFT). In DFT the assumption is made that all electrons occupy their ground state and the Schrodinger equation is solved for a pseudo-electron wave function [78, 79]. In DFT the valence electrons are treated as degrees of freedom, while the core electrons and nuclei are represented by pseudopotentials. Under this approach, the electronic structure of virtually any material can be determined. By knowing the electronic structure, highly accurate forces can be calculated based on very few underlying assumptions. Excellent agreement between DFT calculations and experiments has been observed for a variety of material properties [78, 79]. In quantum molecular dynamics (QMD) the wave function is recalculated after every time step, which limits the size and length of simulations to a few hundred atoms and picoseconds. These limitations render QMD inappropriate for the purpose of this investigation. However, as computer hardware advances it may eventually become a feasible option. Other semi-empirical techniques, such as tight binding and molecular orbital based methods, lie in between quantum and classical models with varying accuracy and computational expense. Next we shift focus to classical potentials, which have the least computational expense, because the system of interest requires multiple nanosecond simulations of thousands of atoms.

Since empirical potentials, for many material systems, were developed before DFT, they have been widely used in MD studies. Empirical potentials are usually developed by first creating a physically motivated functional form. Potential parameters embedded in the function are then determined by fitting to experimental data. Most commonly, functional forms are developed for certain types of bonding, and are usually based on a physical observation or intuition about the associated electron states or effective coulomb interactions. Once the functional form is chosen and the parameters have been determined, the potential is most often tested by comparing material properties calculated with the potential, to a variety of experimental data. More recently, results

from *ab initio* calculations have been used for comparison and in some cases have been used in the initial determination of the free parameters via the force matching method [80].

One of the mostly widely used empirical potentials was developed by Lennard and Jones and is commonly called the Lennard-Jones (LJ) potential [75]. This potential's functional form was physically motivated by the separation dependence of dipole-dipole van der Waals interactions. In dipoles, positively charged nuclei experience a screened attraction to the electrons of surrounding atoms. By summing these Coulombic contributions, it can be shown analytically that the potential energy between neighboring dipoles decays varies as $\frac{1}{\|\mathbf{r}\|^6}$, where $\|\mathbf{r}\|$ is the dipole separation. As a result, the famous

Lennard-Jones 6-12 potential for a system of N dipoles was developed with the following functional form,

$$\Phi = \sum_{i=1}^N \sum_{\substack{j=1 \\ j \neq i}}^N -4 \cdot \varepsilon \cdot \left[\left(\frac{\sigma}{\|\mathbf{r}_{ij}\|} \right)^6 - \left(\frac{\sigma}{\|\mathbf{r}_{ij}\|} \right)^{12} \right] \quad (2.2.1)$$

where Φ is the potential energy, the subscripts i and j denote atomic indices, ε is the minimum energy, σ is the minimum energy length scale and $\|\mathbf{r}_{ij}\|$ is the dipole separation. The 12th power term in the potential represents the repulsive interactions that dominate at very close distances and prevent atoms from fusing together. The exponent in this portion of the potential, however, is not uniquely motivated by physical considerations. Instead, the 12th power repulsive exponent is commonly used to simplify

the computation, where $\left(\frac{\sigma}{\|\mathbf{r}\|} \right)^6$ is computed first and $\left(\frac{\sigma}{\|\mathbf{r}\|} \right)^{12}$ is obtained by squaring the stored result. Other large repulsive exponents, such as 13 or 14 can also be used with minimal impact on the results [75].

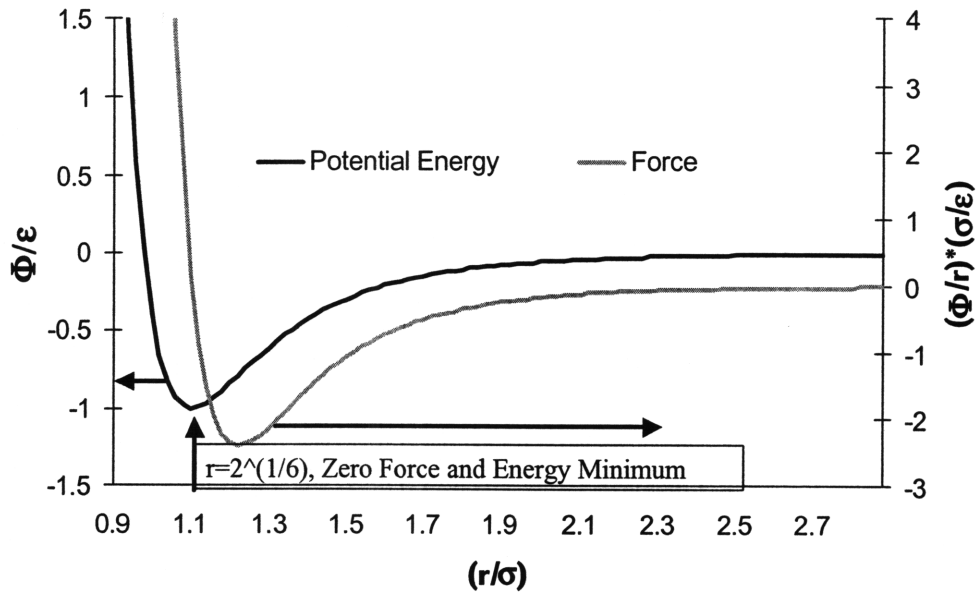


Figure 2.2.1 Lennard-Jones potential and force

Figure 2.2.1 shows a plot of the Lennard-Jones potential energy and force as a function of increasing distance. The forces are largely repulsive at short distances and decrease to zero at the equilibrium distance $\sigma^{1/6}$, where the repulsion is balanced by the van der Waals attraction. Beyond that distance, the van der Waals forces are weakly attractive and extend to infinite dipole separation. The balance between attractive and repulsive forces is a common theme in empirical potential development. Most models include an attractive term that dominates for large separations and a repulsive term for short distances when valence electron orbitals overlap. The Lennard-Jones potential has been widely used and has shown the best agreement with noble gases. This is because their valence electron shells are completely filled, thus there is no shared electron bonding and the interactions are dominated by dipole-dipole van der Waals forces.

Most materials in nature, however, cannot be wholly described by van der Waals interactions. Some materials can be described with only pair-wise attraction and repulsion, however many covalently bonded systems, such as semiconductors and polymer chains require inclusion of higher order many-body interactions. For covalently bonded hydrocarbon systems the interactions are quite complicated and depend on the local bond angles, coordination and dihedral angles. One of the most successful empirical potentials used to describe various configurations of hydrocarbon bonding was developed

by Brenner [81]. Brenner’s reactive empirical bond order (REBO) potential was designed for simulations of reactive systems where the bonds do not need to be pre-specified, but can break and form dynamically. Brenner’s pioneering work [81] has been highly successful and has been widely used to study diamond [82], carbon nanotubes [76], graphene and polymers [83].

2.3 The Adaptive Intermolecular Reactive Empirical Bond Order Potential (AIREBO)

Brenner’s REBO potential [81] is restricted to covalent bonding systems and uses a cut-off function to truncate the interactions at 2 Å. Although it has been largely successful, it is insufficient for studying many systems of interest where interactions beyond 2 Å are important. This inability to treat other types of interactions limits its applicability. For example, REBO can be used to study individual graphene sheets, but cannot be used to study graphite, where multiple layers are stacked with an inter-layer separation of ~ 3.4 Å. This issue also arises with multi-walled carbon nanotubes and polymer chain lattices. To alleviate this constraint, Stuart *et al.* [83] built on Brenner’s work by adding two additional terms to form the adaptive intermolecular reactive empirical bond order potential (AIREBO), where the potential energy is written as,

$$E = \sum_i \sum_{j>i} \left[E_{ij}^{REBO} + E_{ij}^{LJ} + \sum_{k \neq i, j} \sum_{l \neq i, j, k} E_{kijl}^{TORS} \right] \quad (2.3.1)$$

Here, E_{ij}^{REBO} is the Brenner potential, E_{ij}^{LJ} is a Lennard-Jones potential which is used for treating more long ranged van der Waals interactions and E_{kijl}^{TORS} is a four-body potential that shows preference to certain bonding angles in polymeric systems. The covalent bonding described by the pair-wise REBO energy consists of an attractive term V_{ij}^A and repulsive term V_{ij}^R given by [83],

$$E_{ij}^{REBO} = V_{ij}^R + b_{ij} \cdot V_{ij}^A \quad (2.3.2)$$

where the repulsive term V_{ij}^R is given by,

$$V_{ij}^R = w_{ij}(r_{ij}) \left[1 + \frac{Q_{ij}}{r_{ij}} \right] A_{ij} \exp(-\alpha_{ij} r_{ij}) \quad (2.3.3)$$

In equation (2.3.3), r_{ij} is the distance between atoms i and j , and $w_{ij}(r_{ij})$ is the short ranged cut-off function that terminates the interactions beyond 2 Å,

$$w_{ij}(r_{ij}) = S'(t_c(r_{ij})) \quad (2.3.4)$$

$$S'(t) = \Theta(-t) + \Theta(t)\Theta(1-t) \cdot \frac{1}{2} [1 + \cos(\pi t)] \quad (2.3.5)$$

$$t_c(r_{ij}) = \frac{r_{ij} - r_{ij}^{\min}}{r_{ij}^{\max} - r_{ij}^{\min}} \quad (2.3.6)$$

In equation (2.3.5), Θ is the Heaviside step function and all other unspecified quantities are constants that depend on the species of atoms i and j (carbon or hydrogen). The repulsive interaction of the REBO potential is balanced by the attractive term V_{ij}^A , which is given by a summation of three exponential functions that are indexed by integer n ,

$$V_{ij}^A = -w_{ij}(r_{ij}) \sum_{n=1}^3 B_{ij}^{(n)} \exp(-\beta_{ij}^{(n)} r_{ij}) \quad (2.3.7)$$

In equation (2.3.7), the superscripted (n) signifies that each term of the summation has different constants $B_{ij}^{(n)}$ and $\beta_{ij}^{(n)}$ that depend on the interacting species i and j . In a bond order potential, the attraction between pairs of atoms is mitigated by a bond order, which contains the many-body aspects of the relevant physics. For the REBO potential the bond order b_{ij} depends on the local carbon and hydrogen coordination numbers N_{ij}^C and N_{ij}^H , respectively, as well as the conjugated coordination N_{ij}^{conj} , the triplet bond angle $\theta_{jik} = \frac{\mathbf{r}_{ij} \cdot \mathbf{r}_{ki}}{\|\mathbf{r}_{ij}\| \|\mathbf{r}_{ki}\|}$ and the dihedral bond angle ω_{kijl} . In the REBO energy term, the

bond order is written as the summation of four quantities $p_{ij}^{\sigma\pi}$, $p_{ji}^{\sigma\pi}$, π_{ij}^{RC} , π_{ij}^{DH} that can impact the strength and character of the covalent bonding between neighboring atoms,

$$b_{ij} = \frac{1}{2} [p_{ij}^{\sigma\pi} + p_{ji}^{\sigma\pi}] + \pi_{ij}^{RC} + \pi_{ij}^{DH}. \quad (2.3.8)$$

The principal portion of the bond order b_{ij} comes from $p_{ij}^{\sigma\pi}$ and $p_{ji}^{\sigma\pi}$, which penalize bonds that are too close together. These two quantities depend on the local bond angles and coordination of surrounding atoms and are given by,

$$P_{ij}^{\sigma\pi} = \left[1 + \sum_{k \neq i, j} w_{ik}(r_{ik}) \cdot g_i(\cos(\theta_{jik})) \exp(\lambda_{jik}) + P_{ij} \right]^{-1/2} \quad (2.3.9)$$

where N_{ij} is the coordination number that depends on the number of neighboring carbon N_{ij}^C and hydrogen atoms N_{ij}^H ,

$$N_{ij} = N_{ij}^C + N_{ij}^H \quad (2.3.10)$$

$$N_{ij}^C = \left(\sum_{k \neq i} \delta_{kC} w_{ik}(r_{ik}) \right) - \delta_{jC} w_{ij}(r_{ij}). \quad (2.3.11)$$

The three-body angular dependence of the bond order comes from 5th order spline functions $g_C^{(1)}$ and $g_C^{(2)}$,

$$g_C(\cos(\theta_{jik})) = g_C^{(1)}(\cos(\theta_{jik})) + S'(t_N(N_{ij})) [g_C^{(2)}(\cos(\theta_{jik})) - g_C^{(1)}(\cos(\theta_{jik}))] \quad (2.3.12)$$

where,

$$t_N(N_{ij}) = \frac{N_{ij} - N_{ij}^{\min}}{N_{ij}^{\max} - N_{ij}^{\min}}. \quad (2.3.13)$$

In equation (2.3.9), λ_{jik} , which is given by,

$$\lambda_{jik} = 4\delta_{iH} [(\delta_{kH}\rho_{HH} + \delta_{kC}\rho_{CH} - r_{ik}) - (\delta_{jH}\rho_{HH} + \delta_{jC}\rho_{CH} - r_{ij})] \quad (2.3.14)$$

and the two dimensional spline $P_{ij}(N_{ij}^C, N_{ij}^H)$ were added as correction factors for certain coordination and bond configurations. The bond order, b_{ij} , involves tabulated multi-dimensional splines, such as $P_{ij}(N_{ij}^C, N_{ij}^H)$, $g_C^{(1)}(\cos(\theta_{jik}))$ and $g_C^{(2)}(\cos(\theta_{jik}))$, but b_{ij} also depends on $\pi_{ij}^{RC}(N_{ij}, N_{ji}, N_{ij}^{conj})$ and $T_{ij}(N_{ij}, N_{ji}, N_{ij}^{conj})$, which depend on the conjugated coordination number N_{ij}^{conj} ,

$$N_{ij}^{conj} = 1 + \left(\sum_{k \neq i, j} \delta_{kC} w_{ik}(r_{ik}) S'(t_{conj}(N_{ki})) \right)^2 + \left(\sum_{l \neq i, j} \delta_{lC} w_{jl}(r_{jl}) S'(t_{conj}(N_{lj})) \right)^2 \quad (2.3.15)$$

$$t_{\text{conj}}(N) = \frac{N - N_{ij}^{\min}}{N^{\max} - N^{\min}} \quad (2.3.16)$$

The dihedral angular dependence of b_{ij} is contained in π_{ij}^{DH} , which is given by,

$$\pi_{ij}^{DH} = T_{ij} \cdot \sum_{k \neq i, j} \sum_{l \neq i, j} \left[(1 - \cos^2(\omega_{kijl})) \cdot w'_{ik}(r_{ik}) w'_{jl}(r_{jl}) \Theta(\sin(\theta_{jik}) - s^{\min}) \Theta(\sin(\theta_{ijl}) - s^{\min}) \right] \quad (2.3.17)$$

where the dihedral angle cosine $\cos(\omega_{kijl})$ is computed from,

$$\cos(\omega_{kijl}) = \frac{\mathbf{r}_{ji} \times \mathbf{r}_{ik}}{\|\mathbf{r}_{ji} \times \mathbf{r}_{ik}\|} \cdot \frac{\mathbf{r}_{ij} \times \mathbf{r}_{jl}}{\|\mathbf{r}_{ij} \times \mathbf{r}_{jl}\|}, \quad (2.3.18)$$

and the dihedral interaction is truncated by the cut-off function $w'_{ij}(r_{ij})$,

$$w'_{ij}(r_{ij}) = S'(t'_c(r_{ij})) \quad (2.3.19)$$

where

$$t'_c(r_{ij}) = \frac{r_{ij} - r_{ij}^{\min}}{r_{ij}^{\max} - r_{ij}^{\min}}. \quad (2.3.20)$$

Equations (2.3.2)-(2.3.20) comprise the REBO portion of the AIREBO potential, which describes covalent bonding between atoms separated by less than 2 Å. All quantities that are not explicitly listed are constants that depend on the interacting atomic species and can be found elsewhere [83]. The major advancement of the AIREBO potential was the addition of an adaptable LJ potential, which is controlled by switching functions that depend upon the local bonding environment,

$$E_{ij}^{LJ} = S(t_r(r_{ij})) S(t_b(b_{ij}^*)) C_{ij} V_{ij}^{LJ}(r_{ij}) + [1 - S(t_r(r_{ij}))] C_{ij} V_{ij}^{LJ}(r_{ij}) \quad (2.3.21)$$

where V_{ij}^{LJ} is the commonly used Lennard-Jones 6-12 potential

$$V_{ij}^{LJ}(r_{ij}) = 4\epsilon_{ij} \left[\left(\frac{\sigma_{ij}}{r_{ij}} \right)^{12} - \left(\frac{\sigma_{ij}}{r_{ij}} \right)^6 \right]. \quad (2.3.22)$$

The addition of a LJ potential to the short ranged REBO potential is non-trivial, because the LJ potential must only have its effect on specific pairs of atoms that are not covalently bonded. The switching functions $S(t)$ in (2.3.21), are used to mitigate the 12th power repulsive term in V_{ij}^{LJ} ,

$$S(t) = \Theta(-t) + \Theta(t) \Theta(1-t) [1 - t^2(3-2t)] \quad (2.3.23)$$

where,

$$t_r(r_{ij}) = \frac{r_{ij} - r_{ij}^{LJ \min}}{r_{ij}^{LJ \max} - r_{ij}^{LJ \min}} \quad (2.3.24)$$

and

$$t_b(b_{ij}) = \frac{b_{ij} - b_{ij}^{\min}}{b_{ij}^{\max} - b_{ij}^{\min}} \quad (2.3.25)$$

The switching function C_{ij} is used to determine whether or not pairs of atoms are connected to one another through a series of covalent bonds and is given by,

$$C_{ij} = 1 - \max\{w_{ij}(r_{ij}), w_{ik}(r_{ik}) \cdot w_{kj}(r_{kj}) \forall k, w_{ik}(r_{ik}) \cdot w_{kl}(r_{kl}) \cdot w_{lj}(r_{lj}) \forall k, l\} \quad (2.3.26)$$

where the symbol \forall denotes that all possible atoms labeled k and combinations k, l must be checked for a given pair of atoms i and j . Consequently, this function requires cycling through all possible permutations of three successive bonds, to determine if atoms i and j are connected through a series of covalent bonds or partial bonds and therefore should not experience the LJ interaction. Although C_{ij} is very general and allows the potential to describe an arbitrary configuration of carbon and hydrogen atoms, this portion of the potential can require the largest computational expense on a parallel architecture. For large systems, evaluating C_{ij} requires a long iterative procedure whereby every nearest neighbor is checked for a possible path between atoms i and j . Although the C_{ij} switching function is expensive, it is nonetheless necessary. If all pairs of atoms were evaluated with V_{ij}^{LJ} alone, the 12th power repulsion would dominate at short distances nullifying the REBO potential, which would lead to an inaccurate description for the covalently bonded atoms separated by $< 2 \text{ \AA}$. The switching functions relieve this problem and alleviate the need to explicitly express which pairs of atoms experience each type of bonding, thus preserving the reactive characteristics of the REBO potential. With this approach, entire molecules separated by any distance can experience van der Waals attraction and can subsequently come into contact and react.

The last term of the AIREBO potential is an explicit dihedral term which shows preferences to specific bond angles, which is of particular importance in polymeric systems and is given by,

$$E_{kijl}^{TORS} = w_{ki}(r_{ki})w_{ij}(r_{ij})w_{jl}(r_{jl})V^{TORS}(\omega_{kijl}) \quad (2.3.27)$$

where the torsional potential is based on a 10th power cosine function,

$$V^{TORS}(\omega_{kijl}) = \frac{256}{405} \varepsilon_{kijl} \cos^{10}\left(\frac{\omega_{kijl}}{2}\right) - \frac{\varepsilon_{kijl}}{10}, \quad (2.3.28)$$

and ε_{kijl} is a constant. Using this functional form, the AIREBO potential was fit to various experimental data with strong emphasis on the thermodynamic properties of liquid polymers [83]. Since the fitting procedure for AIREBO focused on polymeric systems, we deemed it a suitable choice for the present investigation.

The covalent portion of the AIREBO potential has the same functional form as Brenner's second generation REBO potential [81], however several of the fitting parameters were slightly adjusted for better overall performance [83]. The REBO potential itself has been used to accurately predict the thermal conductivity of diamond [82]. The AIREBO potential is much more complicated than Kirkwood's model [72], because the functional form is motivated by the chemical bonding characteristics of hydrocarbons. To conduct our molecular dynamics simulations of PE chain lattices, we implemented the AIREBO potential in the Large Atomic/Molecular Massively Parallel Simulator (LAMMPS), which is a software package developed at Sandia National Laboratories [84]. This implementation required several modifications to the existing parallel MD framework LAMMPS is built upon. Most notably, we changed the way in which nearest neighbors are computed such that the AIREBO force routine includes its own secondary neighbor list function. Our implementation includes a neighboring function that scans the neighbor list generated by LAMMPS and finds all pairs of atoms separated by less than 2 Å. This secondary list is then used in conjunction with the larger neighbor list generated by LAMMPS, which is based on a user specified cut-off distance for the LJ potential. The parallel features of LAMMPS, however, were not changed. Any simulation using the AIREBO potential can run in parallel, using the domain decomposition procedure already employed in LAMMPS [84].

Chapter 3: Analysis of MD Simulation Results

In the preceding chapter we introduced the theory and methodology of MD simulations. In this chapter we describe the theoretical background associated with the analysis of MD trajectories for the study of thermal properties. Although atomic motions may appear random, there is always some degree of correlation. When viewed through a statistical lens, this correlation can be measured and used to determine the thermal conductivity. In this chapter we present several derivations of equations that are later used to analyze our MD simulations of PE chain lattices. First we discuss how the system's energy and temperature are computed in an equilibrium MD simulation. We then proceed to a discussion of the Green-Kubo method and describe how the thermal conductivity, heat flux and chain-chain conductance are computed. We then move to a brief derivation of the Boltzmann equation and we show how it can be used to calculate the thermal conductivity of a 1D chain under the relaxation time approximation. After introducing the relaxation time based approach, we then discuss lattice dynamics and the methods used for normal mode analysis. Finally we conclude the chapter with a brief overview of the simulation procedures.

3.1 Energy and Temperature

As discussed in chapter 2, an equilibrium MD simulation with periodic boundary conditions naturally conserves energy, volume and the number of particles. These conserved quantities correspond to the microcanonical statistical ensemble, where the energy in the simulation is

$$E = \Phi + \sum_{i=1}^N \frac{1}{2} \cdot m_i \cdot \bar{\mathbf{v}}_i^2 \quad (3.1.1)$$

where Φ is the system potential energy, m_i is the particle mass, $\bar{\mathbf{v}}_i$ is its velocity and the system energy E remains constant. The second term in (3.1.1) is the system's kinetic

energy, as we show it is consistent with (3.1.1) by taking the time derivative of the energy

$$\begin{aligned}\frac{dE}{dt} &= \sum_{i=1}^N \frac{\partial \Phi}{\partial \vec{r}_i} \cdot \frac{\partial \vec{r}_i}{\partial t} + \frac{1}{2} \cdot m_i \cdot \left(2 \cdot \vec{v}_i \cdot \frac{\partial \vec{v}_i}{\partial t} \right) = 0 \\ &\quad - \frac{\partial \Phi}{\partial \vec{r}_i} = m_i \cdot \left(\frac{\partial \vec{v}}{\partial t} \right)\end{aligned}\tag{3.1.2}$$

Thus, $\frac{1}{2} \cdot m \cdot \vec{v}^2$ conserves the total energy when calculating the forces as $-\frac{\partial \Phi}{\partial \vec{r}_i}$. With

this definition for energy, we can now describe the system temperature.

To determine the temperature of a system of particles we must relate their positions and momenta to the macroscopic variables we observe. Intuitively we know that for the same macroscopic state, described by its temperature, pressure, volume, etc. we have a large number of corresponding microscopic states. If we imagine a set of six orthogonal axes, three for position and three for momentum, we could plot the individual state of one particle within the system. If we then multiply the number of axes by the number of particles N , we generate $6N$ total dimensions and could identify the system's microscopic state as a single point in phase space. As time evolves, under the constraints of the system Hamiltonian, H , the microstate moves through phase space tracing out a trajectory. We can then imagine using phase space to plot a number of independent systems, s , all of which have the same macroscopic state identified by temperature T , volume V and pressure P . If we then take s to be large enough, such that it approaches a continuum of points we can write a conservation equation for the s systems in terms of a spatially and temporally dependent density of systems:

$$\frac{df}{dt} = \frac{\partial f^{(s)}}{\partial t} + \frac{\partial f^{(s)}}{\partial \vec{q}_s} \cdot \frac{\partial \vec{q}_s}{\partial t} + \frac{\partial f^{(s)}}{\partial \vec{p}_s} \cdot \frac{\partial \vec{p}_s}{\partial t} = 0\tag{3.1.3}$$

where $f^{(s)}$ is the density of s points, \vec{q}_s and \vec{p}_s are the position and momentum of all the particles and t is time [24, 85]. Equation (3.1.3) is called the Liouville equation and will be subsequently used to derive an expression for thermal conductivity in section 3.2, based on linear response theory, and it will also be used to derive the Boltzmann equation in section 3.3.

As time evolves, each individual system translates through phase space tracing out a trajectory. If each system is microcanonical, the total energy remains constant and we can define a hyper-surface containing all the system states that correspond to that fixed amount of energy. The total area of the constant energy hyper-surface could then be used as an approximate measure of the number of states Ω available to the system, where all states are treated as equally likely. Using this estimate for the number of states we can approximate the system entropy using the Boltzmann relation

$$S = k_B \cdot \ln(\Omega) \quad (3.1.4)$$

where S is the entropy, k_B is Boltzmann's constant and Ω is the number of available microstates that correspond to the same macrostate. The temperature of the system can then be determined by the thermodynamic definition

$$\frac{1}{T} = \left. \frac{\partial S}{\partial E} \right|_{N,V} \quad (3.1.5)$$

where T is temperature, E is the system's energy, while the number of particles N and volume V remain fixed.

Let us now consider a classical three dimensional system of harmonic oscillators.

We can write the system Hamiltonian H as the sum of potential $\frac{1}{2} m_i \cdot \omega^2 \cdot \bar{\mathbf{q}}_i^2$ and kinetic energies $\frac{\bar{\mathbf{p}}_i^2}{2m_i}$ for each particle,

$$E = H\{\bar{\mathbf{q}}_1 \dots \bar{\mathbf{q}}_N, \bar{\mathbf{p}}_1 \dots \bar{\mathbf{p}}_N\} = \sum_{i=1}^N \left(\frac{\bar{\mathbf{p}}_i^2}{2m_i} + \frac{1}{2} m_i \cdot \omega^2 \cdot \bar{\mathbf{q}}_i^2 \right) \quad (3.1.6)$$

where $\bar{\mathbf{p}}_i$ is the particle momentum, $\bar{\mathbf{q}}_i$ is the displacement, m is the mass, and ω is the natural frequency, which is related to the spring constant $K = m_i \cdot \omega^2$.

The estimate for the number of states can then be calculated by integrating over the coordinate space subject to the constraint that the energy be constant:

$$\Omega = \frac{1}{h^{3N}} \cdot \int_{\bar{H}=E}^{\infty} d\bar{\mathbf{q}}_1 \dots d\bar{\mathbf{q}}_N \cdot d\bar{\mathbf{p}}_1 \dots d\bar{\mathbf{p}}_N \quad (3.1.7)$$

where $\hbar = h/2\pi$, h is Planck's constant and \hbar is used to non-dimensionalize the integral. For mathematical convenience we can make a canonical transformation that preserves phase space

$$\bar{q}_i' \equiv \sqrt{m_i \cdot \omega} \cdot \bar{q}_i \quad \bar{p}_i' \equiv \frac{\bar{p}_i}{\sqrt{m_i \cdot \omega}}$$

where the energy is now

$$E = \frac{\omega}{2} \sum_{i=1}^N (\bar{p}_i'^2 + \bar{q}_i'^2) \quad (3.1.8)$$

The hyper-sphere radius can then be determined from,

$$R = \sqrt{\frac{2E}{\omega}} \quad (3.1.9)$$

and the integration for the number of states is now written with respect to \bar{q}_i' and \bar{p}_i' ,

$$\Omega = \frac{1}{\hbar^{3N}} \cdot \int_{H=E}^{\infty} d\bar{q}'_1 \dots d\bar{q}'_N \cdot d\bar{p}'_1 \dots d\bar{p}'_N \cdot \quad (3.1.10)$$

Here we have relaxed the constant energy criterion to encompass energies close to E . We now approximate the integral with that of a thin volumetric shell, where

$$\Omega \approx \frac{2\pi^{3N}}{(3N-1)!} \cdot \left(\frac{2E}{\hbar\omega}\right)^{3N} \cdot \Delta R. \quad (3.1.11)$$

Inserting (3.1.11) into (3.1.4) yields an extensive expression for the entropy that can be differentiated to yield an approximate expression for the energy in terms of the temperature.

$$\frac{\partial S}{\partial E} = \frac{1}{T} \approx k_B \cdot \left(\frac{3N}{E}\right) \quad (3.1.12)$$

where,

$$E \approx N \cdot k_B \cdot T \quad (3.1.13)$$

With this result we can derive an expression for a single particle probability distribution as a function of its coordinates by integrating over all other coordinates in the system,

$$f(\bar{\mathbf{q}}_1, \bar{\mathbf{p}}_1) = \frac{\frac{1}{\hbar^{3N-1}} \cdot \int_{\bar{H} \leq E(N-1)} d\bar{\mathbf{q}}_2 \dots d\bar{\mathbf{q}}_N \cdot d\bar{\mathbf{p}}_2 \dots d\bar{\mathbf{p}}_N}{\frac{1}{\hbar^{3N}} \cdot \int_{\bar{H} \leq E(N)} d\bar{\mathbf{q}}_1 \dots d\bar{\mathbf{q}}_N \cdot d\bar{\mathbf{p}}_1 \dots d\bar{\mathbf{p}}_N} \quad (3.1.14)$$

where $E(N-1)$ denotes the energy of all but one particle in the system. Substituting (3.1.11) into (3.1.14) reduces to,

$$f(\bar{\mathbf{q}}_1, \bar{\mathbf{p}}_1) = \frac{\omega}{2\pi} \cdot \frac{N}{E} \cdot \left(1 - \frac{\frac{\bar{\mathbf{p}}_1^2}{2 \cdot m_1} + \frac{1}{2} m_1 \cdot \omega^2 \cdot \bar{\mathbf{q}}^2}{E} \right) \quad (3.1.15)$$

because N is large and a single particle only contributes a small portion of the total system energy. This allows us to treat (3.1.15) as the first term of an exponential series, resulting in a properly normalized Gaussian distribution.

$$f(\bar{\mathbf{q}}_1, \bar{\mathbf{p}}_1) = \frac{\omega}{2\pi \cdot k_B \cdot T} \exp \left(\frac{-\left(\frac{\bar{\mathbf{p}}_1^2}{2 \cdot m_1}\right) - \left(\frac{1}{2} m_1 \cdot \omega^2 \cdot \bar{\mathbf{q}}^2\right)}{E} \right) \quad (3.1.16)$$

Using the one particle distribution function we can calculate the average kinetic and potential energies

$$\left\langle \frac{\bar{\mathbf{p}}_1^2}{2 \cdot m_1} \right\rangle = \frac{3}{2} k_B \cdot T \quad \left\langle \frac{1}{2} m_1 \cdot \omega^2 \cdot \bar{\mathbf{q}}^2 \right\rangle = \frac{3}{2} k_B \cdot T \quad (3.1.17)$$

This result is commonly known as the equipartition theorem, because each quadratic term in the energy contributes $\frac{3}{2} k_B \cdot T$ to the total energy.

In modeling atomic interactions in real materials, the potential energies are typically large and negative as compared to the smaller positive kinetic energy contributions. This has led to interesting questions concerning the appropriate definition of temperature in a MD simulation. One argument used to justify the use of (3.1.17) to calculate temperature is based on the fact that the atoms in crystalline materials vibrate around an equilibrium position, similar to a particle in a harmonic potential well.

Although the potential energy in most real systems is large and negative, such that it heavily outweighs the kinetic energy contribution below the melting/dissociation temperature, the potential energy could be adjusted with use of an additive constant. This constant could be adjusted to cancel the equilibrium lattice energy but the constant would not alter the system dynamics. If the constant is chosen appropriately, we could perturb the atoms as in a classical MD simulation and we will likely observe an equipartition of kinetic and potential energy. If the assumption of equipartition is valid for the system of interest, the temperature can be computed as [75],

$$T = \frac{1}{3N} \cdot \left\langle \frac{1}{2} m \cdot \bar{\mathbf{v}}^2 \right\rangle, \quad (3.1.18)$$

where the brackets $\langle _ \rangle$ denote a time average.

Some systems may not be well approximated by the equipartition theorem, because in MD simulations all vibrational modes are activated at all temperatures. In real materials, however, the vibrational modes obey quantum mechanics which result in Bose-Einstein statistics [21, 24]. Under this quantum model for the vibrational energy, lower frequency modes are excited to higher energy states at lower temperatures, while the higher frequency modes can remain in the ground state. For systems where the spread in vibrational frequencies is minimal this effect is less pronounced, particularly at higher temperatures where the highest frequency modes are excited well above the ground state. Some systems, such as polyethylene chains, however, have vibrational frequencies that span almost three orders of magnitude [86]. For these systems, even at moderate and high temperatures, the highest frequency modes may not be highly excited. In a MD simulation, which is inherently based on classical mechanics, however, these modes would be more highly excited and would comprise a greater portion of the system's vibrational energy. Based on this line of reasoning we can attempt to fuse the classical dynamics of MD simulations with the quantum reality, by choosing a different definition for the system temperature. Here we propose defining the temperature in the MD simulation by matching the vibrational energy in the simulation with the total vibrational energy for a system of phonons at the same temperature,

$$E_{MD} = \sum_p \sum_{\mathbf{k}} \frac{\hbar \omega}{e^{\hbar \omega / k_B T} - 1} \quad (3.1.19)$$

where k_B is Boltzmann's constant. Lukes *et al.* [9] have used a similar definition to rescale their temperature-dependent MD results, which were initially run using the more common equipartition-based definition (3.1.18). The main difference between Eq. (3.1.19) and the definition used by others [9, 87], is that here we have not included the zero point energy [21]. Eq. (3.1.19) essentially states that the total vibrational excitation energy in the MD system should match that of a quantum system of phonons at the desired temperature. This definition requires a prerequisite determination of the phonon dispersion. Once the phonon states for a specific material are known, the total energy for the MD system can be determined and used as a set point for initialization of the system dynamics.

3.2 Green-Kubo Formula for the Thermal Conductivity

To determine thermal conductivity from equilibrium MD trajectories, we use the approach developed by Green and Kubo [24, 74] based on the linearized Liouville equation. We begin by solving the linearized Liouville equation for the N particle distribution function. We then use this distribution to determine the average heat flux in a system that is subjected to a thermal disturbance as a temperature perturbation. Lastly we identify the portion of the result that is proportional to the temperature gradient as the thermal conductivity.

To begin, we recast (3.1.3) in terms of N particles recognizing that the second and third terms can be substituted in terms of the Hamiltonian equations of motion [24],

$$\frac{\partial f^{(N)}}{\partial t} = \{H, f^{(N)}\} \quad (3.2.1)$$

where $f^{(N)}$ is the N particle distribution and the Poisson bracket $\{_, _\}$ is defined as

$$\{A, B\} \equiv \sum_{i=1}^N \left(\frac{\partial A}{\partial \mathbf{q}_i} \cdot \frac{\partial B}{\partial \mathbf{p}_i} - \frac{\partial A}{\partial \mathbf{p}_i} \cdot \frac{\partial B}{\partial \mathbf{q}_i} \right) \quad (3.2.2)$$

with A and B as arbitrary functions of the phase space variables. We then define the Liouville operator Γ as

$$\Gamma \equiv i \cdot \{H, _ \}$$

so that

$$\frac{\partial f^{(N)}}{\partial t} = -i \cdot \Gamma f^{(N)} \quad (3.2.3)$$

where $i = \sqrt{-1}$. The fundamental assumption in linear response theory is that the Liouville operator does not have an explicit time dependence. Assuming this is valid, we can solve the Liouville equation for the time and phase space dependent density

$$f^{(N)}(\vec{q}, \vec{p}, t) = \exp(-i \cdot t \cdot \Gamma) f^{(N)}(\vec{q}, \vec{p}, 0) \quad (3.2.4)$$

With this solution we derive an expression for the thermal conductivity by considering the linear response to a thermal disturbance.

We momentarily step away from the microcanonical description of our system and consider a canonical system at equilibrium temperature T with a small temperature disturbance δT . Assuming that δT is stationary, its gradient is constant and that the system is in local equilibrium we can apply Boltzmann statistics and write the local probability distribution as:

$$f_0 = C \cdot \exp\left(-\frac{\varepsilon \cdot \Delta V}{k_B \cdot (T + \delta T)}\right) \approx C \cdot \exp\left(-\frac{\varepsilon \cdot \Delta V}{k_B \cdot T} \cdot \left(1 - \frac{\delta T}{T}\right)\right) \quad (3.2.5)$$

where ε is the local energy density and ΔV is the local volume. Taking the second term in the exponent as the perturbation energy we write the perturbed Hamiltonian H' as

$$H'(t) = -\int \varepsilon(\vec{q}(t)) \frac{\delta T(\vec{q}(t))}{T} dV \quad H = H_0 + H' \quad (3.2.6)$$

where H is the total energy and H_0 is the energy of the unperturbed system. Having now identified the perturbed system's Hamiltonian we rewrite the Liouville equation as,

$$\frac{\partial f^{(N)}}{\partial t} = \{H_0, f^{(N)}\} + \{H', f_0^{(N)}\} \quad (3.2.7)$$

By substituting (3.2.6) into the second expression, we arrive at

$$\frac{\partial f^{(N)}}{\partial t} = -i \cdot \Gamma_0 f^{(N)} - \left(\frac{f_0^{(N)}}{k_B \cdot T^2}\right) \cdot \int \frac{\partial \varepsilon(\vec{q}(t))}{\partial t} \cdot \delta T(\vec{q}(t)) dV. \quad (3.2.8)$$

Using energy conservation

$$\frac{\partial \varepsilon}{\partial t} + \vec{\nabla} \cdot \vec{\mathbf{j}}_Q = 0 \quad (3.2.9)$$

where ε is the local energy and $\vec{\mathbf{j}}_Q$ is the local heat flux, we then substitute into (3.2.8)

$$\frac{\partial f^{(N)}}{\partial t} = -i \cdot \Gamma_0 f^{(N)} - \left(\frac{f_0^{(N)}}{k_B \cdot T^2} \right) \cdot \int \left[-\vec{\nabla} \cdot (\vec{\mathbf{j}}_Q(\vec{\mathbf{q}}(t)) \cdot \delta T(\vec{\mathbf{q}}(t))) + (\vec{\mathbf{j}}_Q(\vec{\mathbf{q}}(t)) \cdot \vec{\nabla} \cdot \delta T(\vec{\mathbf{q}}(t))) \right] dV. \quad (3.2.10)$$

The first term in the integral is negligible, which allows us to focus on integrating the second term, resulting in

$$\frac{\partial f^{(N)}}{\partial t} = -i \cdot \Gamma_0 f^{(N)} - \left(\frac{f_0^{(N)} \cdot V}{k_B \cdot T^2} \right) \cdot \vec{\nabla} \cdot \delta T \cdot \vec{\mathbf{J}}_Q \quad (3.2.11)$$

where $\vec{\mathbf{J}}_Q$ is now the net heat flux in the system. We argue that the first term inside the integral of (3.2.10) is small assuming $\vec{\mathbf{j}}_Q(\vec{\mathbf{q}}(t))$ and the disturbance $\delta T(\vec{\mathbf{q}}(t))$ itself are independent, resulting in a smaller volumetric integral by comparison to the second term. However, we intuitively know from Fourier's law for heat conduction (2.1.7) that the heat flux $\vec{\mathbf{j}}_Q(\vec{\mathbf{q}}(t))$ and the gradient of the disturbance $\delta T(\vec{\mathbf{q}}(t))$ (temperature gradient) are more likely to point in the same direction, giving rise to a larger volumetric integral.

Based on this simplification, we can continue by solving (3.2.11) for the phase space density

$$f^{(N)}(\vec{\mathbf{q}}, \vec{\mathbf{p}}, t) = \frac{-V}{k_B \cdot T^2} \cdot \vec{\nabla} \cdot \delta T \cdot \int_{-\infty}^t \exp(-i \cdot (t-t') \cdot \Gamma_0) \vec{\mathbf{J}}_Q dt' \quad (3.2.12)$$

and use the result to calculate the ensemble averaged heat flux

$$\langle \vec{\mathbf{J}}_Q(t) \rangle = \iint \vec{\mathbf{J}}_Q(\vec{\mathbf{q}}, \vec{\mathbf{p}}, t) \cdot f^{(N)}(\vec{\mathbf{q}}, \vec{\mathbf{p}}, t) d\vec{\mathbf{q}} d\vec{\mathbf{p}}. \quad (3.2.13)$$

By substituting (3.2.12), we arrive at

$$\langle \vec{\mathbf{J}}_Q(t) \rangle = \frac{-V}{k_B \cdot T^2} \int_{-\infty}^t \langle J_{Qx}(t) \cdot \vec{\mathbf{J}}_Q(t-t') \rangle \cdot \vec{\nabla} \cdot \delta T \cdot dt. \quad (3.2.14)$$

We then extract the temperature gradient, since we assumed it to be time independent, resulting in an expression for the heat flux, similar to Fourier's law (2.1.7). We now identify an expression for the thermal conductivity, using a Fourier transform to rewrite the integral to obtain:

$$\kappa_{ij}(T, \omega) = \frac{V}{k_B \cdot T^2} \int_0^\infty \langle J_{Qi}(0) \cdot J_{Qj}(\tau) \rangle \cdot \exp(-i\omega \cdot \tau) \cdot d\tau, \quad (3.2.14)$$

Here, $\kappa_{ij}(T, \omega)$ is the temperature and frequency dependent thermal conductivity tensor, where ω is the perturbation frequency and the ij subscripts denote the directional components. In macroscopic heat conduction, we most often encounter constant fluxes and therefore require the zero frequency limit of (3.2.14) [24, 74],

$$\kappa_{ij}(T) = \frac{V}{k_B \cdot T^2} \int_0^\infty \langle \bar{\mathbf{J}}_{Qi}(0) \cdot \bar{\mathbf{J}}_{Qj}(\tau) \rangle \cdot d\tau \quad (3.2.15)$$

where $\kappa(T)$ is now the thermal conductivity most often required in macroscopic analysis, and where the time scale of the system perturbations are orders of magnitude slower than atomic scale fluctuations. However for high frequency inputs of similar time scales as the atomic fluctuations, the frequency dependent thermal conductivity can deviate from the static value by orders of magnitude [88].

We are now left with the task of determining the volume integrated heat flux for the system in terms of the microscopic variables we can extract from an MD simulation. To do this, we revert back to (3.2.9) and develop a quantum mechanical heat flux operator that is generalized for any phase of matter and can be applied to any empirical form of potential energy. Here we recast (3.2.9) as [89],

$$\dot{\mathbf{H}}(\mathbf{x}) + \vec{\nabla} \cdot \mathbf{s}(\mathbf{x}) = 0 \quad (3.2.16)$$

where $\mathbf{s}(\mathbf{x})$ is now a local heat flux operator and $\dot{\mathbf{H}}(\mathbf{x})$ is related to the energy density operator and \mathbf{H} by [89],

$$\dot{\mathbf{H}}(\mathbf{x}) = \frac{1}{i \cdot \hbar} \{ \mathbf{H}(\mathbf{x}), \mathbf{H} \} \quad (3.2.17)$$

where $i = \sqrt{-1}$ in the forthcoming steps when not used as a labeling subscript and \hbar is Planck's constant h divided by 2π . Combining these expressions gives [89],

$$\vec{\nabla} \mathbf{s}(\mathbf{x}) = \frac{i}{\hbar} \{ \mathbf{H}(\mathbf{x}), \mathbf{H} \} \quad (3.2.18)$$

We then assume a generic form for the Hamiltonian operator in order to express the heat flux operator in terms of the microscopic variables available in a MD simulation,

$$H = \sum_{i=1}^N \left(\frac{\bar{\mathbf{p}}_i^2}{2 \cdot m_i} + \Phi_i \right) \quad (3.2.19)$$

We then define a local energy density operator in terms of a spatially dependent weighting function that incorporates contributions to the heat flux from the local environment [89].

$$H(\mathbf{x}) = \frac{1}{2} \sum_{i=1}^N \left\{ \Delta(\mathbf{x} - \bar{\mathbf{q}}_i) \left(\frac{\bar{\mathbf{p}}_i^2}{2 \cdot m_i} + \Phi_i \right) + H.c. \right\} \quad (3.2.20)$$

where $H.c.$ is the Hermitian conjugate and $\Delta(\mathbf{x} - \bar{\mathbf{q}}_i)$ is a spatial weighting function normalized to unity

$$\int \Delta(\mathbf{x} - \bar{\mathbf{q}}_i) dV = 1. \quad (3.2.21)$$

Taking

$$\Delta(\mathbf{x} - \bar{\mathbf{q}}_i) = \left(\frac{1}{l \cdot \sqrt{\pi}} \right)^3 \cdot \exp \left(- \left(\frac{|\mathbf{x} - \bar{\mathbf{q}}_i|}{l} \right)^2 \right), \quad (3.2.22)$$

and using the commutation relations for the position and momentum operators, along with a Taylor expansion of the spatial weighting function, allows simplification of (3.2.18) to

$$\frac{i}{\hbar} \{H(\mathbf{x}), H\} = \sum_{\alpha} \frac{\partial \mathbf{s}_{\alpha}}{\partial \mathbf{x}_{\alpha}}. \quad (3.2.23)$$

Here α denotes a vector component and the spatially dependent heat flux is given by

$$\begin{aligned} \mathbf{s}(\mathbf{x}) = & \frac{1}{2V} \left[\sum_{i=1}^N \left(\Delta(\mathbf{x} - \bar{\mathbf{q}}_i) \frac{\mathbf{p}_i}{2m_i} + \frac{\mathbf{p}_i}{2m_i} \Delta(\mathbf{x} - \bar{\mathbf{q}}_i) \right) \left(\frac{\bar{\mathbf{p}}_i^2}{2 \cdot m_i} + \Phi_i \right) + \dots \right. \\ & \left. \sum_{ij}^N \left(\left(1 + \frac{1}{2!} \sum_b (\mathbf{q}_i^b - \mathbf{q}_j^b) \frac{\partial}{\partial \mathbf{x}^b} + \dots \right) \Delta(\mathbf{x} - \bar{\mathbf{q}}_i) \right) \cdot (\bar{\mathbf{q}}_i - \bar{\mathbf{q}}_j) \cdot \frac{1}{i\hbar} \left\{ \frac{\bar{\mathbf{p}}_i^2}{2 \cdot m_i}, \Phi_i \right\} \right] + H.c. \end{aligned} \quad (3.2.24)$$

We now spatially average the local heat flux operator $\mathbf{s}(\mathbf{x})$, to yield an expression suitable for implementation in a MD simulation [89],

$$\mathbf{s} = \frac{1}{V} \sum_{i=1}^N \left[\left(\frac{\bar{\mathbf{p}}_i^2}{2 \cdot m_i} + \Phi_i \right) \cdot \frac{\bar{\mathbf{p}}_i}{m_i} + \sum_{\substack{j=1 \\ j \neq i}}^N \left(\frac{\partial \Phi_j}{\partial \bar{\mathbf{q}}_i} \cdot \frac{\bar{\mathbf{p}}_i}{m_i} \right) \cdot (\bar{\mathbf{q}}_i - \bar{\mathbf{q}}_j) \right]. \quad (3.2.25)$$

This expression (3.2.25) has two physically meaningful terms that correspond to the two mechanisms that carry heat in all phases of matter. The first term, often called the convective or diffusion term, dominates in liquids and gases where energy is transported through the kinetic energy of the constituent molecules. In solids the second term dominates because the forces are large and atoms do not diffuse through the crystal.

In addition to using this approach for describing the thermal conductivity, the Green-Kubo approach has also been used to derive expressions for other linear response transport coefficients, such as the electrical conductivity, mass diffusivity and viscosity [24, 74, 90]. In each case the resulting transport coefficient is shown to be proportional to the integral of the autocorrelation function for the corresponding flux. As a result, this approach can be generalized to describe any linear transport coefficient. Domingues *et al.* [91] have used this more general technique to derive an expression for the thermal conductance between any two arbitrary bodies. This derivation is based on an analogy between a voltage/temperature gradient, which drives the flow of electrons/heat through an electrical/thermal impedance [90]. We first define the linear response susceptibility $G_{12}^*(\omega)T_0$, which relates the heat flux Q_{12} to the temperature difference [91],

$$\Delta T(\omega) = \frac{Q_{12}(\omega)}{G_{12}^*(\omega)T_0} \quad (3.2.26)$$

where T_0 is the average temperature between the two bodies. The equilibrium fluctuations in $\Delta T(\omega)$ and $Q_{12}(\omega)$ are characterized by their respective power spectral densities $P_{\Delta T}(\omega)$ and $P_{Q_{12}}(\omega)$ which are proportional to the square of $\Delta T(\omega)$ and $Q_{12}(\omega)$,

$$P_{\Delta T}(\omega) = \frac{P_{Q_{12}}(\omega)}{|G_{12}^*T_0|^2} \quad (3.2.27)$$

We can then draw an analogy to the relationship between electrical current and voltage [90],

$$\Delta V(\omega) = I \cdot Z(\omega) \quad (3.2.28)$$

where the resistance is the real part of the complex impedance

$$R(\omega) = \text{Re}(Z(\omega)) \quad (3.2.29)$$

$$R(\omega) = \text{Re} \left(\frac{1}{G_{12}^*(\omega) T_0} \right). \quad (3.2.30)$$

Application of the fluctuation-dissipation theorem then allows us to write the average square voltage as [90],

$$\langle V^2 \rangle = \frac{2}{\pi} \int_0^{\infty} R(\omega) \cdot \Theta(\omega, T) d\omega \quad (3.2.31)$$

where Θ is the average energy of a quantum harmonic oscillator,

$$\Theta = \frac{\hbar\omega}{\exp(\hbar\omega/k_B T) - 1}. \quad (3.2.32)$$

By analogy we can also write a similar expression for the temperature fluctuations,

$$\langle \delta\Delta T(0) \cdot \delta\Delta T(t) \rangle = \frac{2}{\pi} \int_0^{\infty} R(\omega) \cdot \Theta(\omega, T) d\omega \quad (3.2.33)$$

$$\langle \delta\Delta T(0) \cdot \delta\Delta T(\omega) \rangle = \text{Re} \left(\frac{1}{G_{12}^*(\omega) T_0} \right) \cdot \Theta(\omega, T). \quad (3.2.34)$$

Rewriting the resistance as,

$$\text{Re} \left(\frac{1}{G_{12}^*(\omega) T_0} \right) = \frac{\text{Re}(G_{12}^*(\omega))}{|G_{12}^*(\omega)|^2 T_0} \quad (3.2.35)$$

yields a second expression for the power spectral density of $P_{\Delta T}(\omega)$

$$P_{\Delta T}(\omega) = \frac{\text{Re}(G_{12}^*(\omega))}{|G_{12}^*(\omega)|^2} \cdot \Theta(\omega, T) \quad (3.2.36)$$

Equating (3.2.27) and (3.2.36) results in an expression for the real part of the susceptibility [91],

$$\text{Re}(G_{12}^*(\omega)) = \frac{P_{Q_{12}}(\omega)}{\Theta(\omega, T) \cdot T_0^2}. \quad (3.2.37)$$

Inspection of (3.2.26) identifies the thermal conductance $G = \frac{Q_{12}}{\Delta T}$ as,

$$G = T_0 \cdot G_{12}^* \quad (3.2.38)$$

where the power spectral density for the energy exchanged between the two bodies can be written as,

$$P_{Q_{12}}(\omega) = \int_{-\infty}^{\infty} \langle Q_{12}(0) \cdot Q_{12}(t) \rangle e^{-i\omega t} dt \quad (3.2.39)$$

based on the Wiener-Khinchin theorem. This results in the following expression for the thermal conductance [91],

$$G(\omega) = (\hbar\omega \cdot T_0)^{-1} \cdot \left(\exp\left(\frac{\hbar\omega}{k_B T}\right) - 1 \right) \cdot \int_{-\infty}^{\infty} \langle Q_{12}(0) \cdot Q_{12}(t) \rangle e^{-i\omega t} dt \quad (3.2.40)$$

where again we are principally interested in the static conductance as $\omega \rightarrow 0$. The conductance can then be calculated in a MD simulation by tracking the equilibrium fluctuations in the energy exchanged between the two bodies [91] as,

$$Q_{12} = \sum_{\substack{j \in \text{body1} \\ j \in \text{body2}}} \mathbf{F}_{ij} \cdot \mathbf{v}_j - \sum_{\substack{j \in \text{body1} \\ j \in \text{body2}}} \mathbf{F}_{ji} \cdot \mathbf{v}_i \quad (3.2.41)$$

where \mathbf{F}_{ij} is the force exerted on atom j by atom i , while atom j travels with velocity \mathbf{v}_j and \mathbf{F}_{ji} is the force exerted by atom j on atom i , which travels with velocity \mathbf{v}_i .

Equation (3.2.40) is a particularly useful result and has far reaching implications as a new way to investigate the effects of the thermal contact resistance. Most notably, this approach offers an alternative to the more widely used non-equilibrium techniques, which have limited ability to elucidate the details of thermal transport. This approach, however, is based on the equilibrium fluctuations in the net energy exchanged between the two bodies. This allows for natural incorporation of the modal analysis techniques discussed in the forthcoming sections of this chapter, which could allow for the determination of the phonon reflectivity at material interfaces. This expression for the thermal conductance is also useful for the present investigation, because it will allow for calculation of the thermal conductance between PE chains, which is expected to increase with the number and strength of the van der Waals interactions.

3.3 The Boltzmann Equation for Phonon Transport

We begin this section by first deriving the Boltzmann equation for gas molecules. We then derive an expression for the thermal conductivity based on phonon transport.

The resulting expression allows us to calculate the individual phonon contributions to the thermal conductivity, which can provide insight into the thermal transport mechanisms.

We start by recasting the Liouville equation, (3.1.3), considering a system of particles that are broken into two regions. A joint system Hamiltonian H is then composed of two regional Hamiltonians H_s and H_{N-s} as well as an interaction Hamiltonian H' as follows,

$$H = H_s + H_{N-s} + H' \quad (3.3.1)$$

where the subscript N denotes the total number of particles and s denotes the subset of particles we are interested in describing, which interact with particles not contained in the group $N - s$. We assume that the Hamiltonian has the following form

$$\begin{aligned} H_s &= \sum_{n=1}^s \left[\left(\frac{\bar{\mathbf{p}}_n^2}{2m} \right) + U(\bar{\mathbf{q}}_n) + \frac{1}{2} \cdot \sum_{\substack{m=1 \\ m \neq n}}^s \Phi(\bar{\mathbf{q}}_n - \bar{\mathbf{q}}_m) \right] \\ H_{N-s} &= \sum_{i=s+1}^N \left[\left(\frac{\bar{\mathbf{p}}_i^2}{2m} \right) + U(\bar{\mathbf{q}}_i) + \frac{1}{2} \cdot \sum_{\substack{j=s+1 \\ j \neq i}}^N \Phi(\bar{\mathbf{q}}_i - \bar{\mathbf{q}}_j) \right] \end{aligned} \quad (3.3.2)$$

which includes an external potential $U(\bar{\mathbf{q}})$ and a particle interaction potential Φ . The interaction Hamiltonian H' is then

$$H' = \sum_{n=1}^s \sum_{i=s+1}^N \Phi(\bar{\mathbf{q}}_n - \bar{\mathbf{q}}_i). \quad (3.3.3)$$

Next we rewrite the phase space density in terms of a normalized probability distribution function ρ_s based on the coordinates in the group of particles denoted by s ,

$$f_s(\bar{\mathbf{q}}_1, \dots, \bar{\mathbf{p}}_s, t) = \frac{N!}{(N-s)!} \int \prod_{i=s+1}^N dV_i \rho(\bar{\mathbf{q}}, \bar{\mathbf{p}}, t) = \frac{N!}{(N-s)!} \rho_s(\bar{\mathbf{q}}_1, \dots, \bar{\mathbf{p}}_s, t). \quad (3.3.4)$$

The time evolution of the probability distribution is then

$$\frac{\partial \rho_s}{\partial t} = \int \prod_{i=s+1}^N dV_i \frac{\partial \rho}{\partial t} = \int \prod_{i=s+1}^N dV_i \{ \rho, H_s + H_{N-s} + H' \}, \quad (3.3.5)$$

which involves three separate terms in the Poisson bracket, which are evaluated separately. Using integration by parts, the second term $\{ \rho, H_{N-s} \}$ goes to zero and the first and last term are written as

$$\int \prod_{i=s+1}^N dV_i \{\rho, H_s\} = \left\{ \int \prod_{i=s+1}^N dV_i \rho, H_s \right\} = \{\rho_s, H_s\} \quad (3.3.6)$$

and

$$\int \prod_{i=s+1}^N dV_i \left[\sum_{n=1}^s \frac{\partial \rho}{\partial \bar{\mathbf{p}}_n} \cdot \sum_{j=s+1}^N \frac{\partial \Phi(\bar{\mathbf{q}}_n - \bar{\mathbf{q}}_j)}{\partial \bar{\mathbf{q}}_n} + \sum_{j=s+1}^N \frac{\partial \rho}{\partial \bar{\mathbf{p}}_n} \cdot \sum_{n=1}^s \frac{\partial \Phi(\bar{\mathbf{q}}_j - \bar{\mathbf{q}}_n)}{\partial \bar{\mathbf{q}}_j} \right]. \quad (3.3.7)$$

The integral in (3.3.6) involves the sum of $N - s$ versions of the same integral and can be simplified to the following in terms of the phase space densities⁵¹

$$\frac{\partial f_s}{\partial t} + \{H_s, f_s\} = \sum_{n=1}^s \int dV_{s+1} \frac{\partial \Phi(\bar{\mathbf{q}}_n - \bar{\mathbf{q}}_{s+1})}{\partial \bar{\mathbf{q}}_n} \cdot \frac{\partial f_{s+1}}{\partial \bar{\mathbf{p}}_n} \quad (3.3.8)$$

When written in the limit that s goes to unity, (3.3.8) is termed the Boltzmann equation, which describes the time evolution of the single particle phase space density/probability distribution. In the absence of interactions the equation reduces to the left hand side of (3.3.8), often referred to as the streaming terms, because the phase space density evolution becomes identical to that of an incompressible fluid. The right hand side of (3.3.8) is called the collision term and governs the rate at which particle interactions take place.

In (3.3.8) we see that the f_s distribution depends on the integration of the f_{s+1} distribution, which comprises the probability of the coupled system of particles. To make the solution of (3.3.8) tractable, Boltzmann asserted that in the dilute gas limit, the particle trajectories are uncorrelated before collisions. Boltzmann referred to this assumption as “Stosszahlansatz”, which is more commonly known as the molecular chaos assumption [92]. With this assumption, the coupled distribution f_{s+1} in (3.3.8) can be written as a product of single particle distributions f_1 and f_2 . One subtlety associated with this assumption is that the particle trajectories are only required to be uncorrelated before collisions. After a collision, however, this assumption allows for particle trajectories to remain correlated. This asymmetry in the assumption sets the direction of time, because the particle collisions are now irreversible processes. This inherent irreversibility later became an important aspect of Boltzmann’s H-theorem, which shows that the entropy of a gas mixture evolved toward a maximum at thermal equilibrium [92].

We now change our interpretation of the Boltzmann equation from that of gas molecules to phonons, and we seek an approximation for the collision integral. Here we adopt the relaxation time approximation, whereby we model the collision integral as follows²⁰

$$\left(\frac{\partial f}{\partial t}\right)_c = -\frac{f - f_0(E, T)}{\tau(\vec{q}, \vec{k})} \quad (3.3.9)$$

where $\left(\frac{\partial f}{\partial t}\right)_c$ is the right hand side of (3.3.8), f_0 is the equilibrium distribution and $\tau(\vec{q}, \vec{k})$ is the relaxation time. The relaxation time approximation assumes that, when the system is perturbed, it decays exponentially back to the equilibrium distribution, seen by solving (3.3.10):

$$f - f_0 = C \exp\left(-\frac{t}{\tau}\right) \quad (3.3.10)$$

Recasting the Boltzmann equation within the relaxation time approximation, it is now possible to solve the phonon Boltzmann equation and derive an expression for the thermal conductivity

$$\frac{\partial f}{\partial t} + \vec{v} \cdot \vec{\nabla}_{\vec{q}} f + \frac{\vec{F}}{m} \cdot \vec{\nabla}_{\vec{v}} f = -\frac{f - f_0(E, T)}{\tau(\vec{q}, \vec{k})}, \quad (3.3.11)$$

where (3.3.12) represents a generalized expression for particle transport, in which \vec{v} is the particle velocity and $\frac{\vec{F}}{m}$ is its acceleration, and the symbols $\vec{\nabla}_{\vec{q}}$ and $\vec{\nabla}_{\vec{v}}$ denote gradients with respect to position and velocity, respectively. Next we write (3.3.12) in terms of the deviation from equilibrium statistics, where $g = f - f_0$ and

$$\frac{\partial g}{\partial t} + \frac{\partial f_0}{\partial t} + \vec{v} \cdot \vec{\nabla}_{\vec{q}} g + \vec{v} \cdot \vec{\nabla}_{\vec{q}} f_0 + \frac{F}{m} \cdot \vec{\nabla}_{\vec{v}} f_0 + \frac{F}{m} \cdot \vec{\nabla}_{\vec{v}} g = -\frac{g}{\tau} \quad (3.3.12)$$

in which

$$f = f_0 - \tau \cdot (\vec{v} \cdot \vec{\nabla}_{\vec{q}} f) \quad (3.3.13)$$

We arrive at (3.3.14) by first assuming that g is small and therefore its derivatives can be neglected. We also note that phonons are constant velocity plane waves that do not accelerate. Additionally we can incorporate quantum statistics recognizing that phonons

are bosons (quasi-particles), which allows us to describe the average phonon occupation with Bose-Einstein statistics at equilibrium, where the equilibrium distribution function is written as,

$$f_0 = \frac{1}{\exp\left(\frac{\hbar\omega}{k_B T}\right) - 1} \quad (3.3.14)$$

in which ω is the angular phonon frequency. The equilibrium distribution achieves spatial dependence through the temperature field resulting in,

$$f(q, k) = f_0 - \tau \cdot \left(\vec{v} \cdot \frac{df_0}{dT} \cdot \vec{\nabla} T \right). \quad (3.3.15)$$

Since we are initially interested in describing phonon transport along individual PE chains, we can describe the heat flow as one dimensional. For a single PE chain the heat flux can be written as a sum over phonon states propagating in the z direction along the PE chain backbone as:

$$J_{Qz} = \frac{1}{V} \cdot \sum_p \sum_{\vec{k}} \hbar\omega \cdot f \cdot v_z \quad (3.3.16)$$

where J_{Qz} is the component of heat flux in the z direction, V is the volume, p denotes the sum over all polarizations and \vec{k} is the wave vector. Substituting (3.3.15) into (3.3.16) leads to:

$$J_{Qz} = \frac{1}{V} \cdot \sum_p \sum_{\vec{k}} \hbar\omega \cdot v_z \cdot f_0 - \left(\hbar\omega \cdot \frac{df_0}{dT} \right) v_z^2 \tau \cdot (\vec{\nabla} T) \quad (3.3.17)$$

Taking the phonon dispersion relation as an even symmetric function about $\vec{k} = 0$ reduces (3.3.17) to:

$$J_{Qz} = \frac{-1}{V} \cdot \sum_p \sum_{\vec{k}} \left(\hbar\omega \cdot \frac{df_0}{dT} \right) v_z^2 \tau \cdot (\vec{\nabla} T) \quad (3.3.18)$$

since the phonon group velocity v is an odd function. This is expected because the equilibrium distribution should not contribute to the heat flux. Comparing (3.3.18) with Fourier's law for heat conduction (2.1.7), identifies the thermal conductivity κ for a one-dimensional molecular chain as,

$$\kappa = \frac{1}{V} \cdot \sum_p \sum_{\vec{k}} C v_z^2 \tau \quad (3.3.19)$$

which depends on the phonon specific heat C , velocity v and relaxation time τ . In the forthcoming section 3.4 we provide a brief description of lattice dynamics, which can be used to determine the phonon specific heats and group velocities. The phonon relaxation times, however, are more challenging to calculate. Nonetheless, we present a framework for extracting the phonon relaxation times from MD simulations based on the modal description obtained in lattice dynamics. We then conclude the chapter with a final derivation that combines normal mode analysis techniques with the Green-Kubo method for determining the modal contributions to the thermal conductivity, without the relaxation time approximation.

3.4 Lattice Dynamics

To determine the thermal conductivity, as expressed in (3.3.23), we must first determine the phonon specific heats and group velocities using lattice dynamics. Lattice dynamics is a generalized formulation that can provide a useful picture into the spectral characteristics of phonons. To introduce the formulation, we take a simple one-dimensional chain as an example and then proceed to a more general formulation involving the solution of an eigen value equation.

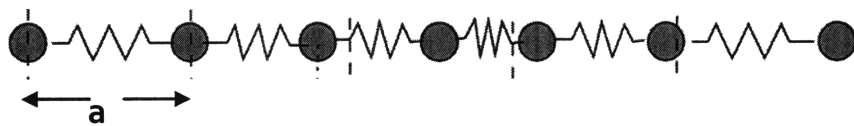


Figure 3.4.1 One-dimensional chain of atoms connected by springs

Consider the one-dimensional chain of atoms in Fig. 3.4.1, where each atom is connected with a spring to two neighboring atoms on each side. If we sum the forces and write down the equation of motion for the n^{th} atom in the chain, we have the following wave equation [23],

$$m_n \cdot \frac{d^2 u_n}{dt^2} = K(u_{n+1} - u_n) - K(u_n - u_{n-1}) \Rightarrow m_n \cdot \frac{\partial^2 u_n}{\partial t^2} = Ka^2 \frac{\partial^2 u_n}{\partial x^2} \quad (3.4.1)$$

where u_n is the displacement of the atom from equilibrium, the subscript n denotes its position in the chain, K is the spring constant, $\frac{\partial^2 u_n}{\partial t^2}$ is the acceleration and m is the mass of the atom. If we assume the chain to be infinite, taking the continuum limit, we arrive at an expression for u_n in (3.4.1), which is solved by a series of plane waves (normal modes)

$$u_n = A \cdot \exp(-i \cdot (\omega \cdot t - k \cdot n \cdot a)) \quad (3.4.2)$$

where k is a wave vector equal to $\frac{2\pi}{\lambda}$, in which λ is the wavelength corresponding to the wave's spatial periodicity and ω is its angular frequency. Inserting the solution into (3.4.2) yields an expression for the normal mode frequencies as a function of the wave vector $\omega(k)$,

$$\omega(k) = 2 \sqrt{\frac{K}{m}} \cdot \left| \sin\left(\frac{k \cdot a}{2}\right) \right|. \quad (3.4.3)$$

The dispersion relation given by (3.4.3) is a periodic solution in k and the maximum frequency is $2\sqrt{\frac{K}{m}}$. This simple case shows that when masses are connected together with long-range repetition, frequencies lower than the natural pair oscillator frequency appear in the temporal displacement of each atom. The periodic solution in k also illustrates an important symmetry property, namely, the highest unique k vector occurs at $k = \pi / a$. Shorter wavelengths beyond this k value, called the first Brillouin zone boundary, reproduce the same atomic displacements already associated with longer wavelengths occurring within the first Brillouin zone. Thus, the first Brillouin zone represents the shortest range of k vectors that result in unique solutions for the atomic displacements.

We now generalize the above treatment to three dimensions and any number of basis atoms. Rewriting (3.4.3) in matrix form, for an individual plane wave solution we arrive at the following [23]:

$$\omega^2(\vec{k}, \nu) \cdot \vec{e}(\vec{k}, \nu) = \mathbf{D}(\vec{k}) \cdot \vec{e}(\vec{k}, \nu) \quad (3.4.4)$$

where $\vec{e}(\vec{k}, \nu)$ is a complex polarization vector which depicts the direction of atomic displacements. Here, $\mathbf{D}(\vec{k})$ is the dynamical matrix containing the mass and stiffness information as $\mathbf{D}(\vec{k})$ is projected onto a particular propagation direction. The $\mathbf{D}(\vec{k})$ matrix elements are given by [23],

$$\mathbf{D}_{\alpha\beta}(jj', \vec{k}) = \frac{1}{(m_j \cdot m_{j'})^{\frac{1}{2}}} \cdot \sum_{l'} \phi_{\alpha\beta}(jj', 0l') \cdot \exp(i \cdot \vec{k} \cdot [\vec{r}(j'l') - \vec{r}(j0)]) \quad (3.4.5)$$

$$\phi_{\alpha\beta}(jj', 0l') = \frac{\partial^2 \Phi}{\partial u_\alpha(jl) \partial u_\beta(j'l')} \quad (3.4.6)$$

The indices j and j' label individual atoms, while l identifies the unit cell in which the atom j is located. The dynamical matrix is symmetric and Hermitian, guaranteeing real eigenvalues that are all positive for stable crystal structures. The eigenvectors, however, may be complex. The real and imaginary parts of each eigenvector correspond to the coefficients of an elliptically polarized wave.

Equation (3.4.6) expresses the essential assumption of lattice dynamics, which is the harmonic limit of the potential model. By Taylor expanding the potential, the first derivative term cancels out for equilibrium structures because the net forces are zero. The second derivative, however, is nonzero and can be interpreted as a harmonic or spring constant associated with a given potential in the equilibrium structure. For the case of an individual PE chain, we can employ the AIREBO potential [83] to determine the phonon dispersion. This can be accomplished by numerically computing the second derivatives in (3.4.6) for a periodic PE chain, which has 6 basis atoms. Application of the lattice dynamics model yields the eigen values and eigen vectors for each of the 18 polarizations shown in Fig. 3.4.2 where Figure 3.4.2a also shows the phonon dispersion computed for the Kirkwood model [72] of a polyethylene chain, which only consists of 4 phonon branches. Figure 3.4.2b shows a plot of the phonon dispersion for the bulk polyethylene lattice structure, based on an *ab initio* calculation of the force constants in (3.4.6) [86]. The bulk PE lattice structure consists of 12 basis atoms (2 chains), and thus there are 36 phonon polarizations in Fig. 3.4.2b. Comparison of Figs. 3.4.2a and 3.4.2b indicates that the AIREBO potential [83] exhibits a drastic improvement over Kirkwood's more simplified model [72]. Although the mid range optical phonon branches are slightly over

predicted with AIREBO, the acoustic polarizations are well described. Most importantly, the slopes of the acoustic polarizations, which equate to the phonon group velocities $v = \partial\omega/\partial k$, are well described by the AIREBO potential. The Kirkwood model, on the other hand, largely under predicts the phonon frequencies and velocities, which would have significant impact on the resulting calculation of phonon transport and thermal conductivity.

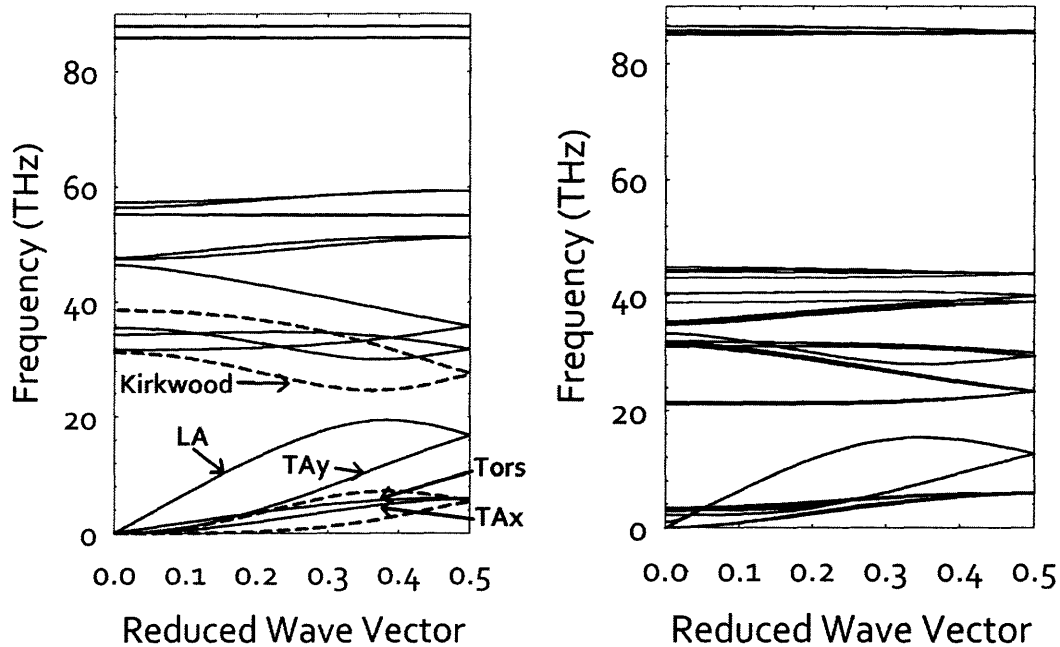


Figure 3.4.2 Phonon dispersion curves for polyethylene. (a) Phonon dispersion for a single PE chain using the AIREBO potential [83] (solid lines) and the Kirkwood model [72] (dashed lines). Text labels are used to identify the four acoustic polarizations: LA, TAy, Tax and Tors (see text) (b) Phonon dispersion of bulk PE using *ab initio* force constants [86].

The atomic displacements associated with each of the four acoustic polarizations are shown in Fig. 3.4.3. Based on scattering theories [25], these modes are expected to have the longest relaxation times and therefore the largest contributions to the thermal conductivity. As a result, we introduce abbreviations for these modes, which are labeled in Fig. 3.4.2a, because they will be discussed in greater detail in chapter 5. Here, Tax corresponds to the transverse acoustic modes with vibrations perpendicular to the C-C bonding plane (Fig. 3.4.3a), TAy corresponds to the transverse acoustic modes with vibrations in with the direction of the C-C bonds (Fig. 3.4.3c), LA corresponds to the

longitudinal acoustic modes with vibrations along the chain axis (Fig. 3.4.3d), and Tors corresponds to the torsional acoustic modes, which twist about the chain axis in/out of the C-C bonding plane (Fig. 3.4.3b) [93]. Once the phonon dispersion is determined, we can compute the individual modal/phonon contributions to the specific heat by expressing the energy as a sum of quantum harmonic oscillator energies,

$$E = \sum_p \sum_{\vec{k}} \hbar\omega \cdot f_0 \quad (3.4.7)$$

where f_0 is the Bose-Einstein distribution, which describes the average phonon occupation for each mode at temperature T . The specific heat can then be determined by taking the derivative of f_0 with respect to temperature,

$$C = \sum_p \sum_{\vec{k}} \frac{k_B \cdot x^2 e^x}{(e^x - 1)^2} \quad (3.4.8)$$

where

$$x = \hbar\omega / k_B T \quad (3.4.9)$$

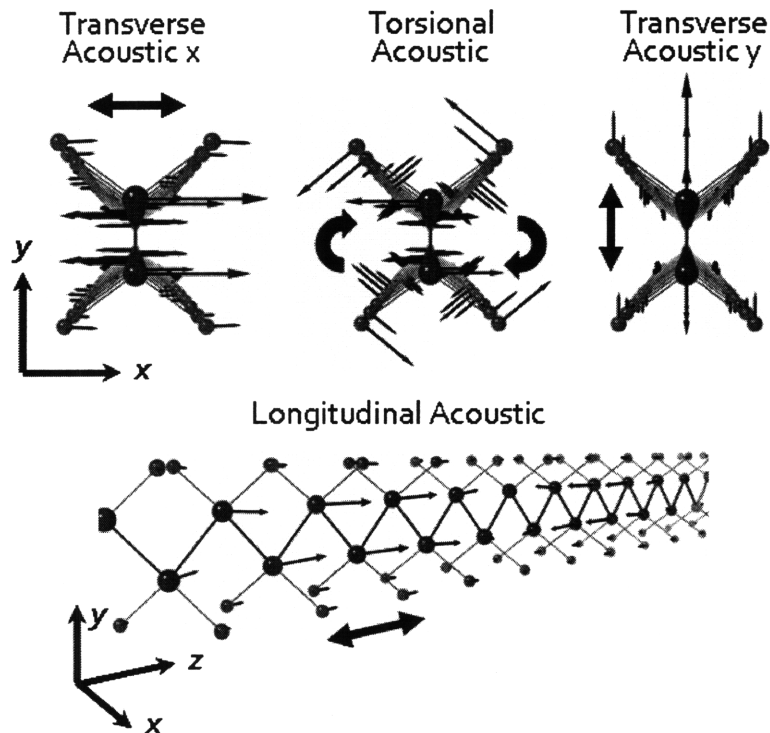


Figure 3.4.3 Atomic displacements for the 4 acoustic polarizations in a polyethylene chain.

3.5 Normal Mode Analysis

To determine the phonon relaxation times τ we can first decompose the atomic positions into normal mode contributions and track the normal energy content as a function of time. The temporal fluctuations in each mode's energy are caused by the nonlinear mode-mode/phonon-phonon interactions. As a result, we can use the time history of these mode energy fluctuations to compute each individual mode's autocorrelation function, which would reveal the time scale over which the mode loses memory of its original configuration. This time scale would then identify the normal mode attenuation rate which would then provide a measure of the phonon relaxation time τ for each mode. To this end, we begin by recalling that the lattice dynamics approach is based upon the harmonic approximation, and therefore allows us to expand the atomic displacements in terms of a Fourier series of normal modes. Under this framework, the atomic displacements can be written as [23, 30],

$$\bar{\mathbf{u}}(jl, t) = \frac{1}{(Nm_j)^{\frac{1}{2}}} \cdot \sum_{\bar{\mathbf{k}}, p} \bar{\mathbf{e}}(j, \bar{\mathbf{k}}, p) \cdot \exp(i\bar{\mathbf{k}} \cdot \bar{\mathbf{r}}(jl)) \cdot X(\bar{\mathbf{k}}, p) \quad (3.5.1)$$

where $\bar{\mathbf{u}}(jl, t)$ is the displacement of an atom labeled j in unit cell l with mass m , $\bar{\mathbf{e}}(j, \bar{\mathbf{k}}, p)$ is the mode eigenvector, $\bar{\mathbf{k}}$ is the wave vector, $\bar{\mathbf{r}}(jl)$ is the lattice site position and the time dependent amplitude of the mode is $X(\bar{\mathbf{k}}, p)$ where p denotes the mode polarization. Equation (3.5.1) represents an inverse Fourier decomposition of the atomic displacements where the original transform can be computed as [23, 30],

$$X(\bar{\mathbf{k}}, p) = \left(\frac{m_j}{N} \right)^{\frac{1}{2}} \cdot \sum_{j,l} \bar{\mathbf{e}}^*(j, \bar{\mathbf{k}}, p) \cdot \bar{\mathbf{u}}(jl, t) \cdot \exp(-i\bar{\mathbf{k}} \cdot \bar{\mathbf{r}}(jl)) \quad (3.5.2)$$

where the $*$ superscript in (3.5.2) implies that the complex conjugate of $\bar{\mathbf{e}}(j, \bar{\mathbf{k}}, p)$. $X(\bar{\mathbf{k}}, p)$ is also a generally complex quantity, although the actual atomic displacements are real values and can be computed by taking the real or imaginary part of the modal amplitudes. The quantity $X(\bar{\mathbf{k}}, p)$ is also time dependent and represents the instantaneous amplitude of a specific mode, which can then be used to compute the mode's total energy,

$$E(\vec{\mathbf{k}}, p, t) = \frac{1}{2} \omega^2 X^* \cdot X + \frac{1}{2} \dot{X}^* \cdot \dot{X} \quad (3.5.3)$$

where \dot{X} is the time derivative of the modal amplitude X . The mode energy is proportional to the phonon occupation and we can analyze the modal fluctuations by taking the deviation from the average energy $\langle E(t) \rangle$:

$$\delta E(t) = E(t) - \langle E(t) \rangle. \quad (3.5.4)$$

By tracking the mode energy fluctuations throughout the MD trajectory, we can then compute and integrate the normalized mode autocorrelation function, which gives the phonon relaxation time:

$$\tau(\vec{\mathbf{k}}, p) = \frac{\int_0^\infty \langle \delta E(t) \cdot \delta E(0) \rangle}{\langle \delta E^2(0) \rangle}, \quad (3.5.5)$$

This approach was originally proposed by Ladd *et al.* [94], later expanded upon by McGaughey and Kaviany [30], and was used to extract phonon mean free paths $\Lambda = v \cdot \tau$ in silicon by Henry and Chen [29]. This MD simulation-based approach allows for calculation of phonon relaxation times without fitting parameters. Analytical approaches, usually based on scattering theory, are often limited to a single type of scattering (3-phonon, Normal, Umklapp) under a specific set of conditions (high ω , high T etc.) and often neglect effects such as dispersion and scattering with optical modes [25, 95]. Furthermore these methods require fitting parameters to existing experimental data, which can be unreliable. This severely limits the predictive power of these methods. The MD method, on the other hand, does not suffer from such constraints and is closer in concept to a first principles-based approach to computing relaxation times.

One limitation of the preceding derivation is that it is based upon the relaxation time approximation [25]. The relaxation time approximation is a secondary approximation to the scattering integral in the Boltzmann equation (3.3.12). This approximation however, was based on Boltzmann's assumption of molecular chaos [92]. One way to avoid the necessity of this assumption, would be to derive an expression for the modal contributions to the thermal conductivity, starting from the Green-Kubo result (3.2.15). Assuming the system's response is linear (small deviations from equilibrium)

the resulting expression would be valid for any phase of matter and therefore would not provide any detailed information about phonon transport in crystalline materials. These details, however, can be included in the Green-Kubo expression, by expressing the heat flux in terms of its modal contributions. For a one dimensional system, such as a PE chain, we express the heat flux as [25]:

$$Q_z = \frac{1}{V} \sum_k \sum_p \hbar\omega \cdot v_z \cdot \delta n(t) \quad (3.5.6)$$

where δn is the deviation from the average occupation number. Inserting Eq. (3.5.6) into Eq. (3.2.15) results in an expression for the thermal conductivity in terms of the normal mode-mode correlation functions [25],

$$\kappa = \frac{1}{Vk_B T^2} \sum_k \sum_p \sum_{k'} \sum_{p'} (\hbar\omega \cdot \hbar\omega') \cdot (v \cdot v') \int_0^\infty \langle \delta n(t) \cdot \delta n'(t+t') \rangle dt' \quad (3.5.7)$$

Here we can make use of Wick's factorization scheme [25],

$$\langle abcd \rangle = \langle ab \rangle \langle cd \rangle + \langle ac \rangle \langle bd \rangle + \langle ad \rangle \langle bc \rangle \quad (3.5.8)$$

to determine the squared deviation from the average occupation number $\langle \delta n^2 \rangle$, by substituting the creation and annihilation operators \hat{a} and \hat{a}^\dagger for the occupation n ,

$$\begin{aligned} \langle \delta n^2 \rangle &= \langle n^2 \rangle - \bar{n}^2 \\ &= \langle \hat{a}^\dagger \hat{a} \hat{a}^\dagger \hat{a} \rangle - \bar{n}^2 \\ &= \langle \hat{a}^\dagger \hat{a} \rangle \langle \hat{a}^\dagger \hat{a} \rangle + \langle \hat{a}^\dagger \hat{a}^\dagger \rangle \langle \hat{a} \hat{a} \rangle + \langle \hat{a}^\dagger \hat{a} \rangle \langle \hat{a} \hat{a}^\dagger \rangle - \bar{n}^2 \\ &= \bar{n}(\bar{n} + 1) \end{aligned} \quad (3.5.9)$$

where \bar{n} is the average occupation number,

$$\bar{n} = \left(\exp\left(\frac{\hbar\nu}{k_B T}\right) - 1 \right)^{-1}. \quad (3.5.10)$$

This factorization scheme then allows us to express the thermal conductivity in terms of the normalized correlation functions $\frac{\langle \delta n(t) \cdot \delta n'(t+t') \rangle}{\sqrt{\langle \delta n^2(t) \rangle \cdot \langle \delta n'^2(t) \rangle}}$, which can be calculated from

the MD trajectory data through:

$$\kappa = \frac{1}{V} \sum_k \sum_p \sum_{k'} \sum_{p'} k_B \left(\frac{x \cdot e^{x/2}}{(e^x - 1)} \cdot \frac{x' \cdot e^{x'/2}}{(e^{x'} - 1)} \right) (\mathbf{v} \cdot \mathbf{v}') \int_0^\infty \frac{\langle \delta n(t) \cdot \delta n'(t+t') \rangle}{\sqrt{\langle \delta n^2(t) \rangle \cdot \langle \delta n'^2(t) \rangle}} dt' \quad (3.5.11)$$

where, $x = \hbar\omega/k_B T$. By identifying the specific heat from (3.4.8), equation (3.5.11) can

be cast more intuitively as,

$$\kappa = \frac{1}{V} \sum_k \sum_p \sum_{k'} \sum_{p'} \sqrt{C_{k,p} \cdot C_{k',p'}} \cdot (\mathbf{v}_{k,p} \cdot \mathbf{v}'_{k',p'}) \int_0^\infty \frac{\langle \delta n_{k,p}(t) \cdot \delta n'_{k',p'}(t+t') \rangle}{\sqrt{\langle \delta n_{k,p}^2(t) \rangle \cdot \langle \delta n'_{k',p'}^2(t) \rangle}} dt'. \quad (3.5.12)$$

Inspection of (3.5.12) reveals several interesting features that bear resemblance to the way the thermal conductivity is expressed when derived from the Boltzmann transport equation, using the relaxation time approximation. In (3.3.23) the relaxation time τ includes all possible phonon-phonon scattering interactions. The key difference between (3.3.23) and (3.5.12) is that the relaxation time in Eq. (3.3.23) is based on the Boltzmann equation, which hinges on the assumption that phonon-phonon scattering events are not correlated. The cross-terms in Eq. (3.5.12), where $k \neq k'$ or $p \neq p'$, account for the possibility that phonon-phonon scattering events could be correlated, which would violate the Stosszahlansatz assumption of molecular chaos [92]. In previous works, where molecular dynamics simulations were used to study the thermal conductivity, only the terms where $k = k'$ and $p = p'$ were included in accordance with (3.3.23) and (3.5.5) [29, 30, 94, 96]. The added correlation features captured by (3.5.12), in fact, will be important for understanding anomalous heat conduction in 1D PE chain molecules.

3.6 Simulation Procedures

To investigate the phonon transport in single PE chains and PE lattices, we implemented the AIREBO potential into the large atomic/molecular parallel simulator (LAMMPS). Every simulation employed periodic boundary conditions along the chain axis in the z direction. All simulations were run at constant energy, volume and number of atoms corresponding to the microcanonical ensemble. Based on preliminary testing a time step of 0.25 fs was used in each simulation to achieve good energy conservation,

with total energy variations less than 0.001%. Preliminary testing also indicated that 10 ns of simulation time were required for thermal conductivity convergence within $\pm 20\%$. As a result all simulations were run for 10 ns and very little dependence ($< \pm 5\%$) on equilibration time was observed. Each simulation was initialized with all atoms at the equilibrium positions and random velocities corresponding to room temperature (300K), based on the quantum-corrected temperature definition, given in (3.1.19). The minimum energy positions of the atoms were determined by standard line search methods in LAMMPS and the resulting PE lattice unit cell dimensions were $7.1 \text{ \AA } \hat{x}$, $5.0 \text{ \AA } \hat{y}$, $2.578 \text{ \AA } \hat{z}$ in the orthombic lattice structure (Fig. 1.3.2), which is within 4% of the values measured experimentally [97]. For single chains, these unit cell dimensions were used to determine the chain volume, as the chain length multiplied by an $\sim 18 \text{ \AA}^2$ cross sectional area [97]. This choice allowed for a direct comparison with results for PE chain lattices [97].

For the single chain simulations, we studied chains that were 10, 20, 40, 80, 120, and 200 unit cells long. For the several cases where isotopes were added, which will be discussed in sections 4.1 and 4.2, approximately 3 times the highest naturally occurring isotope density was used, which corresponded to $\sim 3\text{-}4\%$ for carbon and hydrogen. This resulted in 3 randomly distributed C13 atoms and 5 randomly distributed deuterium atoms replacing atoms in the 40 unit cell long chains, which contain a total of 240 atoms. In each of the computed autocorrelation and cross-correlation functions only half of the simulated data was used, so that the correlation values obtained at $t = 5 \text{ ns}$ consisted of the same sample size as the correlation values at $t = 0$. For each simulation heat flux autocorrelation and normal mode energy data were recorded after each time step, which allowed for flexibility and high resolution in the data analysis.

The Lennard-Jones term of the AIREBO potential allows for a user-specified long ranged cut-off. In the present work, this cut-off was chosen as three times the minimum energy separation σ for the Lennard-Jones interaction of the associated atomic species, which corresponded to $\sim 10 \text{ \AA}$ for carbon-carbon interactions and $\sim 8 \text{ \AA}$ for hydrogen-hydrogen interactions. This allowed for chain-chain interactions between third and fourth nearest neighboring chain molecules.

The PE lattice simulations were run on large processor grids, ranging from 2-30 processors, due to the larger system sizes and long run-times. Ten independent simulations were run for each system of PE chains, by using the same initial positions and different random seed integers for the random number generator. In all systems, periodic boundary conditions were applied along the length of the chains. The boundary conditions in the remaining two directions, however, were modified in each case to examine the anticipated 1D-to-3D transition. Table 3.6.1 lists the system sizes and boundary conditions used in each simulation.

Table 3.6.1 Simulation parameters for PE chain lattice simulations (see Fig. 5.1.1)

Dimensionality of the Phonon Transport	Molecules Stacked in x-Direction	Periodic Boundaries in x-Direction	Layers Stacked in y-Direction	Periodic Boundaries in y-Direction	Number of Molecules	Number of Atoms
1D	1	No	1	No	1	240
1D-2D	2	No	1	No	2	480
1D-2D	4	No	1	No	4	960
1D-2D	6	No	1	No	6	1440
1D-2D	12	No	1	No	12	2880
2D	12	Yes	1	No	12	2880
2D-3D	6	Yes	1	No	6	1440
2D-3D	6	Yes	2	No	12	2880
2D-3D	6	Yes	3	No	18	4320
2D-3D	6	Yes	4	No	24	5760
2D-3D	6	Yes	5	No	30	7200
3D	6	Yes	5	Yes	30	7200

The remaining chapters discuss the results of the simulations for single chains and chain lattices according to the procedures outlined above. In each case, many independent simulations were run under the previously described conditions for improved statistical averaging. Chapter 4 discusses the single chain simulation results and focuses on understanding and explaining the divergent phenomena that were observed. Chapter 5 focuses on how the high thermal conductivity of individual chains is altered by the presence of neighboring chains which induce phonon-phonon scattering through van der Waals interactions. Chapter 6 provides concluding remarks and summarizes the observations of the various aspects of this investigation.

Chapter 4: Single Chain Results

To start our investigation we began with simulations of single PE chains in order to study the fundamental upper limit imposed by phonon-phonon interactions alone. To this end, we ran simulations of individual PE chains with periodic boundary conditions applied along the length of the chain to probe the limiting behavior of an infinitely long chain. By removing the presence of boundaries, we are able to study phonon-phonon interactions in isolation. In this chapter we first show Green-Kubo results for single chains and then proceed to more detailed modal analysis which revealed a new mechanism for anomalous heat conduction that, to the best of our knowledge, has not been previously considered [38, 39, 47].

4.1 Divergent Thermal Conductivity

Figure 4.1.1 shows a heat flux autocorrelation (HFAC) function for a single PE chain. Immediately identifiable from the plot is a strong oscillatory component at ~ 50 THz. Although these oscillations are strong, they are symmetric about zero and therefore do not contribute to the thermal conductivity, which is obtained by integrating the HFAC with respect to time. To highlight the decaying features of the HFAC we also show a plot of the local average HFAC values, which suppresses the effect of the large 50 THz oscillations. From this smoothed version of the data, it is possible to see its decay. When integrated, at short times < 1 ns, the HFAC results in a positive value for the thermal conductivity. Figure 4.1.2 shows the Green-Kubo thermal conductivity with respect to the amount of integration time for short simulation domains 10 and 20 unit cells in length. This cumulative integration of the heat flux autocorrelation function shows that the thermal conductivity is high ~ 450 W/mK. These results, which are averaged over 10 independent simulations, also indicate that the thermal conductivity is convergent with respect to integration time. This non-divergent behavior is typical and has been observed

in all previous studies of other materials that utilize the Green-Kubo formula. However, when the chain length was increased to 40 unit cells and larger, the integration of the HFAC function for several cases exhibited distinctly different behavior. Upon observation of this abnormal result, we probed further by simulating many more cases of 40, 80 and 120 unit cell long chains. Figure 4.1.3 shows a convergent simulation of a 40 unit cell chain and divergent cases for 40, 80 and 120 unit cell chains. The convergent 40 unit cell simulation oscillates around 200 W/mK, while the others diverge and exceed 1,000 W/mK after 5 ns. In studies of other materials, where the Green-Kubo method was used, the integration of HFAC functions typically converged within the first 500 picoseconds. Here, however, in order to consider the possibility of divergence, we have extended the integration to 5 ns, where a typical simulation would run for 3-4 days on 64-bit 3.0 GHz Xeon dual processor servers. This type of diverging behavior has also been observed in previous studies that use different techniques to study simplified models [38, 39, 45-49, 52, 54-56, 60-62, 68]. The major difference here is that we used a more realistic model and expected the strongly embedded anharmonicity and inclusion of hydrogen atoms to discourage such behavior in our simulations. After careful checking for coding errors or sources of accumulated machine error, it was concluded that the divergent behavior shown in Fig. 4.1.3 was caused by some nonlinear feature of the AIREBO model, which may correspond to a physically meaningful characteristic of the phonon transport in PE chains.

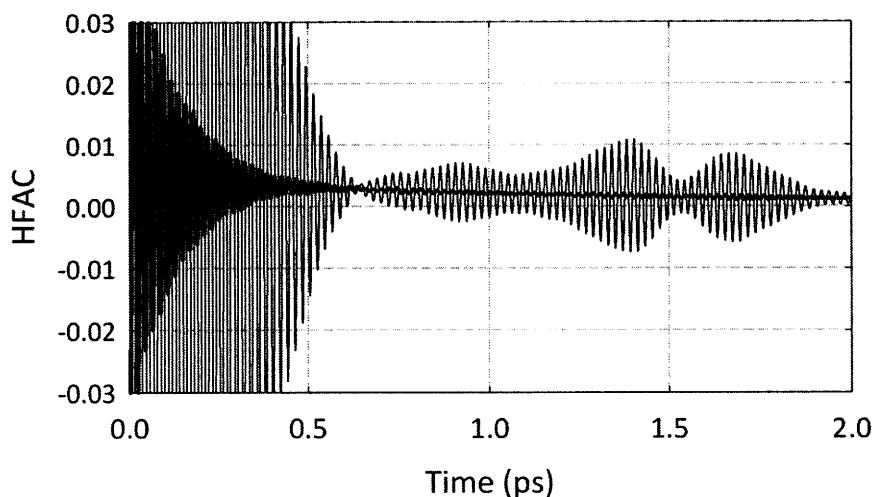


Figure 4.1.1 The heat flux autocorrelation function for a 40 unit cell long chain. The raw data (black line) and smoothed function (red line), based on local average values (1 ps intervals) are shown to highlight its decaying features.

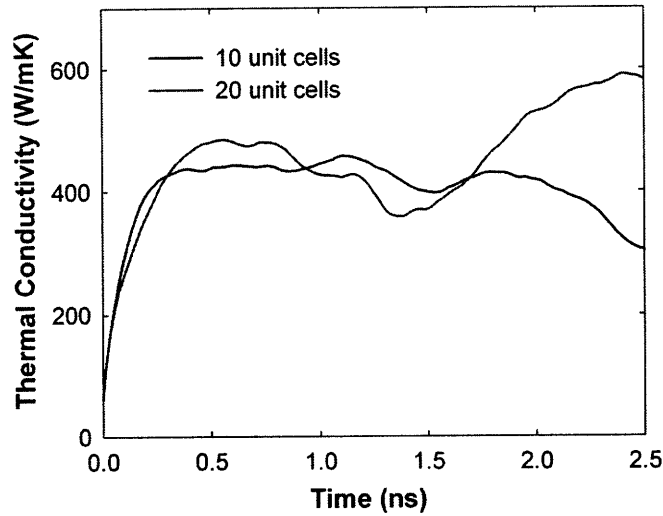


Figure 4.1.2 Average Green-Kubo thermal conductivity integral for 10 and 20 unit cell simulations.

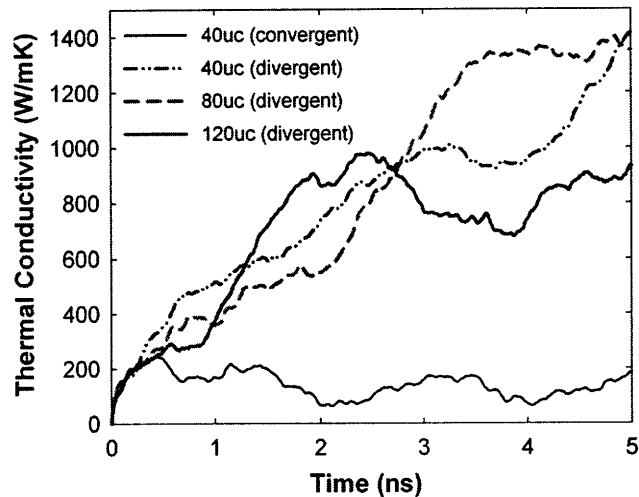


Figure 4.1.3 Green-Kubo thermal conductivity integral for individual 40, 80 and 120 unit cell simulations, showing both convergent and divergent behaviors.

To further investigate this phenomenon we simulated over 60 independent cases of 40 unit cell chains with different random initial velocities. Of the 60 independent simulations that were run, all of the remaining results discussed in this section correspond to the data obtained from the 6 example cases shown in Fig. 4.1.4. These example cases were selected because they exhibited strongly contrasting behavior. When compared to

the 6 cases shown in Fig. 4.1.4, all of the other 54 simulations exhibited similar converging/diverging or intermediate behaviors. Cases 1-4 were conducted under identical conditions, with the only difference being that the random initial velocities (random number seed) differed, which subsequently lead to different phase space trajectories. To further test whether or not the divergent behavior was a result of a physically meaningful aspect of the AIREBO model, we re-simulated the divergent cases 3 and 4 with the same initial velocities, but changed the mass of 3 randomly selected carbon atoms and 5 randomly selected hydrogen atoms to heavier isotopes. Initially, the divergent integrals observed in cases 3 and 4 resulted from the incomplete decay of the HFAC function, which has a persistent tail with a small but positive offset. When these same divergent simulations are run with isotopes present, the previously persistent HFAC tails no longer endure, leading to a convergent integral (Fig. 4.1.4). This response to a physical modification of the problem suggests that the divergent phenomenon is not a result of unphysical numerical artifacts. Instead, this result suggests that the divergence is related to some aspect of the phonon transport, which can be affected by isotope scattering [82]. It is also important to note that the large oscillations in Fig. 4.1.4 are due to the fact that each curve corresponds to the results of an individual simulation trajectory. In typical studies employing the Green-Kubo method, these oscillations are usually suppressed by averaging over many independent simulations. However, for the remainder of this section, we focus on analysis and on an explanation of the strong divergence in cases 3 and 4 specifically.

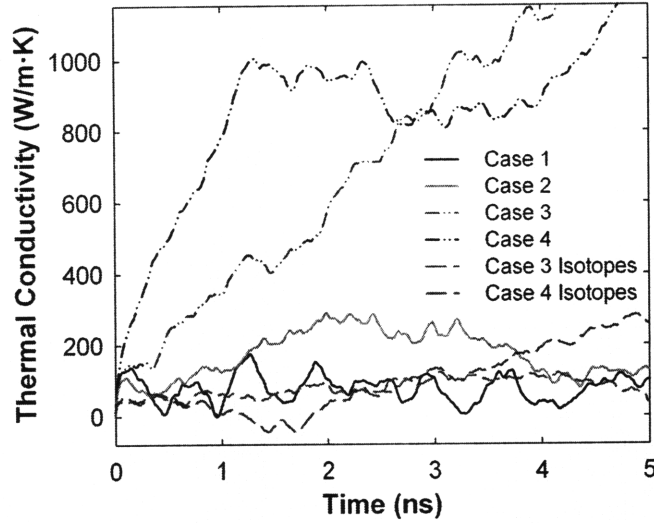


Figure 4.1.4 Green-Kubo thermal conductivity integrals for 5 independent simulations, which exhibited contrasting behavior. Cases 1-4 use identical simulation parameters and procedures, but were initialized with different random velocities. Cases 5 and 6 use the same initial velocities as cases 3 and 4 respectively; however the masses of 3 carbon atoms and 5 hydrogen atoms were increased to heavier isotopes.

4.2 Normal Mode Analysis

With the 6 cases shown in Fig. 4.1.4 under consideration, we used the previously discussed modal analysis technique in conjunction with the Green-Kubo method to calculate the normal mode correlation functions and their respective contributions to the net thermal conductivity (Eq. (3.5.12)). Figure 4.2.1 shows several normal mode correlation functions corresponding to modes with wavelengths of 40 unit cells (ucs), for the divergent case 3. In Figs. 4.2.1-4.2.5, the value n denotes the wave vector as $k = n \cdot 2\pi / 40\text{ucs}$, while the value for p denotes the corresponding polarization. For the polarization, p , we have used the abbreviations TAx, TAy, LA and Tors as described in chapter 3. Each figure panel contains a title with the two modes and polarizations listed in parentheses. Figures 4.2.1(a-d) show the autocorrelation functions for the longest wavelength modes in each acoustic branch (divergent case 3). Other autocorrelation functions for the optical modes were also calculated, but they all exhibited decaying

behavior with time constants between 0.1-5 ps. Although optical modes have much smaller and often negligible contributions to thermal conductivity [29, 95], they can play an important role in heat conduction by scattering with acoustic modes [95].

Decaying behavior was also observed for the acoustic mode autocorrelations. However, Figs. 4.2.1(a) and 4.2.1(c) show that the TAx and Tors modes behave differently and do not fully decay within 5 ns. This persistent correlation suggests that these modes do not fully attenuate, as predicted by mode-coupling theory based explanations of anomalous heat conduction [47]. In accordance with mode-coupling theory, the non-attenuating modes were the lowest frequency, longest wavelength modes in the system [47]. The atomic displacements for the two polarizations (TAx and Tors) correspond to the out of C-C bonding plane vibrations, which are the least stiff and therefore yield the lowest branches of frequencies in the dispersion. Figures 4.2.1(b) and 4.2.1(d), on the other hand correspond to the stiffer TAY and LA vibrations which occur within the C-C bonding plane. Unlike the two non-attenuating modes in the TAx and Tors polarizations, all of the modes in the TAY and LA polarizations decay within 500 ps, which is consistent with normal diffusive transport, even though the decay time is long.

Motivated by mode-coupling theory-based explanations of divergent thermal conductivity, the persistent TAx and Tors correlations were initially thought to be the source of the divergent phenomenon. This mechanism for divergence, however, was questionable because the TAx and Tors autocorrelation functions persisted in all cases. Even in cases 1 and 2 where the results converged, these TAx and Tors modes exhibited non-attenuating behavior similar to that of case 3, shown in Figs. 4.2.1(a) and 4.2.1(c). The idea that this could explain the divergence in Fig. 4.1.4 was further invalidated by calculation of each correlation's respective contribution to the thermal conductivity using (3.5.12), which is shown in each panel with the right-side vertical axis. Examination of the cumulative thermal conductivity contribution for each of these modes, via the integral in (3.5.12), shows that despite the fact that these modes do not fully decay, their contribution to the thermal conductivity is only of order 10 W/mK. Contributions of this magnitude are not large enough to account for the rate of the divergence observed for cases 3 and 4 in Fig. 4.1.4. Even though the cross-correlation between the TAx and Tors modes reaches as high as 0.2, implying that 20% of the energy fluctuations are correlated,

the corresponding thermal conductivity contributions are still unable to account for the large persistent slopes in Fig. 4.1.4. The LA mode autocorrelation (Fig. 4.2.1(d)), however, has a much larger contribution, because the LA velocities are $\sim 16,000$ m/s. Although this mode's contribution is stronger, its autocorrelation decays within 500ps, which cannot account for the positive slope at 5 ns, for case 3 in Fig 4.1.4.

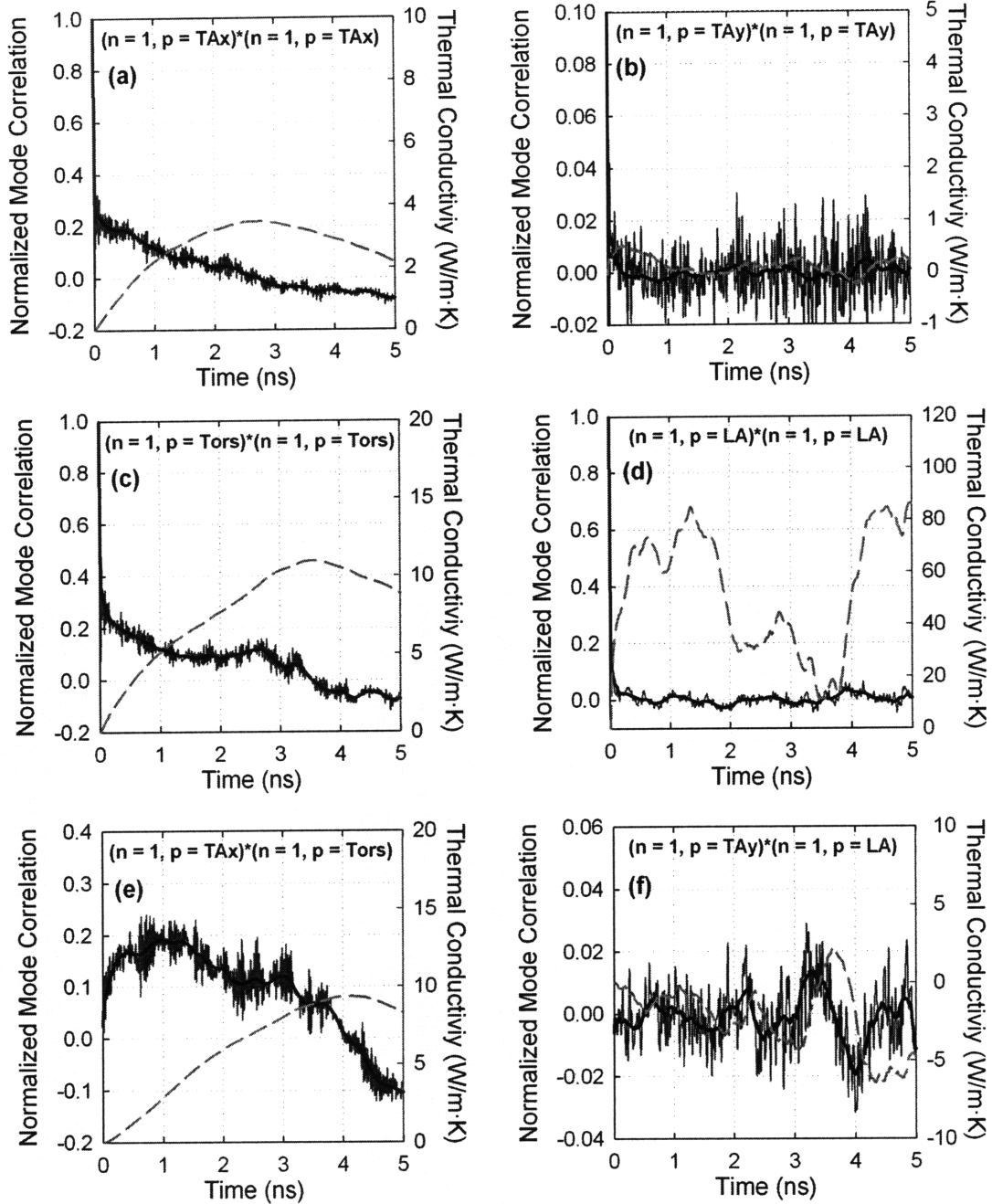


Figure 4.2.1 Normal mode correlation functions (fluctuating lines) and thermal conductivity contributions (gray-dashed lines) for the longest wavelength modes ($\lambda = 40ucs$) of the four acoustic polarizations in case 3. In each panel the correlation corresponds to the two modes indicated by wave vector index n and polarization p . The raw data (left-vertical axis) is shown with light, solid, thin lines. Smoothed local average values (left-vertical axis) are shown with dark, solid, thick lines. (a), (b), (c) and (d) show mode autocorrelations, while (e) and (f) show cross-correlations. In each panel the cumulative contribution to the thermal conductivity (right-vertical axis), based on (3.5.12), is shown with gray-dashed lines.

Examination of (3.5.12) shows that cross-correlations can also contribute to the thermal conductivity. Figures 4.2.1(e) and 4.2.1(f) show cross-correlations between the two non-attenuating TAx and Tors modes, as well as the decaying TAx and LA modes which have higher velocities. The panels of Fig. 4.2.2 show several cross-correlations for shorter wavelength modes in the TAx and Tors polarizations, but these cross-correlations also show minimal contributions to the thermal conductivity. Although these cross-correlations do not explain the divergent results in Fig. 4.1.4, the small cross-correlation oscillations in Figs. 4.2.2(e), 4.2.2(f) and 4.2.3(a-d) support the notion that the cross-terms of (3.5.12) may be negligible in many cases, particularly for 3D materials where divergent conductivity is not expected.

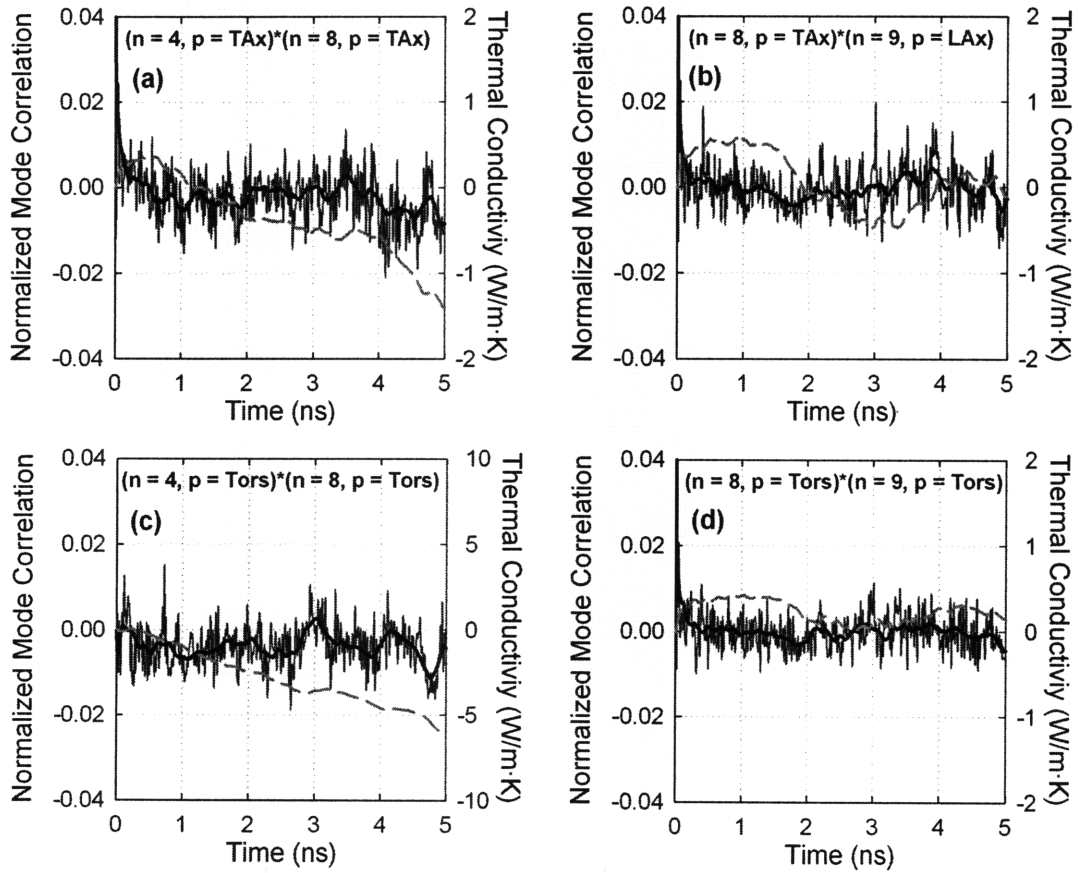


Figure 4.2.2 Normal mode cross-correlation functions (fluctuating lines) and thermal conductivity contributions (gray-dashed lines) for TAx and Tors polarizations in case 3. In each panel the correlation corresponds to the two modes given by wave vector index n and polarization p . The raw data (left-vertical axis) is shown with light, solid, thin lines. Smoothed local average values (left-vertical axis) are shown with dark, solid, thick lines. The cumulative contribution to the thermal conductivity (right-vertical axis), based on (3.5.12), is shown with gray-dashed lines.

In order to explain the large rate of divergence in Fig. 4.1.4, we can see from inspection of (3.5.12) that the phonon group velocity plays the strongest role in determining contributions to the thermal conductivity. A rough inspection of the phonon dispersion for polyethylene indicates that correlations between the LA phonons will have the strongest contribution to the thermal conductivity. Figure 4.2.3 shows several LA cross-correlations for the divergent case 3. Figure 4.2.3(a) shows that the correlation between the $n=4$ and $n=8$ modes persists up to 5 ns. The corresponding contribution to the thermal conductivity is on the order of 100 W/mK, which is 5-10 times higher than that of other polarizations. Figure 4.2.3(b) shows a very interesting feature of the divergent LA cross-correlations at short times. In the first 400 ps, the cross-correlation decays with oscillations, bearing strong resemblance to normal mode autocorrelations. The key feature in Fig. 4.2.3(a) is that the cross-correlation oscillates with a small positive offset, which causes its integral to increase over the entire duration considered. Several other persistent LA cross-correlations are also shown in Figs. 4.2.3(c) and 4.2.3(d), which indicate that the $n=4$ and $n=8$ cross-correlation is not the only combination that gives rise to this diverging trend. Figures 4.2.3(e) and 4.2.3(f), however, show that not all combinations of LA modes give rise to a persistent tail. Nonetheless, the combined effect of the several different LA mode combinations that have persistent tails, when $\pm k$ values are considered, results in a large enough contribution that can account for the magnitude of the divergent slopes in Fig. 4.1.4. A more complete correspondence would require computation of all possible cross-correlation combinations, which is beyond our current computing capability. The results in Fig. 4.2.3, however, offer a possible explanation for the divergence observed in the Green-Kubo results of Fig. 4.1.4.

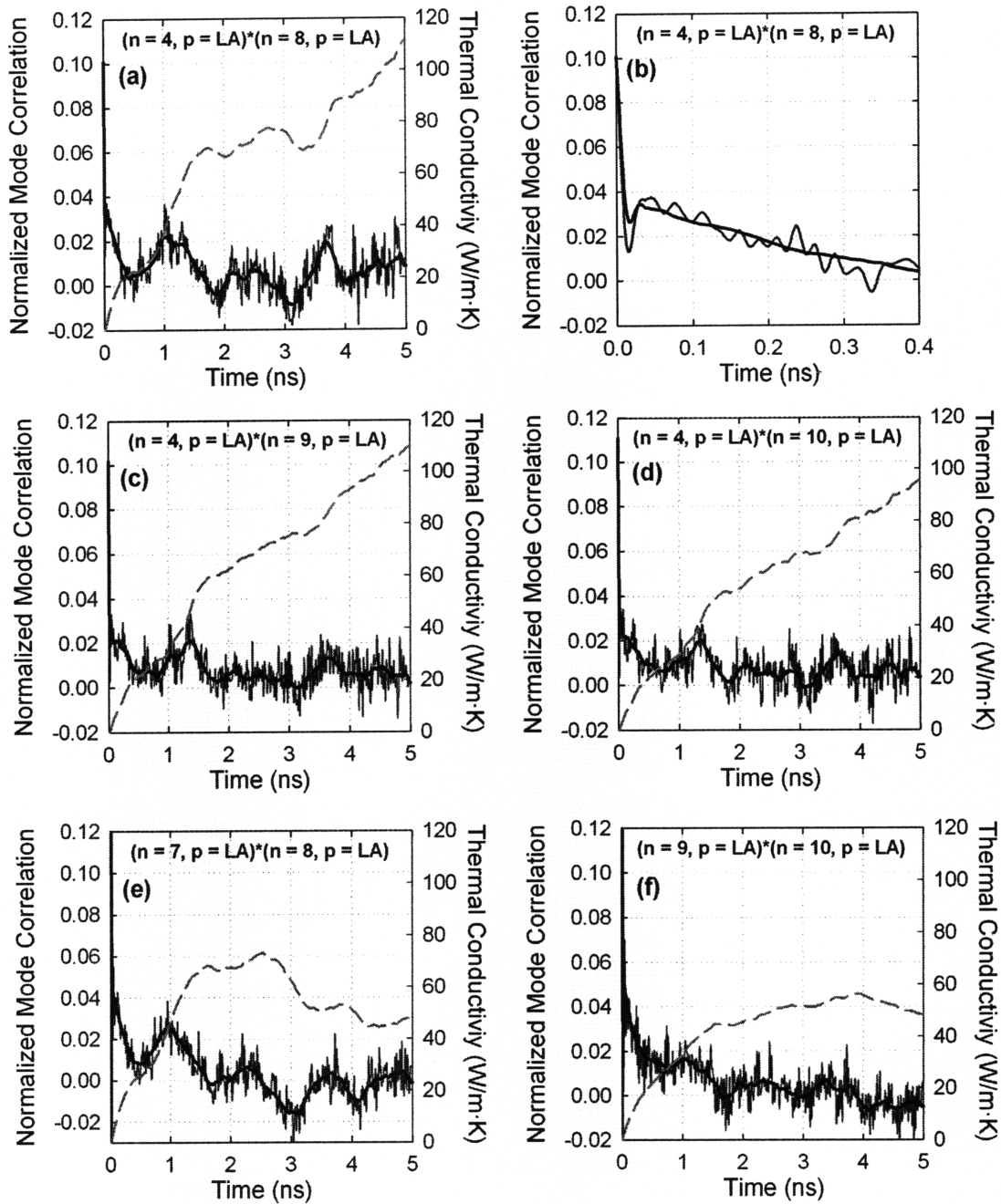


Figure 4.2.3 Normal mode correlation functions (fluctuating lines) and thermal conductivity contributions (gray-dashed lines) for LA modes in case 3. In each panel the correlation corresponds to the two modes indicated by wave vector index n and polarization p . The raw data (left-vertical axis) is shown with light, solid, thin lines. Smoothed local average values (left-vertical axis) are shown with dark, solid, thick lines. The cumulative contribution to the thermal conductivity (right-vertical axis), based on (3.5.12), is shown with gray-dashed lines. (b) illustrates the short time behavior of the correlation in (a).

To test the results of Fig. 4.2.3 as a possible explanation for the divergent HFAC integrals in cases 3 and 4, we also computed LA cross-correlations for the convergent cases 1 and 2, which are shown in Fig. 4.2.4. Figure 4.2.4 shows that when the same cross-correlations, which were divergent for case 3 (Figs. 4.2.3(a-d)), are computed for the convergent cases 1 and 2, the contributions to the thermal conductivity oscillate about zero. This lends support to our explanation for the divergence, which is only associated with cases 3 and 4. This also supports our hypothesis that cross-correlations may be negligible in many cases where normal chaotic phonon collisions are expected.

To further test our hypothesis, we also computed LA cross-correlations for case 4 and compared them to case 5, which uses the same initial velocities, but also includes isotopes. By comparing the correlations and thermal conductivity contributions in Figs. 4.2.5(a), 4.2.5(c) and 4.2.5(e) with that of Figs. 4.2.5(b), 4.2.5(d) and 4.2.5(f), we see that the presence of isotopes significantly decreases the LA correlation's contribution to the thermal conductivity. From the cross-correlation results in Fig. 4.2.5, we see that the presence of isotopes inhibits the persistent correlation, which subsequently caused the HFAC divergence for case 4 in Fig. 4.1.4.

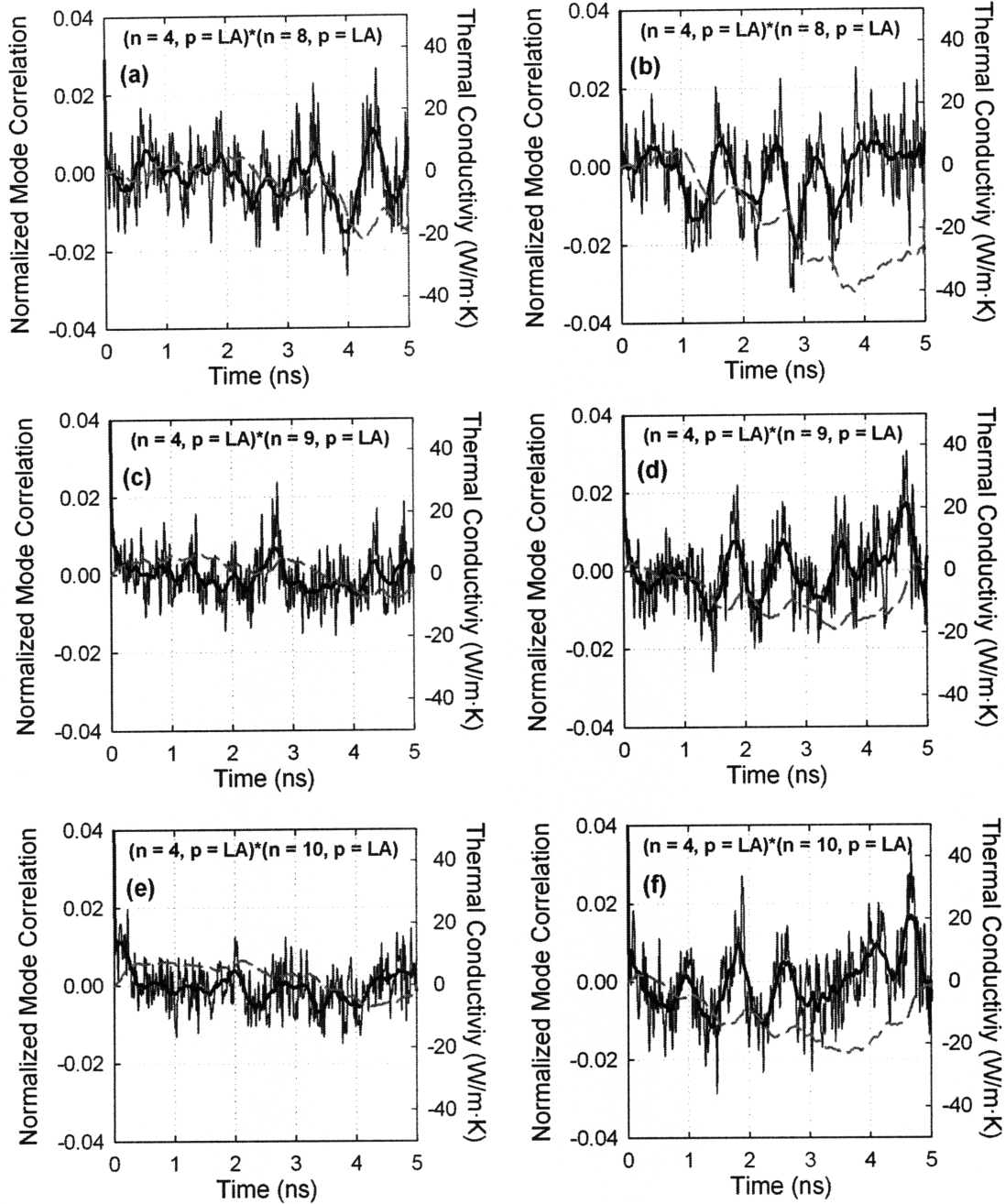


Figure 4.2.4 Normal mode correlation functions (fluctuating lines) and thermal conductivity contributions (gray-dashed lines) for LA modes in cases 1 and 2. (a), (c) and (e) correspond to case 1, while (b), (d) and (f) correspond to case 2. In each panel the correlation corresponds to the two modes indicated by wave vector index n and polarization p . The raw data (left-vertical axis) is shown with light, solid, thin lines. Smoothed local average values (left-vertical axis) are shown with dark, solid, thick lines. The cumulative contribution to the thermal conductivity (right-vertical axis), based on (3.5.12), is shown with gray-dashed lines.

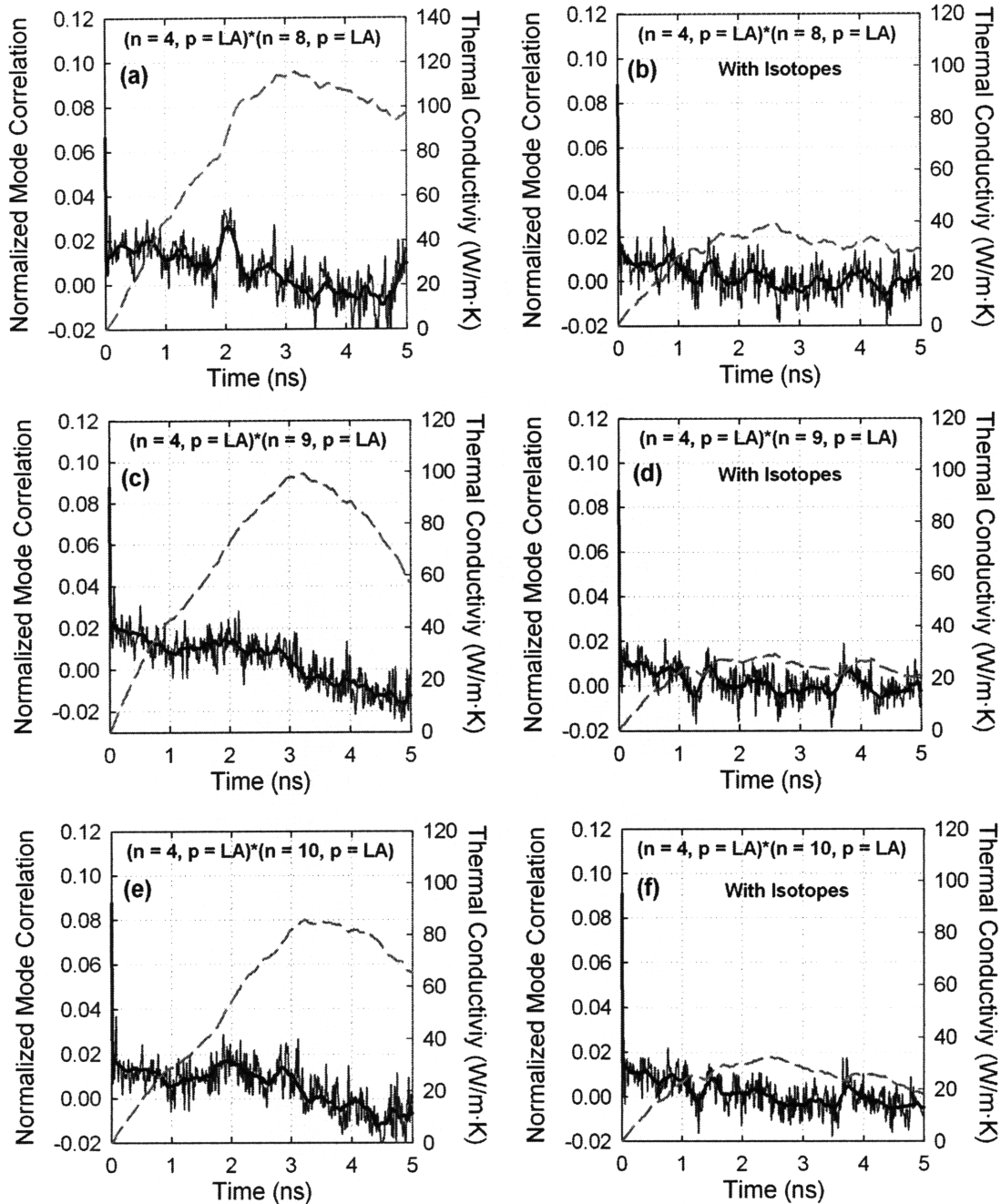


Figure 4.2.5 Normal mode correlation functions (fluctuating lines) and thermal conductivity contributions (gray-dashed lines) for LA modes in case 4 and case 5. (a), (c), and (e) correspond to data from divergent case 4, while (b), (d) and (f) correspond to case 5, which is equivalent to case 4 with the addition of isotopes. In each panel the correlation corresponds to the two modes indicated by wave vector index n and polarization p . The raw data (left-vertical axis) is shown with light, solid, thin lines. Smoothed local average values (left-vertical axis) are shown with dark, solid, thick lines. The cumulative contribution to the thermal conductivity (right-vertical axis), based on (3.5.12), is shown with gray-dashed lines.

4.3 Divergent Behavior Interpretation

Based on the results of Figs. 4.2.1-4.2.5, we believe the HFAC divergence is caused by persistent cross-correlations between certain LA modes. This persistent correlation points to a different explanation for anomalous heat conduction as opposed to the more commonly used explanation which is based on hydrodynamic mode coupling theory [47]. In order to explain our observations we propose a dual paradigm approach to understanding the heat conduction mechanisms, which is illustrated in Fig. 4.3.1. The traditional viewpoint for understanding lattice thermal conductivity is based on the evaluation of phonon scattering rates [25, 27]. In this paradigm, we begin from the idealization of a perfectly harmonic crystal, where the system's normal modes/phonons are non-interacting. In this limit, the thermal conductivity of the crystal is infinite. The next step is then to consider anharmonicity, which is the degree of departure from this idealization. Anharmonicity leads to Umklapp scattering, finite scattering rates and finite thermal conductivity as illustrated on the right side of Fig. 4.3.1. From this view point, it is thought that the sequence of scattering events is random, and this perspective leads to full consistency with Fourier's law for heat conduction. The results of the famous FPU problem, however, are difficult to understand from this view point. From this scattering based paradigm, the FPU system exhibits phonon-phonon scattering through its mode-mode interactions and should therefore have finite thermal conductivity. It is here, that we offer an interpretation of (3.5.12) based on mode-mode correlation rather than scattering, which provides a different way of thinking about anomalous heat conduction.

Consider the opposing limit of a crystal with completely random atomic motion, illustrated on the left side of Fig. 4.3.1. Although this situation does not occur in nature, it serves as an idealization from which we can deviate, in order to investigate the effects of correlation. In this limit, we consider that the motion of every atom as completely independent of the surrounding atoms, such that there are no atomic interactions to allow two atoms to influence each other's trajectory. We also consider that each atom is localized to a specific region through an onsite potential. This denies each atom the ability to transfer heat by convective diffusion. We have chosen this idealization so that no aspect of the atomic motion is correlated, and therefore if the heat flux autocorrelation

function in (3.2.15) were evaluated, the resultant thermal conductivity would be zero. In this idealized limit of random uncorrelated atomic motion, the atoms are non-interacting, while in the opposing limit of an idealized perfectly harmonic crystal, the phonons are non-interacting. By proposing this counter idealization to the perfectly harmonic crystal, we can now consider all real materials as a deviation from the uncorrelated limit, because finite correlation always exists.

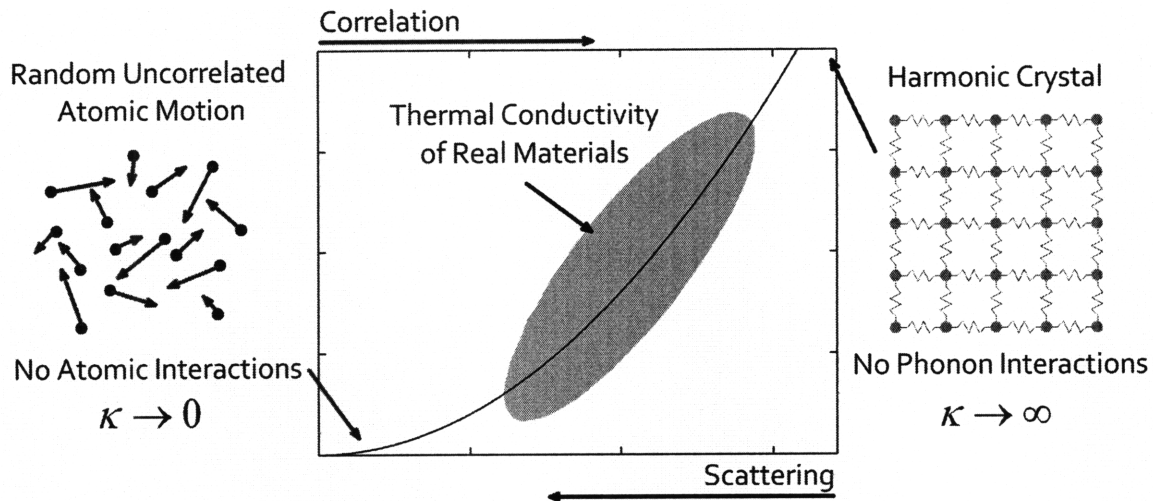


Figure 4.3.1 Diagram of scattering and correlation based paradigms for understanding heat conduction, which illustrates the two opposing idealized limits, the harmonic crystal (right) and the limit of completely uncorrelated atomic motion (left).

Starting from the limit of uncorrelated motion leads to a correlation based paradigm for thinking about thermal conduction, where the correlation in (3.2.15) now acts as a measure of departure from this limit. From this point of view we consider any form of patterned or correlated motion in the system's trajectory as a contribution to thermal conductivity. For systems where phonons are present, this perspective intuitively accounts for the possibility that scattering events can occur in an ordered sequence. To expand on this point, let us postulate the meaning of the temporal fluctuations in mode energy used to calculate the correlations in (3.5.12).

Let us reconsider the idealized perfectly harmonic crystal where the system is initialized with all the energy in one particular mode. This system will perpetually stay in the initial state unless otherwise perturbed. We would therefore observe that the singly excited mode's total energy (3.5.3) is constant. If we then add anharmonicity to the particle interactions, however, we would expect the mode's total energy to change with

time, due to interactions with other modes. We therefore interpret the mode energy fluctuations as a direct measure of the mode-mode interactions (phonon-phonon scattering events) taking place at a given instant.

For 3D bulk materials where many different scattering events are possible, we would expect the order or sequence of scattering events involving one mode k, p to be independent and unrelated to the sequence of scattering events for another mode k', p' . This would be consistent with the notion that phonon-phonon collisions are chaotic, which would imply that the cross terms ($k \neq k'$ and/or $p \neq p'$) of (3.5.12) could be neglected. This simplification would reduce (3.5.12) to (3.3.23 & 3.5.5) and would be consistent with the molecular chaos assumption [92]. The validity of this assumption is supported by the agreement with experiments that was obtained in previous studies that employed (3.3.23 & 3.5.5) for bulk materials [29, 30, 94, 96]. For 3D materials we would expect that the number of allowable phonon-phonon scattering events is large and therefore chaotic, because many choices for interactions exist. This would imply that the cross-terms in (3.5.12) are negligible. For 1D chain lattices, however, the number of allowable scattering events is significantly reduced from that of a 3D bulk material and therefore the assumption of chaotic collisions becomes questionable. From our interpretation, the cross terms of (3.5.12) account for the possibility that the sequence of phonon-phonon scattering events can be temporally correlated, which would lead to an additional contribution to heat conduction that is not captured by (3.3.23 & 3.5.5).

The idea here is that scattering events need not occur randomly, as is generally assumed in the study of heat conduction. Any form of correlation or patterning of the atomic motion can add to a material's thermal conductivity as illustrated in Fig. 4.3.1. If a system of phonons were to have sequenced or cyclically occurring phonon-phonon scattering events, it could result in positive mode-mode cross-correlation, as indicated by (3.5.12). This therefore suggests that anomalous heat conduction can occur in a system with finite (non-zero) scattering rates. If there is some underlying persistent cyclic or sequenced scattering behavior, this phenomenon could then cause cross correlations in (3.5.12) to remain correlated indefinitely, leading to infinite thermal conductivity.

Although our results only show divergence when the chain length is longer than 40 ucs, Fig. 4.2.3(d) does not indicate that the lowest mode in the LA polarization is

directly causing the divergence through its own autocorrelation. Its presence in the system may however be necessary for correlations to persist amongst other LA mode scattering processes. Mode-coupling theories suggest that low frequency, long wavelength modes behave differently than higher frequency modes, and diffuse slowly over a longer time scale [47]. We do see some consistency with this interpretation through the non-attenuating TAx and Tors modes in Figs. 4.2.1(a) and 4.2.1(c) respectively. Based on (3.5.12), however, these modes are unable to account for the strong divergence observed in Fig. 4.1.4. The persistent cross-correlations in Fig. 4.2.3 indicate that the mid-frequency LA modes may have a cyclically correlated sequence of scattering events. The fact that the autocorrelations for these modes (not shown) decay with convergent contributions to the thermal conductivity suggests that these modes have finite nonzero scattering rates. The persistent cross-correlations, however, indicate that the scattering events themselves are correlated and do not occur randomly, as is commonly thought.

4.4 Finite Length Chains

Through our use of periodic boundary conditions, our analysis of single chains up to this point has been focused on the upper limit of an infinitely long chain. Although the results led to better understanding and new insight into the mechanisms of anomalous heat conduction, we can never truly achieve infinite thermal conductivity in a real system. This is due to the finite length of real PE chains, since we would expect that the terminating end unit cells will act as a boundary scattering mechanism, which will disrupt the persistent cross-correlations discussed in the previous section. In light of this inherent limitation, it is important to determine how the finite length of a PE chain will affect the thermal conductivity. To this end we can estimate the thermal conductivity of individual PE chains using (3.3.23). Here we can introduce boundary scattering by modifying the relaxation time according to Matthiessen's rule [24, 25],

$$\frac{1}{\tau} = \frac{1}{\tau_{pp}} + \frac{v}{L} \quad (4.4.1)$$

where the net relaxation time τ of each mode is affected by the phonon-phonon scattering rate within the chain $\frac{1}{\tau_{pp}}$ as well as the finite chain length L . We can then use the autocorrelation terms of (3.5.12), where $k = k'$ and $p = p'$, to generate an estimate for the phonon-phonon scattering rate $\frac{1}{\tau_{pp}}$. Here, we can also consider two limiting cases. First we can use the autocorrelation data from a convergent 40 unit cell simulation to determine τ_{pp} for each mode. We can then use a linear interpolation scheme and a $\tau_{pp} \propto \omega^{-2}$ model to extrapolate relaxation times for other modes. We could then use this phonon-phonon scattering rate in (4.4.1) to determine the thermal conductivity according to (3.3.23). As a secondary estimate for an upper limit, we could consider incorporating the anomalous mechanism discussed in the previous sections. In this limit we can include the cross-correlation effect by taking the phonon-phonon relaxation times for LA modes with wave vectors on the intervals $[0.15, 0.25]$ and $[0.4, 0.5]$ to be infinite. This choice is based on the modes that were shown to have divergent cross-correlations in the previous section (Fig. 4.2.3). The net relaxation time, however, would still be limited by the chain's length, but as the chain length increases these modes can have an unbounded contribution to thermal conductivity. Furthermore we can include the observation that the divergent phenomenon only occurs in chains longer than 40 unit cells.

The results of this predictive scheme are shown in Fig. 4.4.1. This figure shows that boundary scattering suppresses the effects of the divergent LA modes when the chain length is shorter than ~ 1 micron. However, beyond 1 micron the effect of potentially divergent modes becomes apparent, as the thermal conductivity is unbounded and continues increasing with length. As length increases, the first limit approaches a maximum ~ 300 W/mK, because it does not incorporate the divergent mode contributions. The difference between the two curves suggests that it may be possible to detect if the correlated scattering effect actually exists in real PE chains. If thermal conductivity measurements of individual chains become possible in the future, it may

become feasible to determine whether or not the correlation effect exists in real PE chains by comparing the magnitude and trend of the thermal conductivity with chain length.

Another important feature of Fig. 4.4.1 is that we expect the thermal conductivity of individual chains to be much higher than the bulk value, regardless of whether or not the cross-correlation effect persists in real PE chains. Experiments have been used to determine the distribution of chain lengths in bulk PE and the results suggest that the chains ~ 120 unit cells (30 nm) in length are common [98]. As a result we might expect the average thermal conductivity of the chains in bulk PE to be ~ 100 W/mK, which is about 300 times greater than that of the bulk material (0.35 W/mK). This value is twice as large as the result obtained by Freeman *et al.* (~ 55 W/mK) [71]. One might expect their results to be higher than ours, because their use of the Kirkwood model [72] did not consider the CH_2 internal degrees of freedom, and therefore neglected a major portion of the optical-acoustic phonon scattering. However, Fig. 3.4.1 indicates that the Kirkwood model largely underestimates the acoustic mode group velocities, which have the strongest effect on the resultant thermal conductivity, as indicated by (3.5.12).

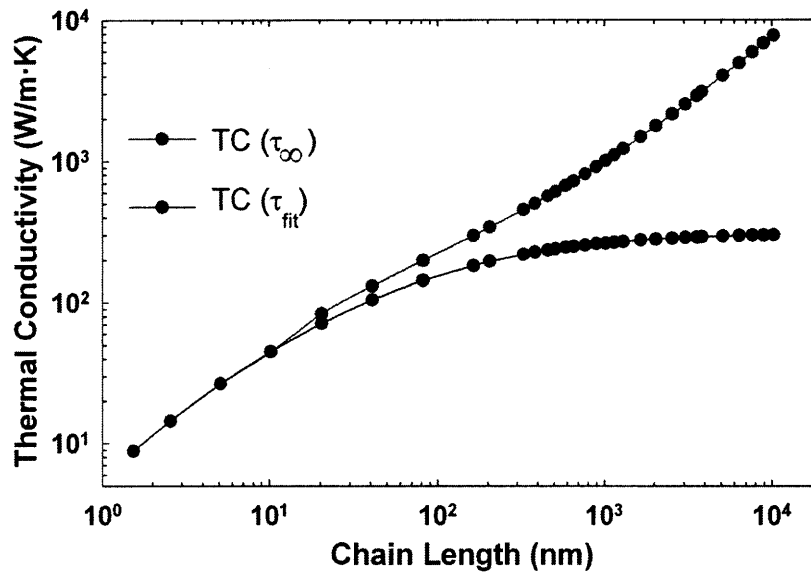


Figure 4.4.1 The predicted thermal conductivity for individual polyethylene chains as a function of chain length.

In evaluating (3.2.15) and (3.2.25) to generate the thermal conductivity results we specified the volume of an individual PE chain as the chain length multiplied by an 18 \AA^2 cross sectional area. This choice for the area was based on the bulk lattice structure

dimensions [1, 97]. It is important to note that the magnitude of the thermal conductivity for a single chain is somewhat arbitrary, because it could be rescaled by simply specifying a different cross-sectional area. In light of this, we have shown the corresponding conductance values for the individual chains in Fig. 4.4.2, where $G = \kappa \cdot A/L$. Here, the choice of area does not impact the results and we see that the maximum conductance per chain is on the order of 10^{-9} W/K and decreases with increasing chain length. For the upper limiting case where the LA cross-correlation effects are included we see that the conductance converges to a constant value $\sim 1.5 \times 10^{-10}$ W/K for chains longer than ~ 1 micron.

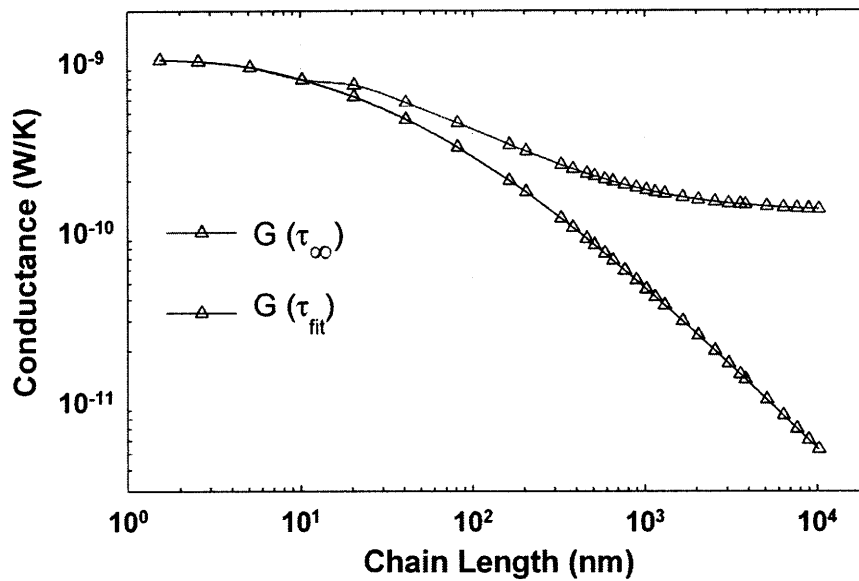


Figure 4.4.2 The predicted thermal conductance for individual polyethylene chains as a function of chain length.

Chapter 5: PE Lattice Thermal Conductivity

In the preceding chapter we showed that the thermal conductivity of individual PE chains is high and can even diverge because of correlated scattering events. We also showed that finite chains are expected to have high thermal conductivity ~ 100 W/mK, which is about 300 times larger than the bulk value 0.35 W/mK. The transition from high thermal conductivity in a single polymer chain to low thermal conductivity in bulk polymers is interesting from both a fundamental and practical stand point. Experiments on mechanically stretched bulk polyethylene report thermal conductivities as high as ~ 42 W/mK along the stretching direction [18]. Although we anticipate that the thermal contact resistance between chains will play a crucial role, anharmonic interactions between chains can lead to increased phonon-phonon scattering, which can diminish the high diverging thermal conductivity of individual chains. From a practical stand point, it is important to understand this effect for the design and structural optimization of inexpensive high thermal conductivity polymers. From a fundamental perspective, the strongly anisotropic bond chemistry (i.e. stiff covalent bonding along the chain backbone versus weak van der Waals bonding in the lateral directions) gives rise to an interesting size effect on the thermal conductivity. Here we expect the opposite trend from what is usually observed in most nanostructures, where the thermal conductivity decreases with size [24, 34]. For polymer chain lattices, we anticipate that the axial thermal conductivity can actually increase with decreasing size, as a result of reduced chain-chain anharmonic scattering.

5.1 1D-to-3D Transition

For infinitely long polymer chains, the weakly attractive van der Waals forces between chains give rise to a stable lattice structure in both 2D and 3D. This unique feature, allows for observation of a 1D-to-3D transition in phonon transport, which will cause a 1D-to-3D transition in the thermal conductivity as is conceptually illustrated in

Fig. 5.1.1. Starting from a single polyethylene chain, which has high thermal conductivity, we anticipate a transition to 2D behavior as more chains are added to form a single lattice plane (1D-to-2D transition). The 2D lattice plane should then exhibit lower thermal conductivity, as a result of anharmonic scattering induced by neighboring chains. A second transition from 2D-to-3D is also expected as additional lattice planes are stacked, leading to even more inter-chain anharmonic scattering, which should lower the thermal conductivity even further. The strongly anisotropic phonon transport in polymer chain lattices can therefore cause the axial thermal conductivity to increase with decreasing crystal size, which is the opposite trend observed in most nanostructures and bulk materials.

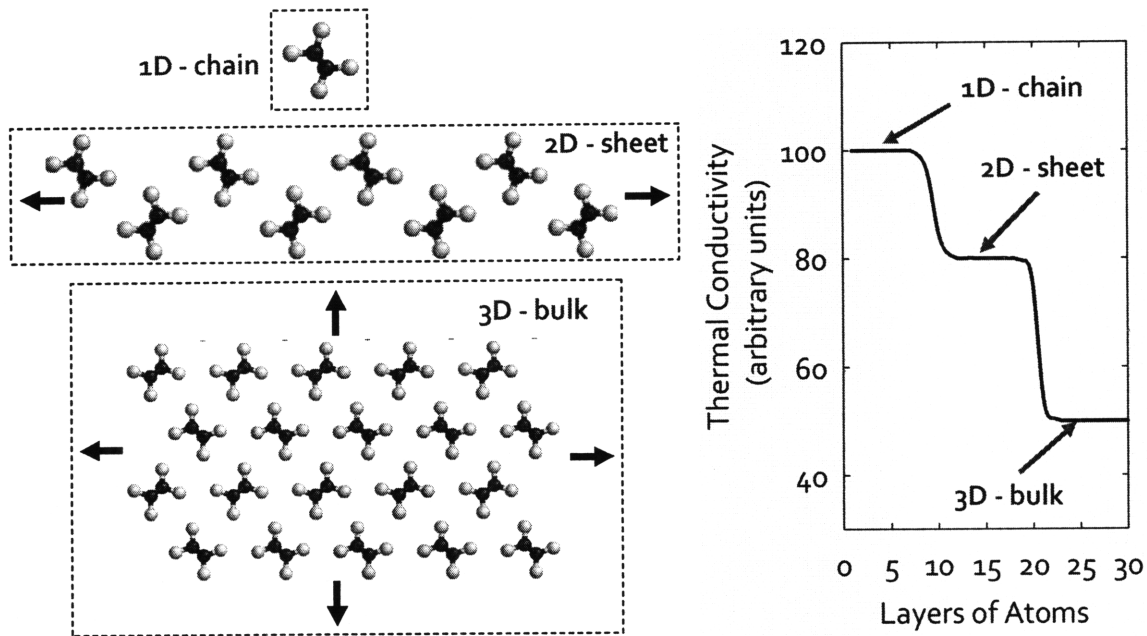


Figure 5.1.1 Conceptual illustration of the 1D-to-3D transition in the lattice structure and its anticipated effect on the lattice thermal conductivity.

The AIREBO potential is well suited for studying the proposed 1D-to-3D transition, because we require a model that can describe both intra-molecular (covalent) and inter-molecular (van der Waals) interactions. The key point is to examine the extent to which the weaker inter-molecular interactions can interfere with the much stronger intra-molecular covalent forces, in order to induce phonon-phonon scattering and reduce the thermal conductivity.

Figure 5.1.2 shows how the decay of the HFAC function changes for the 1D chain, 2D sheet and 3D bulk cases, which are bolded in Table 3.6.1. Figure 5.1.2a shows that the single chain has the longest decay time. When a second chain is added the decay rate increases significantly, leading to lower thermal conductivity. This indicates that the transition from 1D to 2D behavior is sharp, suggesting that chain-chain phonon-phonon scattering is substantial with only two chains present. Figure 5.1.2b shows a more extended view of the HFAC functions. This plot shows that the 1D case has a long tail, which can even lead to divergent thermal conductivity, while the 2D and 3D cases decay more rapidly.

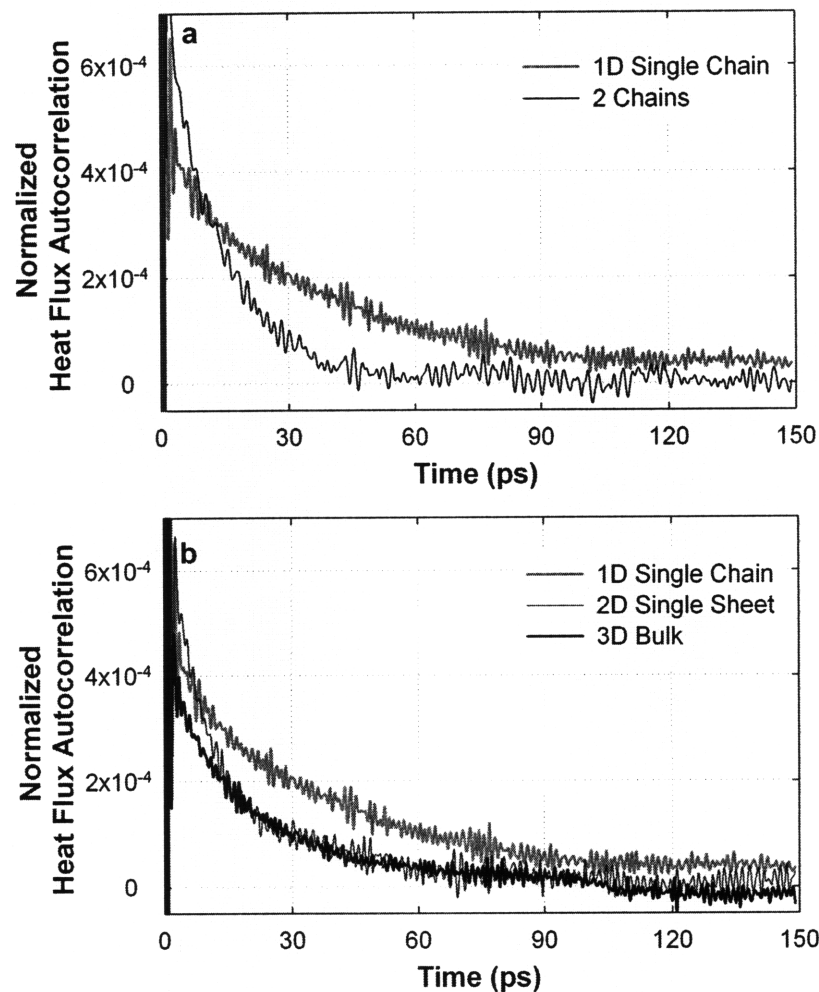


Figure 5.1.2 Normalized heat flux autocorrelation (HFAC) functions vs. time. **a** shows the average HFAC function for 10 independent simulations of the bolded 1D, 2D and 3D cases in Table 3.6.1, as well as the 2nd case with two chains. **b** shows the long time behavior of the HFAC functions for the bolded 1D, 2D and 3D cases in Table 3.6.1. In both **a** and **b** the data has been smoothed over 1 ps intervals to filter out high frequency oscillations for a clearer representation of the decaying features.

The results in Fig. 5.1.3 show the thermal conductivity values obtained for all 12 cases described in Table 3.6.1. This figure shows the full 1D-2D and 2D-3D transitions, with respect to the number of chains or layers in the corresponding dimension. Numerical integration of the HFAC functions after several nanoseconds exhibited oscillations due to cumulative noise associated with the longitudinal acoustic phonons, which are the most dominant heat carriers. As a result, the (infinite) integration limit in (3.2.15), was truncated to 500 ps, which sufficiently captures the autocorrelation decay for all cases, as shown in Fig. 5.1.2b. Each point in Fig. 5.1.3 therefore represents the average thermal conductivity of all 10 independent simulations, while the error bars show the standard deviation. Despite the spread in the results, the 1D-to-3D transition and overall trend of decreasing thermal conductivity with increasing size is nonetheless apparent. The results of Fig. 5.1.3 also show that the transition from 1D-2D is sharper than the transition from 2D-3D. The single chain thermal conductivity is large, as discussed in chapter 4. However, when two chains are allowed to interact the thermal conductivity decreases by $\sim 40\%$, which is also evident from Fig. 5.1.2a. As more chains are added to form a single layer of chains the thermal conductivity does not change as drastically. Once periodic boundary conditions are employed in 2D, the transition to 3D is less abrupt, and the thermal conductivity decreases from the planar limit by another $\sim 30\%$. Once 5 layers of chains have been stacked, Fig. 5.1.3 shows that the thermal conductivity is quite close to that of the bulk value predicted when periodic boundaries are employed in all three dimensions.

Starting from the single chain limit, as more molecular chains are added to the simulation domain, lattice waves begin propagating in the perpendicular directions and at intermediate angles in between. These phonons contribute to the axial thermal conductivity by carrying heat, but they also detract from the high thermal conductivity of each individual chain, by scattering the most efficient heat carrying phonons, which propagate along each chain's carbon backbone. The vital characteristic that allows for the 1D-to-3D transition shown in Fig. 5.1.3, is that these phonons detract from the axial heat conduction more than they can contribute, thus reducing the net thermal conductivity.

Another interesting feature of the results in Fig. 5.1.3, is that the bulk value predicted by our simulations is in good agreement with the thermal conductivity of stretched samples of bulk polyethylene [18]. In the most highly stretched samples, the authors report that single crystalline needle structures were obtained [18]. The correspondence with our simulation results indicates that anharmonic scattering between chains has a stronger effect on reducing the thermal conductivity than the thermal resistance at grain boundaries between crystals. Our results show that the anharmonic scattering induced by weak van der Waals forces can cause significant attenuation of modes propagating along the stiff covalently bonded polymer chain backbone. This provides important quantitative insight into heat conduction in polymer lattices, which will be necessary for designing and manufacturing low-cost high thermal conductivity polymers.

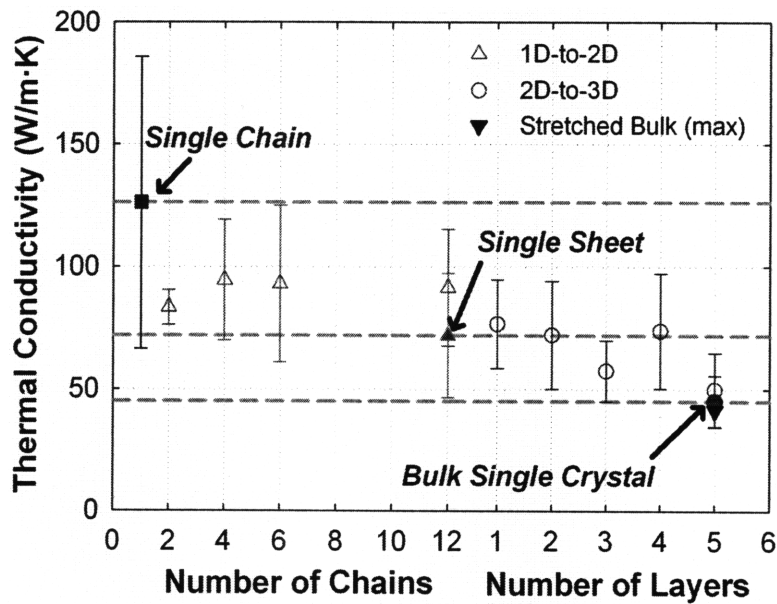


Figure 5.1.3 1D-to-3D thermal conductivity results from the Green-Kubo analysis, showing the 1D-2D (left) and 2D-3D (right) transitions along with the maximum thermal conductivity reported in experiments on mechanically stretched bulk polyethylene. The left portion of the horizontal axis is given in the number of molecular chains for the 1D-2D transition, while the right portion of the horizontal axis is given in terms of the number of 2D layers being stacked for the 2D-3D transition. Dashed lines indicate the values obtained for the 1D single chain limit, the 2D sheet limit and the 3D bulk crystal limit, which show the increasing trend with decreased dimensionality.

5.2 1D-to-2D: Anharmonicity vs. Conductance

In the previous section we observed the expected 1D-to-2D and 2D-to-3D transitions and increasing trend for the thermal conductivity with decreased dimensionality. One interesting aspect of the results is that the 1D-to-2D transition is sharp, and the behavior observed with only two chains present was very similar to that of the 2D infinite planar sheet. In this section we probe this transition in greater detail by considering a long 200 unit cell chain with periodic boundary conditions applied along its length. We then consider how the thermal conductivity of the long single chain (chain 1) is affected by the growing presence of a second chain of finite length (chain 2), with terminated ends $\text{CH}_3\text{-(CH}_2\text{-CH}_2\text{)}_n\text{-CH}_3$. As we increase the value of n for chain 2 we would expect to approach the thermal conductivity obtained for two chains, as discussed in the previous sections. The objective of studying this system is to determine how strong the effect of anharmonicity is, and whether or not its impact on neighboring chains is gradual or immediate. Additionally this system allows us to study the conductance between two neighboring chains, based on (3.2.40). Inspection of (3.2.40) suggests that the conductance between chains should increase with n^2 , since it is proportional to the square of the energy exchanged between chains as a result of the chain-chain van der Waals forces. Determining the conductance between chains will allow for further development of a thermal resistance model which can be used to understand the dominant heat conduction mechanisms.

The following results are based on 10 independent simulations for each of the two chain systems previously described, which consist of (chain 1) a long 200 unit cell chain that extends to the domain's periodic boundaries, and (chain 2) a shorter neighboring chain that has terminated ends $\text{CH}_3\text{-(CH}_2\text{-CH}_2\text{)}_n\text{-CH}_3$. The secondary shorter chain was initialized at its equilibrium position according to the bulk lattice structure, and its length was increased from 0 unit cells (only chain 1) to 190 unit cells. All simulations were run at the quantum corrected room temperature and were initialized with random velocities in the same manner as all simulations discussed previously. Using this setup, we computed the thermal conductivity of the longer 200 unit cell chain as the shorter finite chain's length was increased. For this computation, we omitted contributions to the heat flux that

arose from the van der Waals forces between chains (see equation (3.2.25)). It is in this manner that we isolated the effect of anharmonicity, because the resulting heat flux autocorrelation function was restricted to the same intra-molecular forces that are used in the single chain calculations and no intermolecular forces were included. Thus the neighboring chain only affects the results through its ability to alter the trajectory of chain 1. The chain-chain van der Waals forces that give rise to this effect on the trajectory are not included in the calculation of the temporally varying heat flux (3.2.25), thereby separating the effect of anharmonicity from the chain-chain conductance. These chain-chain van der Waals forces, however, are used to compute the chain-chain conductance (equation (3.2.40) & (3.2.41)).

Figure 5.2.1 shows how the thermal conductivity of chain 1 decreases from the increased length of chain 2. Here we see that the full onset of anharmonicity occurs at short chain lengths ~ 10 unit cells. Conceptually we can think of the presence of chain 2 as a temporally varying perturbation to the trajectory of chain 1. This perturbation serves to disrupt the correlated motion of the atoms in chain 1 and subsequently causes the heat flux autocorrelation to decay more quickly. It is interesting to note that the effect is immediate and once chain 2 is large enough to cause a significant disruption in the correlated atomic motion of chain 1, the thermal conductivity decreases by $\sim 50\%$. Figure 5.2.1 shows that beyond 10 unit cells in length, the continued increase in length of chain 2 does not cause a continuous decrease in thermal conductivity for chain 1.

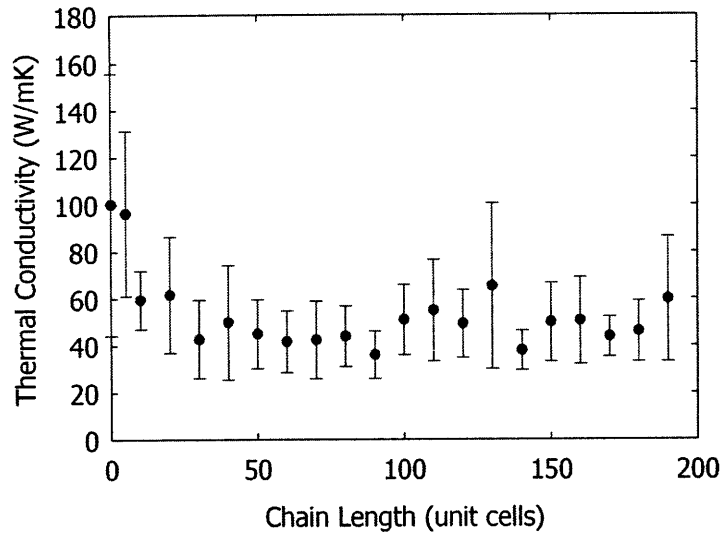


Figure 5.2.1 Thermal conductivity of chain 1 in the presence of chain 2, whose length is increased from 0 unit cells (only chain 1 present) to 190 unit cells.

Figure 5.2.2 shows how the normalized heat flux autocorrelation (HFAC) changes as the length of chain 2 is increased. Similar to the results in chapter 4, the HFAC functions exhibited strong oscillations ~ 50 THz that are symmetric about zero and thus do not contribute to the heat conduction. The HFAC functions in Fig. 5.2.2 were obtained by averaging over the 10 independent simulations, and the curves consist of smoothed local average values (2.5 ps intervals) in order to highlight the decaying features. Here we can see that the presence of chain 2 serves to disrupt the correlated decay of chain 1 and leads to stronger oscillations, which detract from the Green-Kubo thermal conductivity integral (3.2.15).

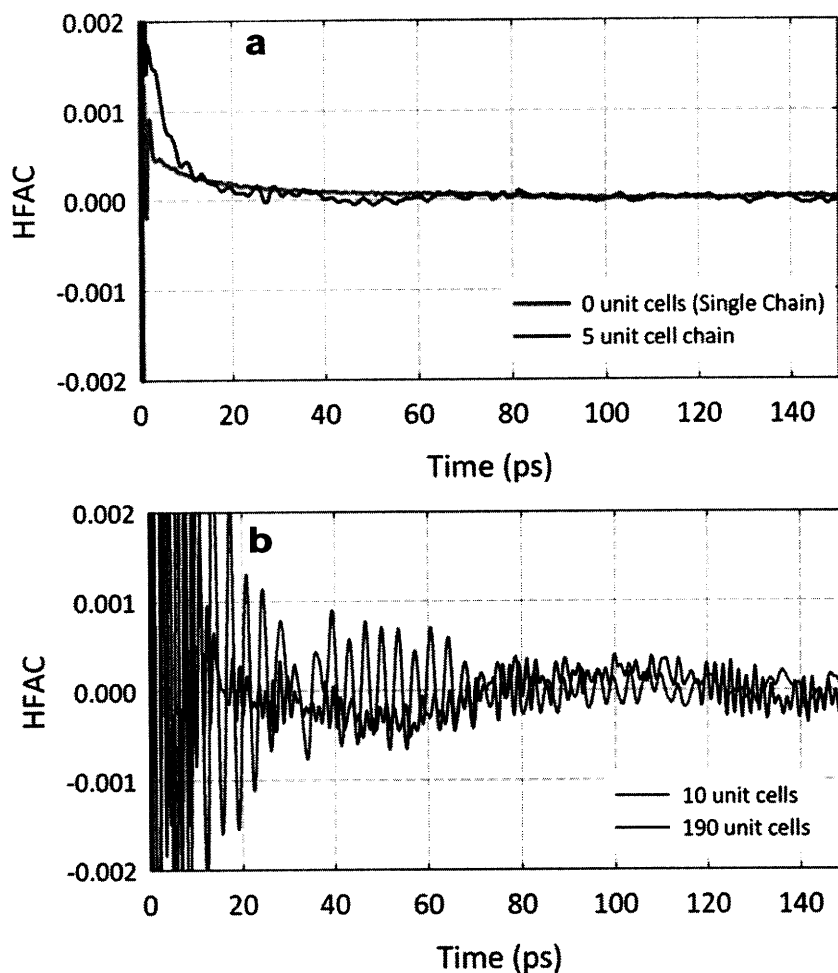


Figure 5.2.2 Normalized heat flux autocorrelation functions for chain 1 **a**, when chain 2 is 0 and 5 unit cells long and **b**, when chain 2 is 10 and 190 unit cells long. The values have been smoothed using the same procedure for all curves and are based on local averages over 2.5 ps intervals.

In addition to decreasing the longer chain's thermal conductivity, the presence of the second chain adds a new parallel channel for heat conduction. This chain-chain conductance serves to reduce the overall thermal resistance, thereby increasing the overall thermal conductivity of the two chain composite structure. Studying the interplay between these two competing effects of anharmonicity and conductance allows for better understanding of the dominant mechanism for thermal transport in mechanically stretched bulk PE. Figure 5.2.3 shows the conductance values for the cases considered in Fig. 5.2.1, based on (3.2.40). This plot shows that the conductance increases as expected, and is proportional to the square of the number of interacting atoms and length of chain 2.

It is also important to note that the magnitude of the conductance $\sim 10^{-10}$ W/K is comparable to other conductance values obtained for the conductance between nanoparticles, which range from 10^{-14} – 10^{-9} W/K [91]. Figure 5.2.4 shows an example normalized energy exchange autocorrelation (EEAC) function. Here we see the same strong 50 THz oscillation observed in HFAC functions. As a result Fig. 5.2.4 also shows the same data when smoothed using local average values (2.5 ps intervals) in order to highlight its decaying features. Here we can see that unlike the HFAC which decays over hundreds of picoseconds, the EEAC decays much more rapidly in less than one picosecond. This short decay is expected since the coupling between the two chains is weak, as compared to the more dominant covalent intramolecular interactions.

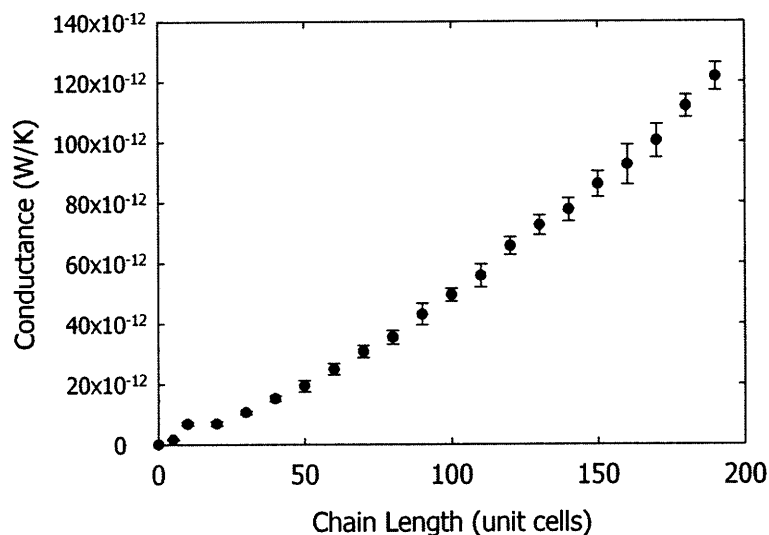


Figure 5.2.3 Chain-chain conductance between chain 1 and chain 2 as a function of the length of chain 2. Error bars indicate the standard deviation obtained from the 10 independent simulations

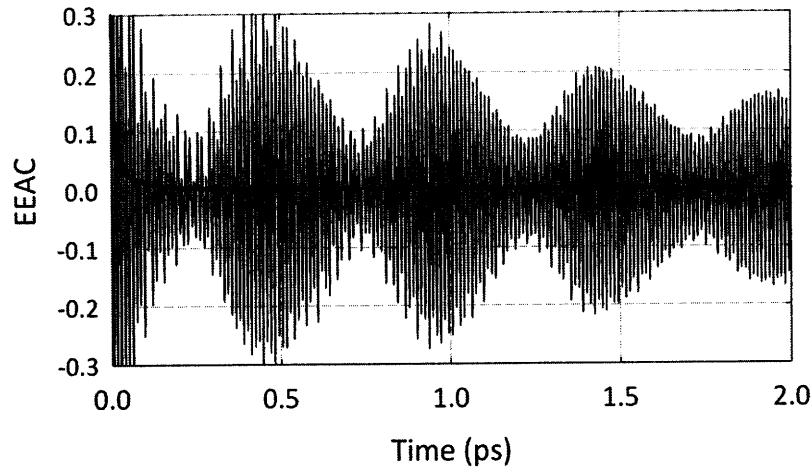


Figure 5.2.4 Normalized energy exchange autocorrelation (EEAC) function used to compute the conductance between chain 1 and chain 2. The (red line) values have been smoothed over 2.5 ps intervals to highlight the decaying features of the actual EEAC, which exhibits large oscillations ~ 50 THz.

One simple way to incorporate the calculated conductance into a thermal resistance model would be to treat each chain as an infinite 1D fin. The notion that individual chains can be treated as fins is based on the temporal temperature fluctuations. At a given instant we would expect that the atoms in one chain may have higher kinetic energy while other atoms in the same vicinity, that comprise the neighboring chains, may have less kinetic energy. The atoms with higher energy can then conduct that energy to surrounding atoms through the chain-chain conductance. This process of dissipation resembles that of macroscopic convection and can therefore be used in accordance with Newton's law of cooling $Q = hA_s\Delta T$. In the proposed fin model we treat each neighboring chain as a means of heat removal, by imagining each chain as a fin with a rectangular cross section set by the bulk lattice constants. We can then calculate a heat transfer coefficient by matching to the heat transfer obtained with the chain-chain conductance $G\Delta T = hA_s\Delta T$, where h is the heat transfer coefficient and $A_s = 1.471 \times 10^{17} \text{ \AA}^2$ based on the bulk lattice structure. This leads to an overall fin resistance of $1.72 \times 10^9 \text{ K/W}$, where we have used the average thermal conductivity in Fig. 5.2.1 $\sim 47 \text{ W/mK}$ as the individual chain thermal conductivity. This is the average value we would expect for two completely overlapping 200 unit cell chains. With this estimate for the resistance we can then proceed to calculate the effective thermal conductivity of two neighboring 200 unit cell chains, where they are considered as thermal resistors in parallel. Here we

find that the effective thermal conductivity of two neighboring chains is ~ 82 W/mK, which is in good agreement with the two chain result in Fig. 5.1.3.

Here we can see that even though the effect of anharmonicity is strong and reduces the thermal conductivity of each individual chain to ~ 47 W/mK, the chain-chain conductance counter balances the effect and enhances the composite structure conductivity by almost 40 W/mK. It is however interesting to note that the effect of the anharmonicity is immediate and reduces the individual chain thermal conductivity with only a short overlapping region. The conductance, on the other hand, increases more gradually and would only be able to compensate for the anharmonic reduction when the overlapping regions are large.

Chapter 6: Conclusions and Future Directions

6.1 Conclusions

Experiments have demonstrated that the thermal conductivity of bulk polymers can be increased dramatically by mechanical stretching, as a result of increased polymer chain alignment [18, 19, 99]. In order to determine the range of possible applications for such materials it is important to first understand and quantify the fundamental upper limits. In this thesis we have derived and implemented several MD trajectory analysis techniques that revealed important information about the phonon transport in individual polyethylene chains as well as PE chain lattices. Intuitively we know that the highest possible thermal conductivity that can be achieved in polymer chain based materials is the limit of an infinitely long single chain. We have chosen PE because it is the simplest and most widely used polymer. In this respect, a single PE chain in the zig-zag conformation bears strong resemblance to the 1D nonlinear chain of oscillators studied by Fermi, Pasta and Ulam in the 1950's, which led to the discovery that nonlinear chains of oscillators can be non-ergodic [40]. This surprising result implied infinite thermal conductivity and has led to decades of discussion about anomalous heat conduction in low-dimensional systems.

In this thesis we studied phonon transport in individual PE chains and observed divergent Green-Kubo integrals, which suggests that an infinitely long PE chain can have infinite thermal conductivity. We then proceeded to conduct more detailed analysis and found that the divergent effect could be suppressed by the addition of heavier isotopes, which indicated that the divergent phenomenon was not a result of unphysical numerical artifacts. Modal analysis showed that the lowest frequency modes in the system do not fully attenuate, which is often explained by hydrodynamic mode coupling theory [47]. Further analysis, however, showed that this behavior was exhibited by all simulations, regardless of whether or not the thermal conductivity diverged. Furthermore, when the contribution of these modes to the thermal conductivity was evaluated, they were unable

to explain the rate of divergence in the Green-Kubo integrals. Subsequent analysis revealed that the divergence was due to persistent cross-correlation amongst certain LA modes. This observation led to a new explanation for the divergence and suggested that all phonons do experience phonon-phonon scattering, yet some modes encounter scattering events in a correlated pattern. This notion violates one of the most widely used simplifications of the Boltzmann equation, which is based on the assumption of molecular chaos [92]. This new evidence and explanation subsequently led to a new perspective for thinking about lattice heat conduction. Here we proposed an alternative paradigm to the traditional viewpoint which is based on working towards the most accurate account of scattering interactions. Our new paradigm suggests that more efficient heat conduction can be thought of as arising from increased correlation in the atomic motion.

Using the results obtained for individual chains with periodic boundary conditions, we also predicted the thermal conductivity and conductance of finite length chains. These calculations indicated that the thermal conductivity may converge to ~ 300 W/mK for micron long chains, if the divergent phenomenon does not persist. On the other hand, if the divergent phenomenon does persist, these calculations showed that the thermal conductivity is unbounded and the conductance converges to a constant $\sim 1.5 \times 10^{10}$ W/K. In pursuit of understanding phonon transport in stretched polymers, we also studied how the thermal conductivity of a single chain is impacted by the presence of additional chains, which can enhance phonon-phonon scattering through van der Waals interactions. To this end, we studied how the thermal conductivity decreases from 1D-to-2D behavior in a planar sheet and how the thermal conductivity is further decreased by stacking planar sheets to build up to a 3D lattice, which gave rise to a second transition from 2D-to-3D behavior. These results showed that the full transition from 1D-to-2D occurs with only 2 chains present. The scattering induced by the second chain prevents the thermal conductivity from diverging and also reduces the single chain conductivity by $\sim 40\%$. The transition from 2D-to-3D behavior, on the other hand, is more gradual and once 5 layers of planar sheets have been stacked, we observed convergence to the bulk lattice behavior. Our results for the bulk lattice thermal conductivity also agree well with

the highest value obtained for stretched samples of bulk PE, which were reported to contain thin crystal needle like structures [18].

Lastly, we investigated the 1D-to-2D transition in greater detail for better understanding of the interplay between the effect of anharmonicity and conductance. This was accomplished by studying a system of 2 chains. Chain 1 was 200 unit cells long and extended to the periodic boundaries, while chain 2 was shorter and had terminated ends. Using this system we studied the rate at which the thermal conductivity of chain 1 decreased as a result of increasing the length of chain 2. These simulations indicated that the effect of anharmonicity was immediate and that a 10 unit cell length for chain 2 had the same impact on the thermal conductivity of chain 1 as a 190 unit cell chain. This reduction in thermal conductivity of $\sim 50\%$ was counterbalanced by the fact that the presence of the second chain opens a new path for heat conduction as a parallel resistance. This effect was studied by computing the chain-chain conductance. These results showed that the chain-chain conductance followed the expected trend and increased as the square of the chain 2 length. These results were then incorporated into a simple 1D fin heat conduction model and showed that the two chain thermal conductivity results can be explained by considering each chain as a separate thermal resistor in parallel. This self consistency in our calculations further confirms the fidelity of our results. Furthermore the quantitative results and increased understanding gained from the various MD simulations conducted in this thesis can provide additional insight into the design and structural optimization of polymer chain-based heat transfer materials.

6.2 Future Directions

Although several aspects of the relevant physics have been explored in this thesis, many issues of concern and interest remain for future study. For example, a future investigation should address more thoroughly the most appropriate definition of temperature. Here, we have shown results for simulations at room temperature based on the quantum corrected definition discussed in chapter 3. This choice was motivated by the large spectrum of phonon frequencies in the PE chains (0.01 - 90 THz), which lead to

arguments surrounding the possible misrepresentation of normal mode amplitudes if the equipartition-based definition was used. Other simulations, which were not discussed were run at room temperature, using the equipartition-based definition and resulted in even higher convergent thermal conductivity $\sim 1,000$ W/mK and a stronger divergence $> 10,000$ W/mK within 5 ns. The results discussed in chapters 4 and 5, which were based on the quantum corrected temperature definition, were emphasized because they serve as a more conservative estimate. Future investigations should probe the behavior of single chains and chain lattices at room temperature based on the equipartition definition, along with detailed modal analysis to cross check the magnitude of the thermal conductivity and to verify the proposed cross-correlation mechanisms. Furthermore, additional simulations should be used to study the temperature dependence of the thermal conductivity, which may assist in establishing the correct definition of temperature.

Another area for future pursuit could involve studying the thermal conductivity dependence on crystallinity. Experiments on stretched polymers often report X-ray diffraction measurements as a means of estimating the degree of crystallization in the samples. Although our conductance calculations suggest that the chain-chain conductance can be large and plays an important role in the lattice heat conduction, we would still expect that chain-chain entanglement and disorder could disrupt the heat conduction pathways and reduce the thermal conductivity. It would be interesting if future studies could establish how exactly how the degree of entanglement impacts the thermal conductivity.

Future investigations could also explore the properties of related polymer molecules such as Teflon and polyacetylene. Teflon, for example, has the same structure as PE except that the hydrogen atoms are replaced by heavier fluorine atoms. It would be interesting to investigate whether or not the divergent phenomenon observed in single chains persists in Teflon as well. If so, it could possibly lead to a more general understanding and also a different range of applications, since Teflon is more stable at higher temperatures. Additionally, it may be interesting to study polyacetylene, which is a zig-zag hydrocarbon chain, where every other carbon is only bonded to one hydrogen atom instead of two as is the case with PE. The absence of some of the hydrogen atoms leads to stronger double bonds between adjacent carbon atoms. With this increased

stiffness along the carbon backbone, we might expect even higher phonon group velocities and therefore even higher thermal conductivity. It would also be interesting to study whether or not the divergent phenomenon persists in polyacetylene molecules as well. These future directions along with the foundational knowledge obtained in this thesis could add important insight into the future design optimization and large-scale manufacturing of cheap high thermal conductivity polymers.

References

- [1] L. H. Sperling, *Introduction to Physical Polymer Science*. 4 ed. 2006, Bethelhem Pennsylvania: John Wiley & Sons Inc. 249.
- [2] H. S. Tekce, D. Kumlutas, and I. H. Tavman, Composites Effect of Particle Shape on Thermal Conductivity of Copper Reinforced Polymer Journal of Reinforced Plastics and Composites, **26**, 113 (2007).
- [3] Y. S. Song and J. R. Youn, Evaluation of effective thermal conductivity for carbon nanotube/polymer composites using control volume finite element method Carbon, **44**, 710–717 (2006).
- [4] C.-W. Nan *et al.*, Interface effect on thermal conductivity of carbon nanotube composites Appl. Phys. Lett., **85**(16), 3549 (2004).
- [5] M. Moniruzzaman and K. I. Winey, Polymer Nanocomposites Containing Carbon Nanotubes Macromolecules, **39**, 5194-5205 (2006).
- [6] A. Bagchi and S. Nomura, On the effective thermal conductivity of carbon nanotube reinforced polymer composites Composites Science and Technology, **66**, 1703-1712 (2006).
- [7] S. Berber, Y.-K. Kwon, and D. Tomanek, Unusually High Thermal Conductivity of Carbon Nanotubes Physical Review Letters, **84**(20), 4613-4616 (2000).
- [8] J. Che, T. Cagin, and W. A. G. III, Thermal conductivity of carbon nanotubes Nanotechnology, **11**, 65-69 (2000).
- [9] J. R. Lukes and H. Zhong, Thermal Conductivity of Individual Single-Wall Carbon Nanotubes Journal of Heat Transfer, **129**(6), 705-716 (2007).
- [10] J. F. Moreland, J. B. Freund, and G. Chen, The Disparate Thermal Conductivity of Carbon Nanotubes and Diamond Nanowires Studied By Atomistic Simulation Microscale Thermophysical Engineering, **8**, 61-69 (2004).
- [11] M. A. Osman and D. Srivastava, Temperature dependence of the thermal conductivity of single-wall carbon nanotubes Nanotechnology, **12**, 21-24 (2000).
- [12] Z. Yao *et al.*, Thermal conduction of carbon nanotubes using molecular dynamics Phys. Rev. B, **71**, 085417 (2005).
- [13] W. Zhang *et al.*, Chirality dependence of the thermal conductivity of carbon nanotubes Nanotechnology, **15**, 936-939 (2004).
- [14] M. Fujii *et al.*, Measuring the Thermal Conductivity of a Single Carbon Nanotube Phys. Rev. Lett., **95**, 065502 (2005).
- [15] P. Kim *et al.*, Thermal Transport Measurements of Individual Multiwalled Nanotubes Phys. Rev. Lett., **87**(21), 215502 (2001).
- [16] D. J. Yang *et al.*, Thermal conductivity of multiwalled carbon nanotubes Phys. Rev. B, **66**, 165440 (2002).
- [17] C. Yu *et al.*, Thermal Conductance and Thermopower of an Individual Single-Wall Carbon Nanotube Nano Lett., **5**(9), 1842-1846 (2005).
- [18] C. L. Choy *et al.*, Elastic Modulus and Thermal Conductivity of Ultradrawn Polyethylene Journal of Polymer Science: Part B: Polymer Physics, **37**, 3359-3367 (1999).

- [19] D. B. Mergenthaler *et al.*, Thermal Conductivity in Ultraoriented Polyethylene Macromolecules, **25**, 3500-3502 (1992).
- [20] N. W. Ashcroft and N. D. Mermin, *Solid State Physics*. 1976: Brooks Cole. 848.
- [21] P. L. Hagelstein, S. D. Senturia, and T. P. Orlando, *Introductory Applied Quantum and Statistical Mechanics*. 2004, New Jersey: John Wiley & Sons. 785.
- [22] N. Pinna, M. Antonietti, and M. Niederberger, A novel nonaqueous route to V₂O₃ and Nb₂O₅ nanocrystals Colloids and Surfaces A: Physicochem. Eng. Aspects, **250**, 211-213 (2004).
- [23] M. T. Dove, *Introduction to Lattice Dynamics*. 1993: Cambridge University Press. 258.
- [24] G. Chen, *Nanoscale Energy Transport and Conversion: A Parallel Treatment of Electrons, Molecules, Phonons, and Photons*. 2005: Oxford University Press. 560.
- [25] G. P. Srivastava, *Physics of Phonons*. 1990, New York: Adam Hilger. 421.
- [26] Z. Rieder, J. L. Lebowitz, and E. Lieb, Properties of a Harmonic Crystal in a Stationary Nonequilibrium State J. Math. Phys., **8**, 1073 (1967).
- [27] R. Peierls, Ann. Physik, **3**, 1055 (1929).
- [28] D. A. Broido *et al.*, Intrinsic lattice thermal conductivity of semiconductors from first principles Appl. Phys. Lett., **91**, 231922 (2007).
- [29] A. Henry and G. Chen, Spectral Phonon Transport Properties of Silicon Based on Molecular Dynamics Simulations and Lattice Dynamics Journal of Computational and Theoretical Nanoscience, **5**, 141-152 (2008).
- [30] A. McGaughey and M. Kaviani, Quantitative validation of the Boltzmann transport equation phonon thermal conductivity model under the single-mode relaxation time approximation Phys. Rev. B, **69**, 094303-094315 (2004).
- [31] C. Dames, Thermal properties of nanowires and nanotubes : modeling and experiments, MIT, **Ph.D.** (2006).
- [32] C. J. Glassbrenner and G. A. Slack, Thermal conductivity of silicon and germanium from 3K to the melting point Phys. Rev., **134**(4A), 1058-1069 (1964).
- [33] A. Khituna, J. Liu, and K. L. Wang, On the modeling of lattice thermal conductivity in semiconductor quantum dot superlattices Appl. Phys. Lett., **84**(10), 1762-1764 (2004).
- [34] D. Li *et al.*, Thermal conductivity of individual silicon nanowires Appl. Phys. Lett., **83**(14), 2934-2936 (2003).
- [35] Y. S. Ju and K. E. Goodson, Phonon scattering in silicon films with thickness of order 100 nm Appl. Phys. Lett., **74**(20), 3005-3007 (1999).
- [36] M. S. Dresselhaus *et al.*, New Directions for Low-Dimensional Thermoelectric Materials Adv. Mater., **19**, 1-12 (2007).
- [37] B. Poudel *et al.*, High-Thermoelectric Performance of Nanostructured Bismuth Antimony Telluride Bulk Alloys Science, **320**, 634-638 (2008).
- [38] G. P. Berman and F. M. Izraileva, The Fermi–Pasta–Ulam problem: Fifty years of progress Chaos, **15**, 015104 (2005).
- [39] D. K. Campbell, P. Rosenau, and G. M. Zaslavsky, Introduction: The Fermi–Pasta–Ulam problem—The first fifty years Chaos, **15**, 015101 (2005).
- [40] E. Fermi, J. Pasta, and S. Ulam, Studies of Nonlinear Problems. I, (1955).

- [41] R. Bourbonnais and R. Maynard, Energy Transport in One- and Two- Dimensional Anharmonic Lattices with Isotopic Disorder Phys. Rev. Letters, **64**(12), 1397-1400 (1989).
- [42] G. Casati *et al.*, One-Dimensional Classical Many-Body System Having a Normal Thermal Conductivity Phys. Rev. Lett., **52**(21), 1861-1864 (1984).
- [43] A. Dhar, Comment on “Can Disorder Induce a Finite Thermal Conductivity in 1D Lattices?” Phys. Rev. Lett., **87**(6), 069401 (2001).
- [44] C. Giardina *et al.*, Finite Thermal Conductivity in 1D Lattices Phys. Rev. Lett. , **84**, 2144-2147 (1999).
- [45] T. Hatano, Heat conduction in the diatomic Toda lattice revisited Phys. Rev. E, **59**(1), R1-R4 (1999).
- [46] S. Lepri, R. Livi, and A. Politi, Heat Conduction in Chains of Nonlinear Oscillators Phys. Rev. Lett., **78**(10), 1896-1899 (1997).
- [47] S. Lepri, R. Livi, and A. Politi, On the anomalous thermal conductivity of one-dimensional lattices Europhys. Lett., **43**(3), 271-276 (1998).
- [48] S. Lepri, R. Livi, and A. Politi, Thermal conduction in classical low-dimensional lattices Physics Reports, **377**, 1-80 (2003).
- [49] B. Li and J. Wang, Anomalous Heat Conduction and Anomalous Diffusion in One-Dimensional Systems Phys. Rev. Lett., **91**(4), 044301 (2003).
- [50] B. Li, L. Wang, and B. Hu, Finite Thermal Conductivity in 1D Models Having Zero Lyapunov Exponents Phys. Rev. Lett., **88**(22), 223901 (2002).
- [51] B. Li, H. Zhao, and B. Hu, Can Disorder Induce a Finite Thermal Conductivity in 1D Lattices? Phys. Rev. Lett., **81**(1), 63-66 (2001).
- [52] N. Li, P. Tong, and B. Li, Effective phonons in anharmonic lattices: Anomalous vs. normal heat conduction Europhys. Lett., **75**(1), 49-55 (2006).
- [53] M. Mareschal and A. Amellal, Thermal conductivity in a one-dimensional Lennard Jones chain by molecular dynamics Phys. Rev. A, **37**(6), 2189-2196 (1988).
- [54] O. Narayan and S. Ramaswamy, Anomalous Heat Conduction in One-Dimensional Momentum-Conserving Systems Phys. Rev. Lett., **89**(20), 200601 (2002).
- [55] T. Prosen and D. K. Campbell, Momentum Conservation Implies Anomalous Energy Transport in 1D Classical Lattices Phys. Rev. Lett., **84**(13), 2857-2860 (2000).
- [56] T. Prosen and D. K. Campbell, Normal and anomalous heat transport in one-dimensional classical lattices Chaos, **15**, 015117 (2005).
- [57] A. V. Savin and O. V. Gendelman, Heat conduction in one-dimensional lattices with on-site potential Phys. Rev. E, **67**, 041205 (2003).
- [58] A. V. Savin *et al.*, Nonlinear dynamics of zigzag molecular chains Physics - Uspekhi, **42**(3), 245-260 (1999).
- [59] A. V. Savin, G. P. Tsironis, and A. V. Zolotaryuk, Heat Conduction in One-Dimensional Systems with Hard-Point Interparticle Interactions Phys. Rev. Lett., **88**(15), 154301 (2002).
- [60] H. Shiba and N. Ito, Anomalous Heat Conduction in Three-Dimensional Nonlinear Lattices J. of the Physical Society of Japan, **77**(5), 054006 (2008).
- [61] J.-S. Wang and B. Li, Intriguing Heat Conduction of a Chain with Transverse Motions Phys. Rev. Lett., **92**(7), 074302 (2004).

- [62] J.-S. Wang and B. Li, Mode-coupling theory and molecular dynamics simulation for heat conduction in a chain with transverse motions Phys. Rev. E, **70**, 021204 (2004).
- [63] N. J. Zabusky and M. D. Kruskal, Interaction of “solitons” in a collisionless plasma and the recurrence of initial states,” Phys. Rev. Lett., **15**, 240-243 (1965).
- [64] B. V. Chirikov, Resonance processes in magnetic traps J. Nucl. Energy, Part C, **1**, 253-260 (1960).
- [65] F. M. Izrailev and B. V. Chirikov, Statistical Properties of a Nonlinear String Sov. Phys. Dokl. , **11**, 30 (1966).
- [66] F. M. Izrailev, A. I. Khisamutdinov, and B. V. Chirikov, Numerical experiments with a chain of coupled anharmonic oscillators, Institute of Nuclear Physics, (1968).
- [67] T. Prosen and M. Robnik, Energy transport and detailed verification of Fourier heat law in a chain of colliding oscillators J. Phys. A: Math Gen., **25**, 3449-3472 (1992).
- [68] F. Mokross and H. Buttner, Thermal Conductivity in the Diatomic Toda Lattice J. Phys. C: Solid State Phys., **16**, 4539-4546 (1983).
- [69] M. Toda, Vibration of a chain with nonlinear interaction J. Phys. Soc. Japan, **22**(2), 431-436 (1967).
- [70] N. Li and B. Li, Temperature dependence of thermal conductivity in 1D nonlinear lattices EPL, **78**, 34001 (2007).
- [71] J. J. Freeman, G. J. Morgan, and C. A. Cullen, Thermal conductivity of a Single Polymer Chain Phys. Rev. B, **35**(14), 7627-7635 (1986).
- [72] J. Kirkwood, The Skeletal Modes of Vibration of Long Chain Molecules Journal of Chemical Physics, **7**, 506-509 (1939).
- [73] B. G. Sumpter *et al.*, Atomistic Dynamics of Macromolecular Crystals Adv. Poly. Sci., **116**, 27-58 (1994).
- [74] J. Hansen and I. McDonald, *Theory of Simple Liquids*. 2 ed. 1986, London: Academic Press.
- [75] D. Frenkel and B. Smit, *Understanding Molecular Simulation*. 2001: Academic Press. 600.
- [76] S. Maruyama, A molecular dynamics simulation of heat conduction in finite length SWNTs Physica B, **323**, 193-195 (2002).
- [77] A. Henry and G. Chen, High Thermal Conductivity of Single Polyethylene Chains Using Molecular Dynamics Simulations Phys. Rev. Lett., **101**, 235502 (2008).
- [78] R. Car, Introduction to density-functional theory and ab-initio molecular dynamics Quantitative structure-activity relationships, **21**(2), 97-104 (2002).
- [79] D. J. Singh and L. Nordstrom, *Planewaves, Pseudopotentials, and the LAPW Method*. 2 ed. 2005: Springer. 134.
- [80] F. Ercolessi and J. B. Adams, Interatomic Potentials from First-Principles Calculations: the Force-Matching Method Europhys. Lett., **26**(8), 583-588 (1994).
- [81] D. W. Brenner *et al.*, A Second-Generation Reactive Empirical Bond Order (REBO) Potential Energy Expression for Hydrocarbons Journal of Physics: Condensed Matter, **14**, 783-802 (2002).
- [82] J. Che *et al.*, Thermal conductivity of diamond and related materials from molecular dynamics simulations J. Chem. Phys., **113**(16), 6888-6900 (2000).

- [83] S. Stuart, A. B. Tutein, and J. A. Harrison, A Reactive Potential for Hydrocarbons with Intermolecular Interactions *Journal of Chemical Physics*, **112**(14), 6472-6486 (2000).
- [84] S. Plimpton, Fast Parallel Algorithms for Short-Range Molecular Dynamics *J. Comp. Phys.*, **117**, 1-19 (1995).
- [85] M. Toda, R. Kubo, and N. Saito, *Statistical Physics I*. 2 ed, ed. P. Fulde. 1995, Berlin: Springer-Verlag.
- [86] G. D. Barrera *et al.*, The Vibrational Spectrum and Ultimate Modulus of Polyethylene Macromolecules, **39**, 2683-2690 (2006).
- [87] S. Volz and G. Chen, Molecular-dynamics simulation of thermal conductivity of silicon crystals *Phys. Rev. B*, **61**, 2651-2656 (2000).
- [88] S. G. Volz, Thermal Insulating Behavior in Crystals at High Frequencies *Phys. Rev. Lett.*, **87**(7), 074301 (2001).
- [89] R. Hardy, Energy-Flux Operator for a Lattice *Phys. Rev.*, **132**(1), 168-177 (1963).
- [90] H. B. Callen and T. A. Welton, Irreversibility and Generalized Noise *Phys. Rev.*, **83**(1), 34-40 (1951).
- [91] G. Domingues *et al.*, Heat Transfer between Two Nanoparticles Through Near Field Interaction *Phys. Rev. Lett.*, **94**, 085901 (2005).
- [92] C. Cercignani, *Theory and Application of the Boltzmann Equation* 1975, New York: Elsevier.
- [93] V. N. Popov, V. E. V. Doren, and M. Balkanski, Elastic properties of single-walled carbon nanotubes *Phys. Rev. B*, **61**(4), 3078-3084 (2000).
- [94] A. J. C. Ladd, B. Moran, and W. G. Hoover, Lattice thermal conductivity: A comparison of molecular dynamics and anharmonic lattice dynamics *Phys. Rev. B*, **34**(8), 5058-5064 (1986).
- [95] G. P. Srivastava, Phonon Conductivity of Insulators and Semiconductors *J. Phys. Chem. Solids*, **41**, 357 (1980).
- [96] L. Sun and J. Murthy, Domain size effects in molecular dynamics simulation of phonon transport in silicon *Appl. Phys. Lett.*, **89**, 171919 (2006).
- [97] L. Yin *et al.*, Structure image of single crystal of polyethylene *Polymer*, **44**, 6489-6493 (2003).
- [98] R. G. Snyder, S. J. Krause, and J. R. Scherer, Determination of the Distribution of Straight-Chain Segment Lengths in Crystalline Polyethylene from the Raman LAM-1 Band *J. Polymer Science*, **16**, 1593-1609 (1978).
- [99] E. Skow, Processing and thermal properties of molecularly oriented polymers, Massachusetts Institute of Technology, *Masters*: p. 63 (2007).